Synthesis & Characterization of Graphene Enhanced Electroless Ni-P Composite Coatings

by

Ahmad Raza Khan Rana

Submitted in partial fulfilment of the requirements
for the degree of Master of Applied Sciences

at

Dalhousie University
Halifax, Nova Scotia
March 2020

DEDICATED TO MY BELOVED PARENTS

TABLE OF CONTENTS

List of tables

List of figures

Abstract

Electroless Ni-P coating has attracted attention since few decades due to high hardness and corrosion resistance. However, applications that demand high wear and cracking resistance require coatings to exhibit toughness along with erosion and corrosion resistance. Extending applications of Ni-P coatings are impeded by cracking under Hertzian and scratching loads as well as erosion under high velocities. Graphene is known for high hardness and impermeability, so was selected as an additive for Ni-P coating matrix to produce Ni-P-graphene coatings having enhanced properties. Coatings were characterized by Hertzian-type indentation, scratch tests along with acoustic emission monitoring. The indents and scars were characterized by microscope to investigate toughening. Wear rates, toughening and damage mechanisms were identified and discussed in detail. Corrosion, erosion and erosion-corrosion properties of the developed coatings were also addressed. Graphene addition in Ni-P coating matrix is found to significantly improve its hardness, toughness, corrosion, erosion and erosion-corrosion attributes.

List of abbreviations & symbols used

API - American petroleum institute

AISI - American iron and steel institute

AE - Acoustic emission

CVD – Chemical vapor deposition

DC – Direct current

EDS - Electron dispersive spectroscopy

EIS – Electrical impedance spectroscopy

E-C - Erosion-corrosion

K_{co} - Pure corrosion rate

K_{eo} - Pure erosion rate

K_{ec} Erosion enhanced corrosion

ΔKe – Corrosion-enhanced erosion

ΔKc – Erosion-enhanced corrosion

K_s - Synergism

MMC – Metal-matrix composites

MW-PECVD – Microwave plasma enhanced chemical vapor deposition

Ni-P – Nickel Phosphorous composite

Ni-P-G – Nickel Phosphorous and Graphene composite

PD – Potentiodynamic

PECVD – Plasma enhanced CVD

PMAFS – Powder metallurgy assisted friction surfacing

SAGD – Steam-assisted gravity drainage

SCE – Saturated calomel electrode

SEM - Scanning electron microscope

SLG – Single-layered graphene

SPE - Solid particle erosion

SPEC - Slurry-pot erosion-corrosion

STM – Scanning tunneling microscope

TEM – Transmission electron microscope

† - Trade name

Acknowledgements

I would like to express my feelings of gratitude to my supervisor Prof. Dr. Zoheir Farhat for his immense guidance and support throughout my MASc Materials Engineering Program at Dalhousie University. I would like to thank Prof. Dr. George Jarjoura for his support and opportunity to participate as lab instructor/ TA for undergraduate corrosion course. I would also like to say thanks to my lab mates Zhi Li, Nicole Cameron and Marisa Maclean for their support with my research activities. Finally, I would like to acknowledge the priceless support and tremendous patience of my family members during this research program.

Ahmad Raza Khan Rana

March 2020

Chapter 1 Introduction

1.1 Background and Objectives

Pipelines and process equipments in hydrocarbon industry are vulnerable to degradations due to various damage mechanisms [1-2]. The nature and extent of such damage mechanisms can vary depending upon various factors such as pipeline/ process equipment's material, service conditions and environmental factors.

EC (erosion-corrosion) and pure erosion are among the prominent damage-mechanisms observed in hydrocarbon industry; and are known for versatility of failure modes (pitting, micro-cutting, gouging etc.) [1, 3]. Solid particle erosion and EC are quite common in the systems handling powdered catalyst, oil sands and slurries etc. During erosion-corrosion, material loss rate is significantly higher than the sum of material loss rate due to pure erosion and pure corrosion acting separately. In certain instances, the shape and morphology of damaged surface and number of removed debris provide signs of this damage mechanism [4].

Some applications of carbon steel in the petroleum industry (e.g. alkaline sour water systems) require certain flow rate (3 ms^{-1} – 6 ms^{-1}) to avoid stagnant conditions as well as fouling especially in case of heat exchangers [1]. However, higher velocities beyond 20 fps can jeopardize the integrity of carbon steel due to erosion or EC damages. On the other hand, some materials such as SS 316L is more resistant to localized pitting under flowing conditions than under stagnant conditions, as it retains protective oxide layer under flowing conditions [5]. Furthermore, the alloys of Cu and Al are easily worn out under high velocity streams due to their lower hardness [1]. For these reasons, there have been some

established IOWs (Integrity Operating Windows) for the optimum flow rates with respect to metallurgies as well as parameters of contained service (e.g. 20 fps for lean amine solution) in order to pro-actively mitigate such degradations. Finally, there have also been well established guidelines for optimum velocity considering different metallurgies against sea water flow conditions (tidal, immersed, jet etc.) [1, 5].

Some chemical process units employ fluids that contain abrasive particles in suspended state. One such example is the oil sand facility where the feed stock and process fluids contain erosive sand as well as corrosive agents (sulfur, organic acids, salts etc.). Process equipments for oil sands processing (centrifuges, vessels etc.) and transportation (pumps, pipelines, valves etc.) are highly prone to EC and erosion damages. EC and pure erosion are driven by a number of factors that include (but not limited to) particle attributes (velocity, angle of attack, size, shape, weight/ density, hardness), material attributes (hardness, ductility, corrosion resistance, geometry) as well as service conditions (chemistry, corrosivity, temperature etc.). In the past few years, there have been considerable efforts to combat this degradation with detailed focus on each mitigation facet e.g. use of higher Mo containing alloys to resist organic acid corrosion or the use of higher corrosion allowances by keeping more wall thickness. Material up-gradations and surface modifications through re-designing are other possible solution to ensure the integrity of process equipments and pipelines.

In spite of all of above said measures, there are still challenges in terms of EC due to higher associated costs. Coatings are one of effective measure; that can protect the surface of materials by preventing the exposure to the environment and service conditions. Electroless coatings are known for their excellent adhesion properties. The non-existence of grain boundary due to amorphous structure is the primary reason for higher corrosion resistance of Ni-P coatings. Moreover, the absence of solvents in electroless coatings is another

advantageous aspect that eliminates the efforts associated with drying, curing, and subsequent inspections. Unlike conventional solvent (liquid) containing epoxy coatings application, there is no segregation of DFT (dry film thickness) & WFT (wet film thickness) inspections. Also, electroless coatings are environmentally safe and more reliable in terms of better surface finish and ease of application when compared FB (fusion bond) epoxy and liquid epoxy coatings. However, there is still a need to improve the cracking and wear performance of Ni-P coatings to extend their application in the hydrocarbon, energy and aerospace industries. It has been reported that the wear behavior of Ni-P coatings can potentially be improved by using ternary coating [6].

Graphene, the one atom thick allotrope of carbon [7], is a potential candidate for ternary coatings due to its attribute i.e. higher hardness, lower density [8], higher impermeability [9-10] as well as hydrophobic nature. Also, there have been numerous composite coatings reported so far that are developed by enrichment of graphene and its derivatives [11-15] with improved corrosion and wear/ erosion behaviors. Tamilrasan [16] recently reported significant improvement in EC behavior of Ni-P coatings due to enrichment of graphene in the coating matrix. Also, few studies [16-19] have reported improvement in hardness due to incorporation of graphene. On the other hand, variation of EC behavior of graphene enriched Ni-P coatings w.r.t surface roughness is still un-explored. Finally, tribological behaviors of graphene enhanced Ni-P coating such as wear, scratching and indentation etc. are yet to be explored.

The specific objectives of current research work are as follows:

1. Characterization of commercially available graphene for its defects, number of layers as well as suitability for coating application
2. Determine the optimum plating parameters (stirring speed, graphene concentration, plating time etc.) for achieving a homogenous distribution of graphene along with achieving an optimum coating thickness

3. Investigation of cracking and scratching behavior of electroless Ni-P coatings matrix with and without addition of graphene
4. Investigate the impact of graphene addition on erosion-corrosion, pure corrosion and solid particle erosion performance of electroless Ni-P composite coatings

1.2 Graphene overview

Graphene is a single atom thick layer (0.345 nm) of sp^2-hybridized carbon atoms densely packed in a honeycomb crystal lattice, and known for its remarkable electrical, mechanical, optical and magnetic properties. Figure 1.1 shows hexagonal arrangement of graphene revealing ɓ-bonds and Л-bonds [20] where each Carbon atom has three ɓ-bonds and Л-bond with neighboring Carbon atoms. Graphene is the only allotrope with the highest number of edge atoms and every atom is available/ exposed due to its two-dimensional configuration. Single layer graphene has shown exceptionally higher electrical conductivity than that of few layered graphene [21]. Single layered graphene is reported to have high (100x) chemical reactivity than thicker graphene sheets [22]. Table 1-1 summarizes the various reported attributes of graphene.
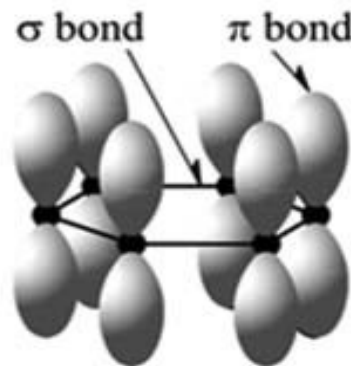
Figure 1.1– Arrangement of Carbon atoms in graphene network [20]

Table 1-1 Attributes of graphene [20]

Attribute	Value
Fracture Strength	125 GPa
Thermal Conductivity	5000 ~ 8000 W m^{-1} K^{-1}
Young's Modulus	1100 GPa
Specific Surface Area	2630 m^2/g
Optical Transmittance	97.7 %

Most of applications of graphene require growth of single layer graphene on a substrate and is difficult to control [20]. Л-Л interactions lead to re-stacking of graphene. Whereas, defects in a graphene nano sheet increase its reactivity. Increased number of layers can turn graphene into graphite that becomes metallic and is of least importance for producing high strength MMCs (metal-matrix composites). Some challenges associated with graphene synthesis are to control the number of produced layers along with enhanced productivity.

1.2.1 Synthesis of graphene

Various methods have been developed so far for producing graphene that differ in terms of methodology, type of feedstock (precursor), substrate, nano-structural quality, productivity, morphology of product and the number of produced layers. Synthesizing graphene at reasonable cost with microstructural quality is a primary concern. Most developed methods rely on 3-D crystals or substrates to produce 2-D graphene. Each method has its own advantage and limitations. Given below are the details of some of reported methods.

1.2.1.1 Chemical vapor deposition techniques

CVD is known for producing high surface area graphene. The quality of graphene produced by CVD is much influenced by the substrate as they can influence (based on solubility of carbon) whether the graphene is a result of precipitation (e.g. on Ni) or surface catalysis (e.g. on Cu). Growth of large surface area and defect free films is a major challenge. Various methods of CVD have been reported for development of SLG (single layer graphene), BLG

(bi-layer graphene) as well as FLG (few layered graphene) on various substrates [23]. In one of reported method, camphor was first evaporated at 180 ºC on Ni and pyrolyzed in another chamber (i.e. CVD furnace) at 700 ºC – 850 ºC, using Argon as carrier gas. Upon natural cooling to room temperature, few-layered (~ 35 layers) graphene was observed on Ni foil [23]. An alternative method involved a gas mixture of H_2 and CH_4 in a 92:8 ratio at a gas pressure of 80 Torr that was discharged by DC. The resulting graphene on the substrate indicated ridge formation due to differential thermal expansions (between graphene and Ni) and nucleation due to hetro-epitaxial growth of graphene (1-2 nm thick) on Ni [24]. In another method, 3-4 layered graphene was produced by CVD employing a gas mixture of methane, hydrogen and argon in the ratio of 0.15:1:2. The flow rate of gas mixture was kept as 315 sccm. Synthesis time was 20 minutes at 1000°C. Moderate cooling resulted in the formation of graphene on Ni substrate [25]. Similar techniques likely to fail when Si is used as substrate instead of Ni.

CVD can take the benefit from plasma and microwave where these methods have been found promising in producing graphene on variety of substrates (W, Si, Ni, Cr, Mo, Nb, SiO_2, Al_2O_3, SS 304 L etc.) without surface preparation or catalyst deposition [26]. In a reported method, 1-3 layered graphene was produced on SS substrate by MW-PECVD at 500 ºC. The method utilized a mixture of methane and hydrogen (1:9 ratio) at a pressure of 30 torr under 200 sccm flow rate. Microwave power was kept as 1200W. Produced graphene showed the better crystallinity than any other method [27].

1.2.1.2 Exfoliation and cleavage

Graphite contains layers of graphene in stacked form and these layers are stuck together under the influence of weak Van Der waals forces. So, the graphene can be prepared from highly pure graphite by breaking the bonds produced by these Van Der Waals forces. Graphene nano-sheets can be separated by exfoliation as well cleavage methods; that in

turn requires mechanical or chemical energy for breaking these bonds [20]. Exfoliation is basically a repeated peeling process and can be dry or liquid phase exfoliation. In a dry exfoliation HOPG (highly oriented pyrolytic graphite) sheet of 1 mm thickness was dry etched in oxygen plasma to make many mesas of 5 μm. The etched graphene was transferred on a photoresist (substrate) and baked, allowing the mesas to stick firmly to the photoresist. Then scotch tape peeling was used to peel-off the layers from graphite sheet. The flakes attached to photoresist were released in acetone and transferred to Si substrate. These flakes (on Si substrate) found to have single to few layered graphene [26]. In liquid-phase exfoliation, single to few layered graphene has been produced by various methods as dispersion and exfoliation of pure graphite in N-Methyl Pyrrolidone and SSDB (sodium dodecylbenzene sulfonate) [28-29]. Liquid phase exfoliation can be promising in large-scale production of graphene. The limitation could be the impurity levels and defects that in turn impact the attributes of produced graphene [26].

1.2.1.3 Chemical methods

Other than liquid-phase exfoliation (which is also regarded as a chemical method), there are other chemical approaches to extract the graphene from graphite without exfoliation. In one of the reported method natural graphite was subjected to multi-step oxidation and purification processes, followed by dilution using methanol and centrifuging to produce graphene sheets from dispersion. The resulting graphene had 1-6 layers and thickness was proportional to the dilution factor [30]. In a different chemical approach, sulfuric and nitric acid were intercalated between layers of graphite followed by rapid heating to 1000 ºC. The explosive evaporation of acid molecules led to the formation of thin graphitic sheets. In a second-step intercalation, oleum and TBA (tetra-butyl ammonium hydroxide) were used to synthesize single and few-layered graphene using sonication in a surfactant solution [26]. In another chemical approach named Hummer's method, strong oxidants are used

throughout the process such as concentrated sulfuric acid, nitric acid, and potassium permanganate. The graphite sheet is exfoliated and oxidized under the action of strong oxidizing agent, and then subjected to a reduction method such as thermal or chemical reduction. A reduction agent is used to eliminate oxygen-containing functional groups to achieve graphene.

1.2.1.4 Biological methods

Biological methods may involve exfoliation, reduction or both for synthesis of graphene. Various studies report the reduction of GO (graphene oxide) from biomolecules (ascorbic acid, glucose, melatonin, humanin etc.). Utilization of biomaterials results in effective synthesis of graphene in terms of saving (time and energy) as well as elimination of endotoxins contamination. Biological modification of GO using polyphenolic compound (resveratrol) provides better biocompatibility, solubility and selectivity than chemical-reducing agents such as hydrazine and citrate [31]. Another low cost and environmentally friendly biological approach involve the use of plant extracts (as bio-surfactants) for liquid phase exfoliation of graphite into graphene [32].

1.2.1.5 Thermal decomposition of SiC

Hydrogen etched surface of 6H-SiC were heated to a high temperature (1250 – 1450 ºC) for a time of 1-20 minutes. Graphene was thermally decomposed on the surface plane (0001) of single crystal of 6H-SiC. Graphene with 1-3 layers was epitaxially grown on the surface, whereas number of layers were dependent on the decomposition temperature [33]. Furthermore, there are reported methods of graphene synthesis on a Ni-coated SiC substrate that yielded continuous layers of graphene at a much lower temperature of 750 ºC [34]. This method of graphene synthesis can be promising for semiconductor applications [26].

1.2.1.6 Unzipping of CNTs

Various methods have been reported so far to synthesize graphene using MWNT (multi-wall nanotubes) as starting material. In one of the approaches, CNTs were opened longitudinally by the intercalation of Li and ammonia. The intercalated layers were exfoliated in the acid followed by abrupt heating. The resulting product contained partially opened MWNTs along with graphene flakes and nanoribbons. In a different approach, graphene nanoribbons were produced by the plasma etching of polymer embedded MWNTs. A chemical approach for producing substrate-free graphene employed multi-step exfoliation using concentrated H_2SO_4, $KMnO_4$ and H_2O_2 followed by oxidation using $KMnO_4$ and reduction using NH_4OH and hydrazine monohydrate ($N_2H_4.H_2O$) solution [26]. In another approach, Aluminum sulfide (Al_2S_3) was calcined in gaseous environment containing CO and Argon. The reaction led to the formation gaseous carbon and α-alumina. Graphene sheets were later crystallized on alumina particles [35].

1.2.2 Graphene defects

Defects can occur in graphene during its synthesis or post synthesis such as chemical treatment, irradiation etc., that can impact the chemical, mechanical, thermal, electrical and magnetic properties of graphene and produced composites. Agglomerates due to re-stacking of graphene platelets can likely compromise the intended attributes of composite matrix. In MMC (metal-matric composite), the diffusion of defective graphene platelets with metals may lead to formation of carbide (e.g. Al_4C_3 in Al matrix) that will deteriorate the strength and hardness of resulting MMC [36]. Uniaxial strains are likely developed in the graphene during the bending of underlying substrates. Defects can also change the hybridization status of Carbon atoms in the graphene layer.

1.2.2.1 Intrinsic defects

The intrinsic defects in graphene can be classified into five types that are detailed as: [37]

1.2.2.1.1 Stone-Wales defect

This defect is also termed as Stone-Thrower-Wales defect that involves change in the connectivity of two Л-bonded carbon atoms by a rotation of 90º w.r.t centre point of the bond as shown in Figure 1.2. This rotation can happen in CNT, graphene and similar framed carbon allotropes that leads to a nucleophile region with greater chemical reactivity, making them a preferred site for binding to hydrogen [38]. Presence of such defects along CNT network can enhance conductance along a specific path leading to charge delocalization. This defect doesn't result in removal or introduction of carbon atom from the network. Stone-Wales defect can be introduced intentionally using electron radiation or rapid cooling in a high temperature environment and requires formation energy of 5 eV. This type of defect can be visualized using STM (Scanning Tunneling Microscopy) and TEM (Transmission Electron Microscopy) and characterized by IR spectroscopy [39].
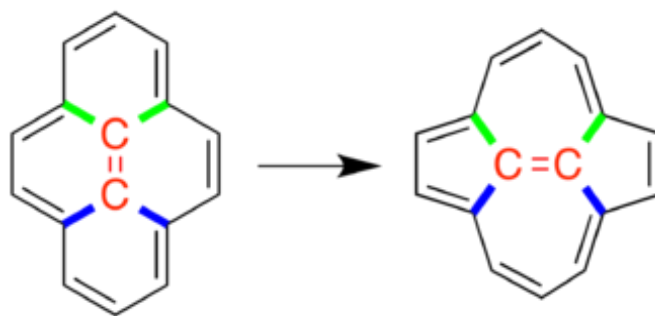
Figure 1.2 – Stone-Wales Defect due to rotation of Л-bonded Carbon atom [37]
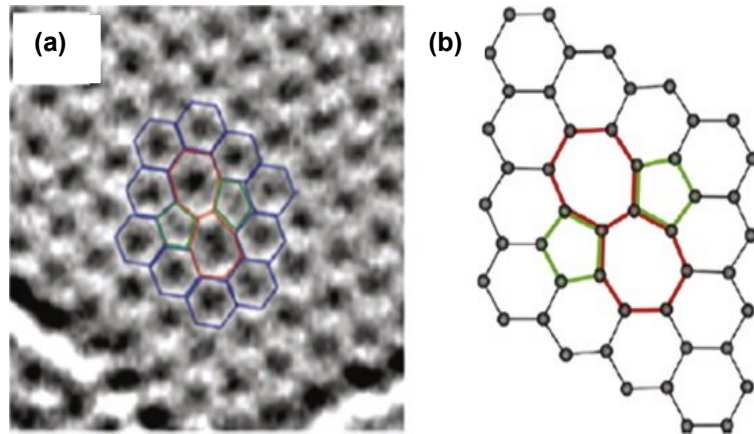
Figure 1.3 – (a) TEM image and (b) atomic structure from DFT (density functional theory) for Stone-Wales defect on graphene network [37]

1.2.2.1.2 Single vacancy defect

Single vacancy defect refers to the removal of a single carbon atom from the ring. The consequent graphene undergoes Jahn-Teller distortion to minimize the total energy. Two of the three dangling binds are connected to each other and towards missing atom. The formation energy for such a defect is approx. 7.5 eV. Figure 1.4 (a-b) shows TEM image and atomic structure from DFT calculations for graphene with single vacancy defect [37].
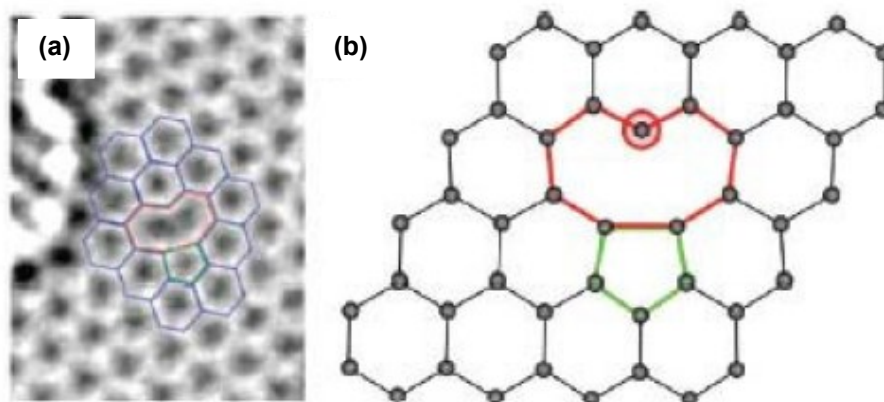
Figure 1.4 – (a) TEM image and (b) atomic structure from DFT for single vacancy defect on graphene network [37]

1.2.2.1.3 Multiple vacancy defect

Multiple vacancy defect refers to the removal of more than a single carbon atom from the ring. There are three different consequential arrangements from multiple vacancies in graphene network as shown in Figure 1.5 (a-f). Figure 1.5 (a) and 1.5 (d) shows the arrangement that comprise of two pentagons and one octagon (rather four hexagons) in the event of loss of two carbon atoms. The formation energy for this configuration of multiple vacancy defect is 8 eV. Whereas, Figure 1.5 (b) and 1.5 (e) shows the arrangement that result from transformation from first arrangement under certain conditions and has a formation energy of 7 eV. These defects in Figure 1.5 (b) and 1.5 (e) also under Л-bond rotation like Stone-Wales defects. This rotation will result in stabilization of whole system through reduction in the energy of graphene structure. One step further would be the transformation of second vacancy defects into more complex configuration via rotation of another bond as shown in Figure 1.5 (c) and 1.5 (f). The formation energy of this configuration of defect is somewhere in between 7.0 eV and 8.0 eV. The removal of more carbon atoms will result in larger and complex configuration defects [37].
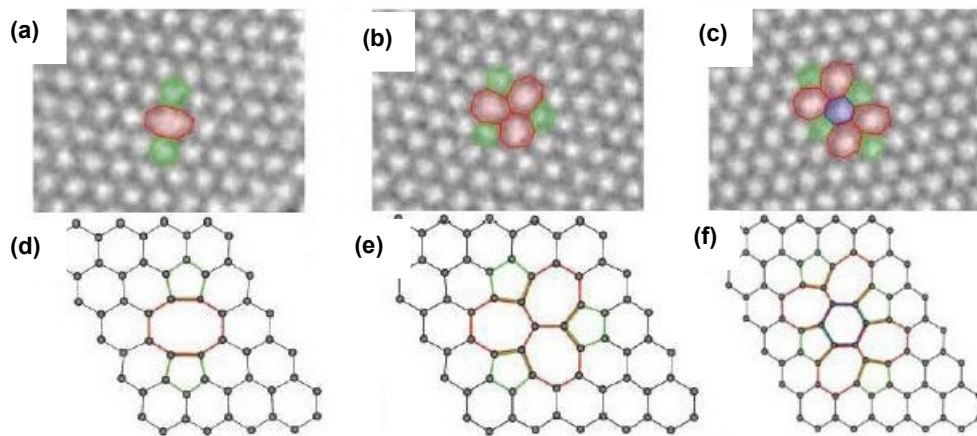
Figure 1.5 – (a) – (c) TEM image and (d) – (f) atomic structure from DFT for multiple vacancy defect on graphene network [37]

1.2.2.1.4 Line defect

This can happen during CVD process due to graphene growth randomly at different positions. Cross-fusion begins due to graphene growth to a certain size. The defect is indicated in Figure 1.6 where the two crystals are stitched together by chain of hexagons, pentagons and heptagons. The boundary/ interface between crystals is not straight thereby making defects as non-periodic alongside the boundary.
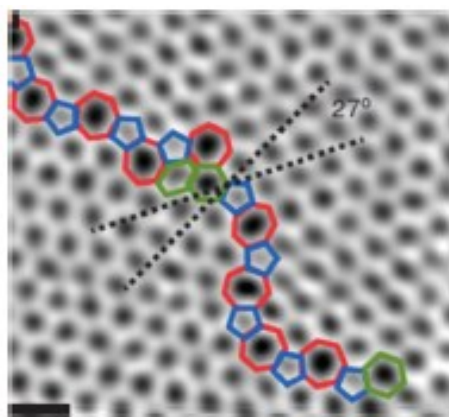
Figure 1.6 – ADF-STEM (aberration corrected annular dark field scanning transmission electron microscopic) image of line defect on graphene network [37]

1.2.2.1.5 Out of plane carbon ad-atoms

Missing carbon atom generated from single and multiple vacancy defects may not be completely off the graphene plane. These carbon atoms in turn migrate on the surface of graphene after separation from hexagonal ring. These carbon atoms have the affinity to interact with neighboring perfect graphene layer. This interaction results in the formation of 3D structure thereby compromising the original planar structure of graphene layer. Carbon ad-atom is shown in Figure 1.7 (a) and 1.7 (d) that forms a bridge-type configuration on top of C-C layer. Whereas, Carbon atoms can also migrate through the lattice forming a metastable dumbbell configuration as shown in Figure 1.7 (b) and 1.7 (e). Figure 1.7 (c) and 1.7 (f) show inverse Stone-Wales defect formed by two migrating carbon ad-atoms.

The out of planes ad-atoms have very fast migration rate or high formation energy and can't be characterized using TEM or STM. The structure tends to be more complex as a greater number of carbon ad-atoms are introduced. Also, some degree of sp^3-hybridization can happen locally. Such defect is challenging in terms of its mitigation or elimination.
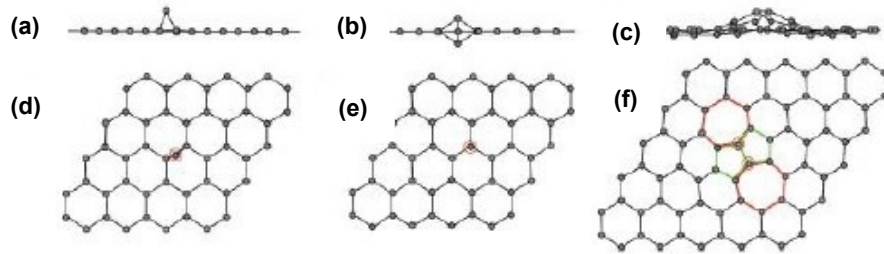
Figure 1.7 – Introduction of defects on the outside surface of graphene (a) – (c) space structure (d) – (f) location of induced carbon atoms [37]

1.2.2.2 Introduced defects

Furthermore, there are two types of introduced defects that are detailed as:

1.2.2.2.1 Foreign ad-atoms

Metal atoms or oxygen-containing functional groups (hydroxyl, carboxyl etc.) are inevitably introduced onto the surface of graphene during synthesis by CVD or strong oxidation methods (e.g. Hummers method). These ad-atoms undergo covalent bonding or weak van der Waals interaction with nearest carbon atoms. Such defects are known as foreign ad-atoms and result in significant migration on the surface of graphene. Complete removal of oxygen atoms during reduction of oxidized graphite is a difficult process, so there is a certain amount of oxygen despite of thermal or chemical reduction(s). Such defect can be characterized by detection of oxygen content and its form using photoelectron spectroscopy.

1.2.2.2.2 Substitutional impurities

Nitrogen and boron atoms can replace the carbon atoms in graphene network due to their ability to form three chemical bonds. These heteroatoms in turn constitute the impurity defects as shown in Figure 1.8 (a) and 1.8 (b). Nitrogen and boron atoms can exist independently and can also exist simultaneously by controlling the synthesis method(s). Nitrogen-doped and boron-doped graphene have excellent attributes in terms of catalytic activity and conductivity.
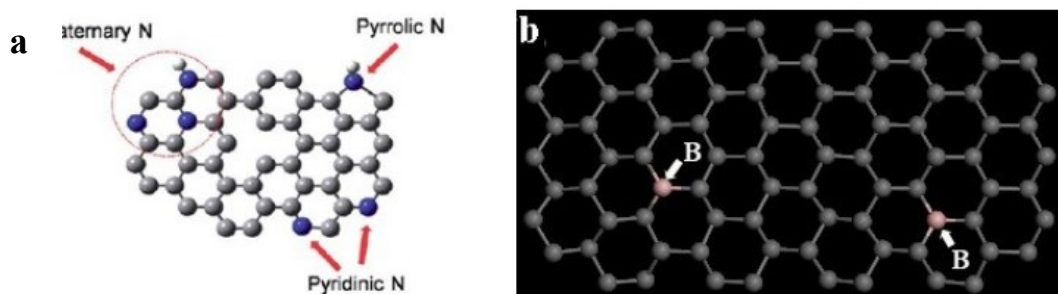
Figure 1.8 – In-plane heteroatom substitution defect model of graphene showing (a) nitrogen defects (b) boron defects [37]

1.2.2.3 Double graphene structure defects

There will be no interlayer bonding among the carbon atoms in case of defect-free graphene. With intrinsic defects (holes, dangling bonds and migrating carbon atoms), there will be formation of new chemical bonds among the carbon atoms. The structural defects will be more complex if there is stacking of multiple layers of graphene that will in turn affect the macrostructure and properties of the resulting materials (e.g. coatings) [37].

1.2.3 Raman spectroscopy

Raman spectroscopy is a vibrational technique with extreme sensitivity to molecular bonding and geometric structure(s). It collects the low frequency and vibrational signatures

of a molecule giving insight into how it is put together, as well as how it interacts with other molecules around it. Unlike FTIR (Fourier transformation infrared spectroscopy), it relies on the scattering of light rather than absorption. During Raman scattering, the molecule upon interacting with photons may be elevated to a higher energy state. These molecules may in turn relax to a higher vibrational energy (level) thereby producing a photon of different energy. The difference between energies of incident and scattered photons is regarded as Raman shift as shown in Figure 1.9 (a) [40]. Raman scattering enables the characterization of very small differences through resulting Raman spectra. The intensity and pattern off different peaks can help to fairly gauge the defects in graphene, number of layers as well as synthesis methodology (reduction, CVD etc.).

(a)
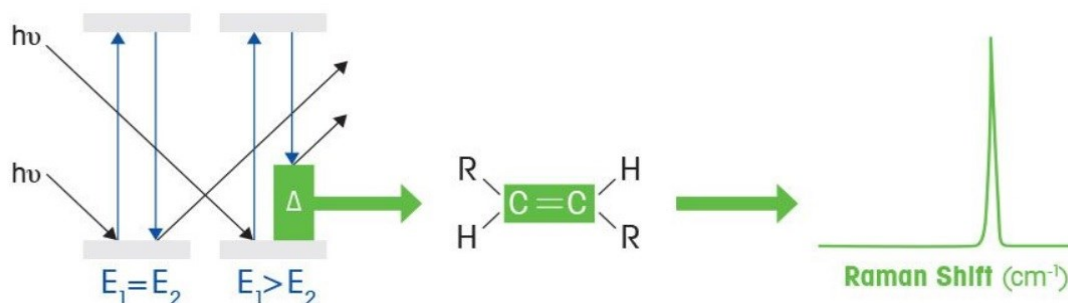
(b)
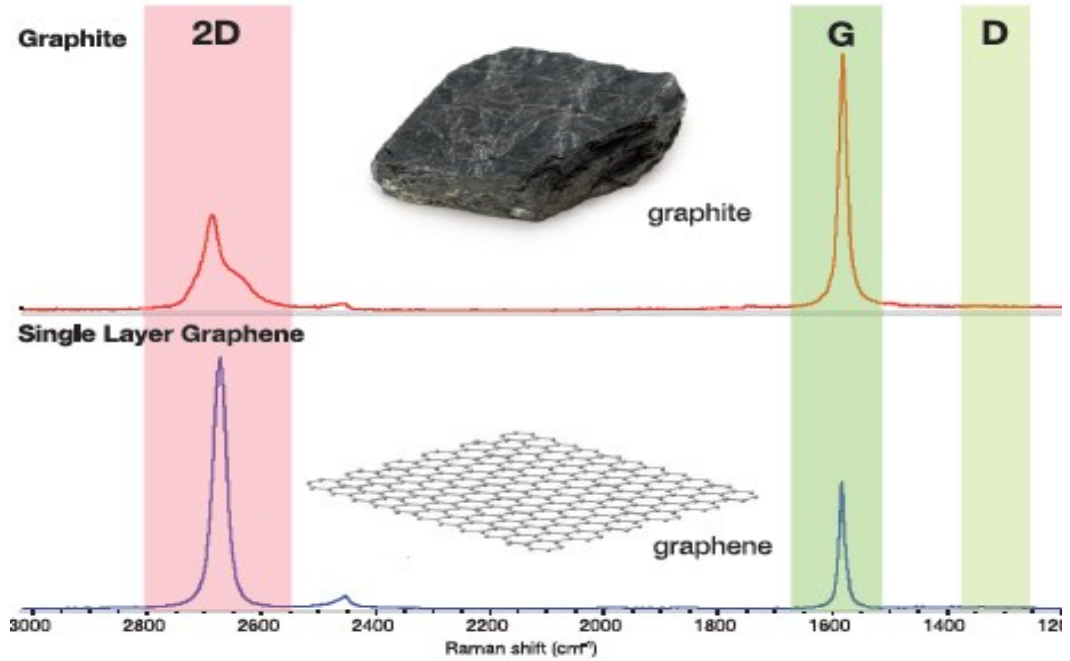
Figure 1.9 (a) Raman scattering pattern schematic [40] (b) and typical Raman spectrums of graphite and defect-free graphene using 532 nm laser [41]

Figure 1.9 (b) shows the typical Raman spectrums of graphite and defect-free graphene as generated by a laser with a wavelength of 532 nm [41]. D-peak represents the breathing mode from sp^2 carbon rings and reveals defects (edge, basal plane) in the nanostructure of graphene. Whereas, suppressed D-peak is indicative of either graphite or defect-free graphene. On the other hand, intense D-peak would be representative of graphene with defects. Position and shape of this band is subjected to change with change in the wavelength of incident laser beam i.e. different patterns can be seen for 514 nm laser than those by 532 nm and 633 nm laser, respectively [41]. G-band in a typical Raman spectrum shows the in-plane vibrational mode of sp^2 hybridized carbon atoms that constitute the graphene sheet or sample. The wavenumber for G-peak is highly sensitive to the number of layers in a graphene sample. For 532 nm lasers, number of layers are calculated using equation (1.1) as [41]:

$$Wavenumber_{G\ peak} = 1581.6 + \frac{11}{1+n} \qquad (1.1)$$

17

Whereas, n= number of graphene layers

The wavenumber of G-peak that is an indicative of number of layers, and highly sensitive to temperature, doping effects and even small strains in the graphene sample. On the other hand, intensity of G-peak can help to gauge layer thickness of graphene. Increased intensity implies higher thickness of graphene layer. In general, the wavenumber(s) of G-peak in monolayer and ten-layered graphene are 1587.1 cm^{-1} and 1582.6 cm^{-1}, respectively under a laser wavelength of 532 nm. 2D-peak is the second order or resonating mode of D-peak and is not an indicative of graphene defects unlike D-peak. The wavenumber as well as shape of 2D peak also represents the thickness of graphene layer. On the other hand, the supressed 2D peak indicates multi-layers in graphene sample. Also, the shape of 2D peak is an indicative of synthesis method utilized. Finally, an ideal defect-free single layered graphene exhibits intensity ratio of 2 between 2D-peak and G-peak i.e. $I_{2D}/ I_G= 2$, when examined by a laser with a wavelength of 532 nm [41]. The current research work has utilized the capability of Raman to examine the graphene and differentiate between graphene, GO, graphite etc. using laser with wavelengths of 514 nm and 633 nm.

1.2.4 Potential applications

The excellent properties of graphene make that a suitable candidate for variety of industrial applications. Various avenues that can benefit from graphene and its derivatives comprise (but not limited to) below:

1.2.4.1 Electrical

The graphene sheet displays a semi-metallic (or zero-gap semiconductor) character, although the same is not possible for a graphene sheet rolled into a CNTs due to curvature(s). The band gap in graphene can be varied from 0 eV to 0.25 eV by the application of voltage. Graphene has a remarkable electron mobility of 15,000 $cm^2 V^{-1} s^{-1}$ and the lowest resistivity of 10^{-6} $\Omega \cdot cm$ at room temperature, which is the lowest-ever for any

material [42]. EMI (electromagnetic interference) is an undesired interruption in RF (radio frequency) signals due to conduction, electrostatic and electromagnetic induction from external sources. The optical transmittance and conductivity make graphene a potential choice for transparent EMI (electromagnetic interference) shielding [43]. Graphene is a suitable material for construction of quantum computers due to its two-dimensional and charge functionalization attributes [44].

1.2.4.2 Composite coatings

Protective coatings have huge demand to deal with variety of material degradations across modern-day's hydrocarbon, energy, marine, space applications. As an excellent nano-filler combined with higher hardness, impermeability and charge carrier properties, graphene can be used for anti-corrosion and anti-wear coatings. Potential applications of graphene can be erosion-corrosion resistant coatings in pipelines, SAGD (steam-assisted gravity drainage) systems, anti-fouling coatings for heat exchanger tube bundles and ships. Also, the impermeability can make it a potential candidate to deal with HIC (hydrogen induced cracking) by covering the laminates, that can cause cracking of metal in the event of H_2S intrusion inside the laminates as shown in Figure 1.10. Various methods have been reported so far to produce graphene enriched composite coatings such as CVD, epoxy paints, PMAFS, electroless plating, electrochemical plating etc. Graphene has potential for self-healing coating applications due to its ability to align with carbon atoms in a hexagonal manner, thereby filing the holes or coating imperfections [45].
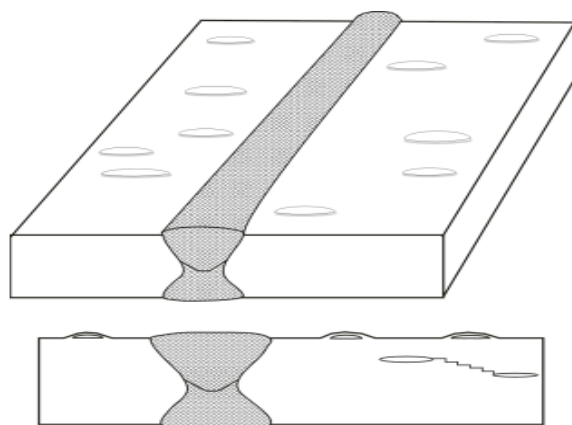
Figure 1.10 – Blistering and HIC in steels due to H2S permeation inside delaminates [1] *

1.2.4.3 Catalyst applications

Catalysts are widely used in the chemical industry to make manufacturing processes more efficient and economical by providing an alternative pathway for the synthesis of chemicals and compounds. Graphene and its derivatives will be a promising candidate for catalyst applications due to its high surface area to volume ratio. High surface area and high adsorption capacities make it suitable for catalyst support systems as well. On the other hand, catalytic potential of graphene is still un-explored due to inertness of graphene; and requires research efforts to unlock the inertness of graphene. Furthermore, GBSSC (graphene based solid-state catalysis) is an emerging as well as emerging application of graphene for sustainable catalysis [46]. GO (Graphene oxide) a derivative of graphene is a potential candidate for carbo-catalysis. Graphene has been reportedly used as a carbo-catalyst in various transformations such as oxidation of alcohols and alkenes into respective aldehydes and ketones as well as hydration of alkynes. Other than carbo-catalysis, the graphene and its derivatives can be used in photo-catalysis, metal-free catalysis as well as catalyst support. Other than economics and bulk production, the challenges that impede the wide use of graphene application in catalysis are segregation and re-stacking from Л-Л

20

bonds interactions. Also, nano-catalysts supported by graphene can have low stability due to interactions with graphene. The higher surface energies of metallic nano-catalysts (supported by graphene) can make the graphene lose its synergistic impact in catalysis [47].

1.2.4.4 Thermal management

Excellent thermal conductivity combine with high surface area and flexibility has motivated researchers to find avenues of using graphene and its derivatives for thermal management applications. Various candidate derivatives of graphene for thermal management are GO (graphene oxide), graphene films, graphene foams, graphene fibers, graphene laminates and graphene TIM (thermal interface materials). Unlike traditional heat spreaders made from aluminum and copper, graphene-based heat spreaders can be much efficient and lightweight. On the other hand, the thermal conductivity of graphene is impacted by the device's structure as well as geometry and decreases significantly compared to suspended graphene. Also, the thermal performance of graphene is impacted by the synthesis method [48]. The nature of graphene as heat spreader can pave the way towards composite materials that will reduce the size and performance of heat exchangers in the oil and gas application(s). Figure 1.11 and Figure 1.12 show an electronic chip thermograph and a U-type bundle of shell and tube heat exchanger, respectively.
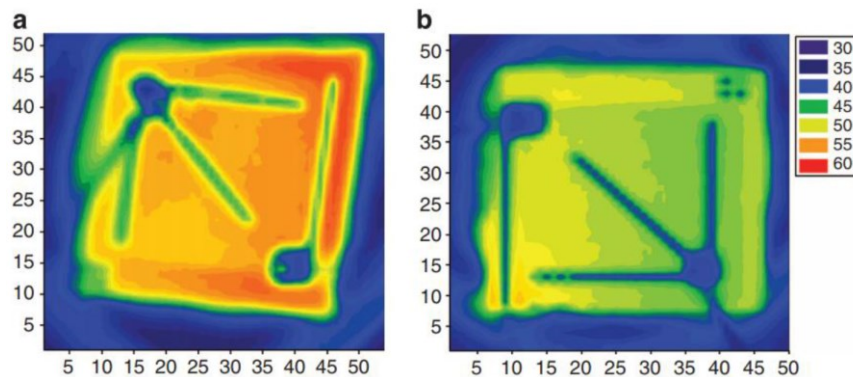
Figure 1.11 – Infrared thermograph of electronic chip (a) without RGO (b) with RGO [48]

21
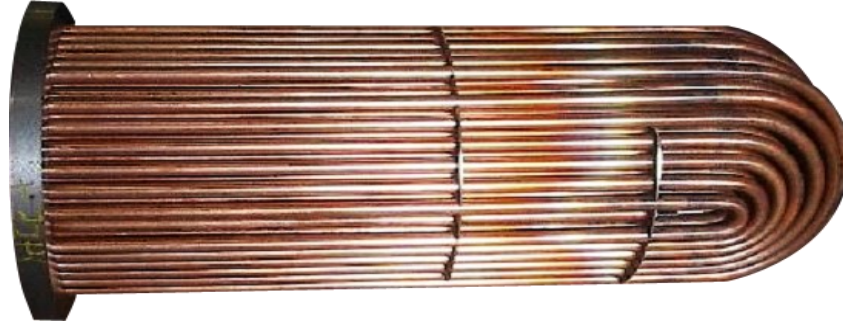
Figure 1.12 – U-type bundle for shell and tube heat exchanger

1.2.4.5 Medical applications

The 2D allotropic structure of graphene, GO (and its composites) has paved their use in tissue engineering, gene and small molecular drug delivery [49]. Other medical applications of graphene and GO include (but not limited to) anti-cancer therapy, bio-functionalization of proteins and antimicrobial agent for bones and teeth implantation [50].

1.3 Ni-P composite coatings

Since last few decades, electroless Ni-P has been used as protective coating for various industrial applications due to its high hardness (4.9 – 5.9 GPa) [51]. The coating uniformity , absence of the need for external current during the electroless process makes it promising candidate in terms of ease of application. The absence of grain boundary (i.e. amorphous structure) makes Ni-P corrosion resistant. In electroless Ni-P reactions, Ni sulfate is used as a salt and sodium hypophosphite as reducing agent. Ni and P are co-deposited on the substrate(s) as a result of below reactions [19]:

$$(H_2PO_2)^- + H_2O \rightarrow H^+ + (HPO_3)^{2-} + 2H_{abs} \tag{1.2}$$

$$Ni^{2+} + 2H_{abs} \rightarrow Ni + 2H^+ \tag{1.3}$$

$$(H_2PO_2)^- + H_{abs} \rightarrow H_2O + OH^- + P \tag{1.4}$$

$$(H_2PO_2)^- + H_2O \rightarrow H^+ + (HPO_3)^{2-} + H_2 \tag{1.5}$$

The microstructure of as-deposited electroless Ni-P coatings varies with the content (wt. %) of P (phosphorus). At lower concentration (i.e. < 7 wt.%) of P, Ni-P coatings are crystalline. On the other hand, higher phosphorus concentration makes Ni-P matrix amorphous [15]. The concentration of P in the matrix is quite sensitive to pH of plating bath. The optimum pH (4.5 – 5.5) is required to achieve a balance of P (to achieve amorphousness) and Ni (to achieve the hardness) in the coating matrix. The acidic solutions for Ni-P plating also require an optimum temperature of 85 ºC – 90 ºC while alkaline Ni-P solutions can work at lower temperature(s). The acidic solutions work best to achieve higher P content in the matrix, whereas alkaline is used for reduced P content [51]. There are certain limitations with Ni-P matrix such as brittleness and pores/ defects from the release of hydrogen during electroless plating reaction as shown earlier in Equation (1.5).

Ni-P-graphene composite coatings have been attempted in various studies employing different concentrations and multiple derivatives of graphene (graphene powder, platelets GO, RGO etc.) [13-18]. All these studies reported an improvement in the composite coating matrix due to obvious barrier and mechanical properties of graphene. All the reported works [13-18] have commonality that the stirring speeds were kept very low (50-100 rpm) during Ni-P-graphene plating reactions.

1.4 Damage mechanisms of materials

All materials are prone to degradation due to inherent limitations, environment(s) or by various defects that happen during the manufacturing, handling, installation and operating conditions etc. The various defects from manufacturing can be classified as point imperfection, line imperfection and area imperfection. Broadly speaking, these degradations include (but not limited to) cracks, voids/ porosities, wear and corrosion.

1.4.1 Cracks

Brittle materials are likely to exhibit different cracks under indentation loading. Formation and propagation of cracks in materials requires stress, either applied or residual. Micro-fracture and cracking behavior of materials have been investigated widely by contact-type indentation tests. Two different shaped indenters as spherical and pyramid (known as Berkovich) are typically used for these indentation tests. Magnitude and distribution of stress is influenced by indenter's shape; whereas, pyramid shaped indenter has higher stress than spherical indenter under the same applied load. Figure 1.13 shows Hertzian crack formation under spherical indenter that assumes non-conforming, frictionless surfaces with small strains in the elastic limit.
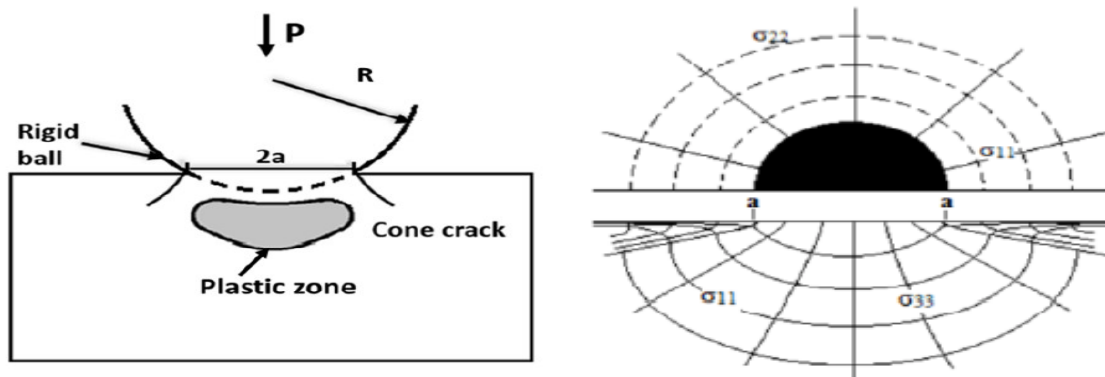
Figure 1.13 – a) Hertzian Indentation Process and stress trajectory's b) top view c) side view [52]

Robert Cook and George Pharr identified five different crack types that occurred under both indenter types. Theses are named as cone, radial, median, half-penny and lateral cracks as shown in Figure 1.14 (A - E) [53].
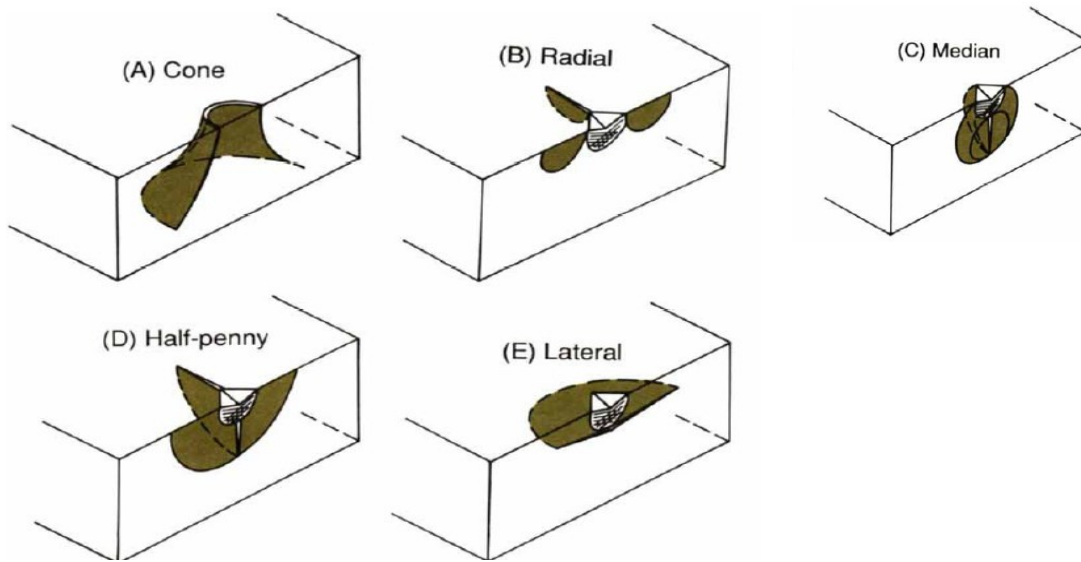
Figure 1.14 - Typical crack-types in materials under indentation loads [53]

Cone cracks (or Hertzian ring cracks) are typical in case of spherical indentation. A cone crack was first studied by Hertz in 1881 on silicate glass. The crack initiates as a surface ring crack at the edge of contact and then propagates downwards, forming a cone eventually. The angle of the cone by which the crack extends depends on the Poisson's ratio of the material. Radial cracks (or Palmqvist cracks) occur with both spherical and sharp indentation loads; and known to exist under wide range of contact loads [51]. Radial cracks are generally parallel to load axis and originate from the edge of plastic contact [53]. The localized load generated during plastic deformation is the driving force behind generation and propagation radial cracks. Like radial cracks, median cracks are also parallel to the load axis. However, they are caused by pyramid shaped indenters and generate underneath the elastic-plastic zone. A half-penny crack can be generated from growth of median crack alongside the surface, or downwards propagation of radial crack, or from the combination

of both median and radial cracks. Lateral cracks are usually circular in shape and happen to be underneath the deformation zone. Unlike other cracks, these form during the unloading of indenters (rather loading). These are parallel to the surface and driven by the residual stresses.

Performance of protective coatings is compromised in the presence of cracks. The formed cracks in the protective coatings result in the seepage of corrosive service (i.e. electrolyte) in the space between substrate, that in turn triggers the crevice corrosion underneath the coating. This corrosion (underneath the cracked coating) results in various failure modes such as spalling, de-adhesion, blisters as shown in Figure 1.15 [54].
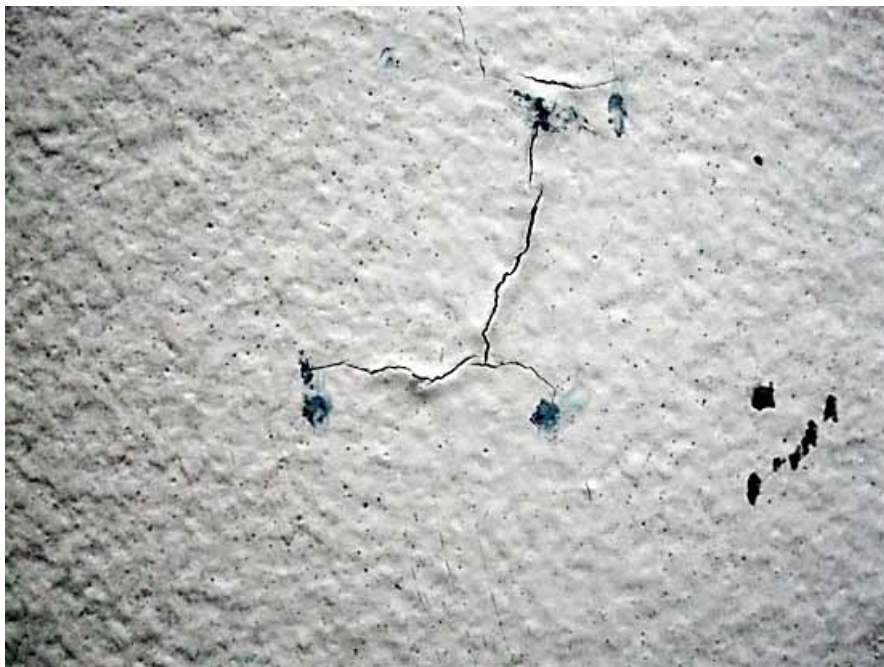
Figure 1.15 - Typical cracks, pores and blisters on protective coatings [54]

Micro-cracks can be examined using one of (or combination of) methods such as: microscopic examination, travel distance of indenter in a progressive load scratch test and AE (acoustic emission) signal. Whereas, cracks in various industrial systems are detected

using visual examination or other non-destructive examinations such as microscopy, ECT (eddy current test), RT (radiography), WFMT (Wet Fluorescent Magnetic Test), AE (acoustic emission) and ACFM (altermatic current field measurements). The selection of test methods is conditional to the type of process and anticipated cracks. The cracking of industrial assets may come from various drivers such as stresses, operating temperature(s), service conditions, Table B1 and B2 in appendix summarize the various cracking(s) reported in the oil and gas and petrochemical environments.

1.4.2 Wear

Wear is the degradation of material that results in deformation or gradual removal of particles from its matrix. Wear is much common type of material degradation that can impact the wide range of material from household shovels to aerospace components. Various wear types are detailed below:

1.4.2.1 Abrasive wear

Abrasive wear occurs when any solid object (e.g. pipeline, shovel, machinery etc.) is loaded against the particles with equal or higher hardness. The mechanism of abrasive wear is influenced by grit geometry and presence of lubricants. Even minor amounts of harder particles in soft bulk matrix may cause abrasive wear. An example is the worn-out impellers and other components in sugarcane industry from small amount of silica (sand) that exists in molasses of sugarcane. Various failure modes of abrasive wear that can be think of are scratching, scoring and gouging; that vary with extent of abrasive wear. Abrasive wear involves a variety of wear mechanisms namely cutting, micro-ploughing, micro-fracture, accelerated fatigue from repeated deformations and grain pull-out etc. that act in conjunction. Figure 1.16 shows the possible wear mechanisms in abrasive wear(s) [55]. Micro-ploughing ideally doesn't detach the material from surface; rather it just displaces the materials on the sideways of formed groove. Repeated movement of slider on the same

wear track causes the micro-cracking of ridges and subsequent loss of material. Micro-cutting results in chips formation with size equal to volume of the formed groove. Micro-ploughing and micro-cutting be dominant failure modes in case of ductile materials. The ratio/ extent of micro-ploughing to micro-cutting is governed by attributes of asperity (hardness, angle of attack). Micro-cutting will prevail over ploughing in the scenarios of high hardness and higher angle of attack [56].
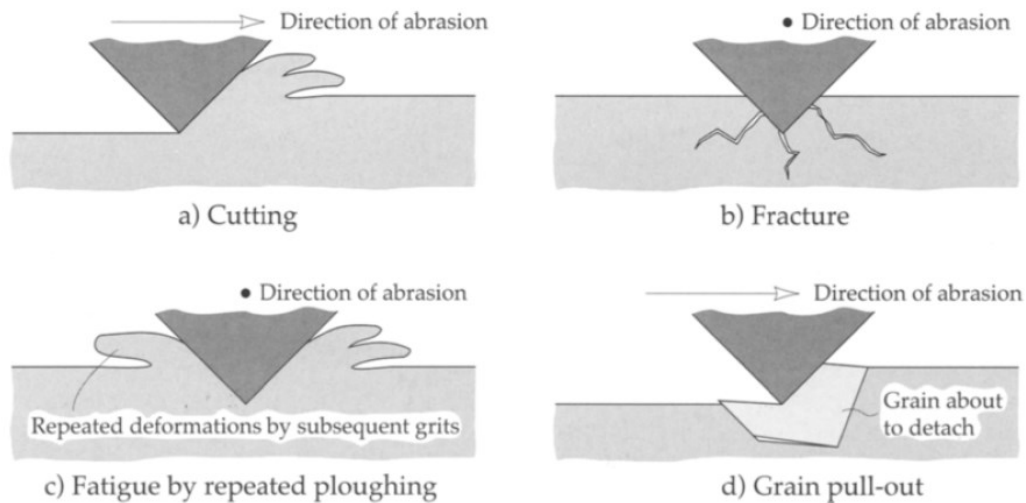
Figure 1.16 – Mechanisms of abrasive wear [55]

1.4.2.2 Erosive wear

Erosive wear is caused by the impact of solid or liquid particles over material's surface and material strength doesn't guarantee the minimization of wear. Erosive wear involves several mechanisms that are dependent on several factors including particle velocity, particle's size as well as angle of impingement etc. [1,55]. At high speeds the particle may cause brittle fracture or plastic deformation depending on nature of material. The repeated impact of blunt or spherical particles at the location of plastic deformation in turn leads to materials

loss in the form of thin plates. Whereas, sharp particles cause brittle fragmentation or cutting. On the other hand, the stresses at the impingement point is insufficient in the event of low speed to cause plastic deformation and the wear proceeds by fatigue instead of plastic deformation. At very high speeds, melting of surface may occur. The space satellites are prone to erosion from gaseous particles where the atoms are eroded away from the lattice. Figure 1.17 shows different possible mechanisms of erosive wear.
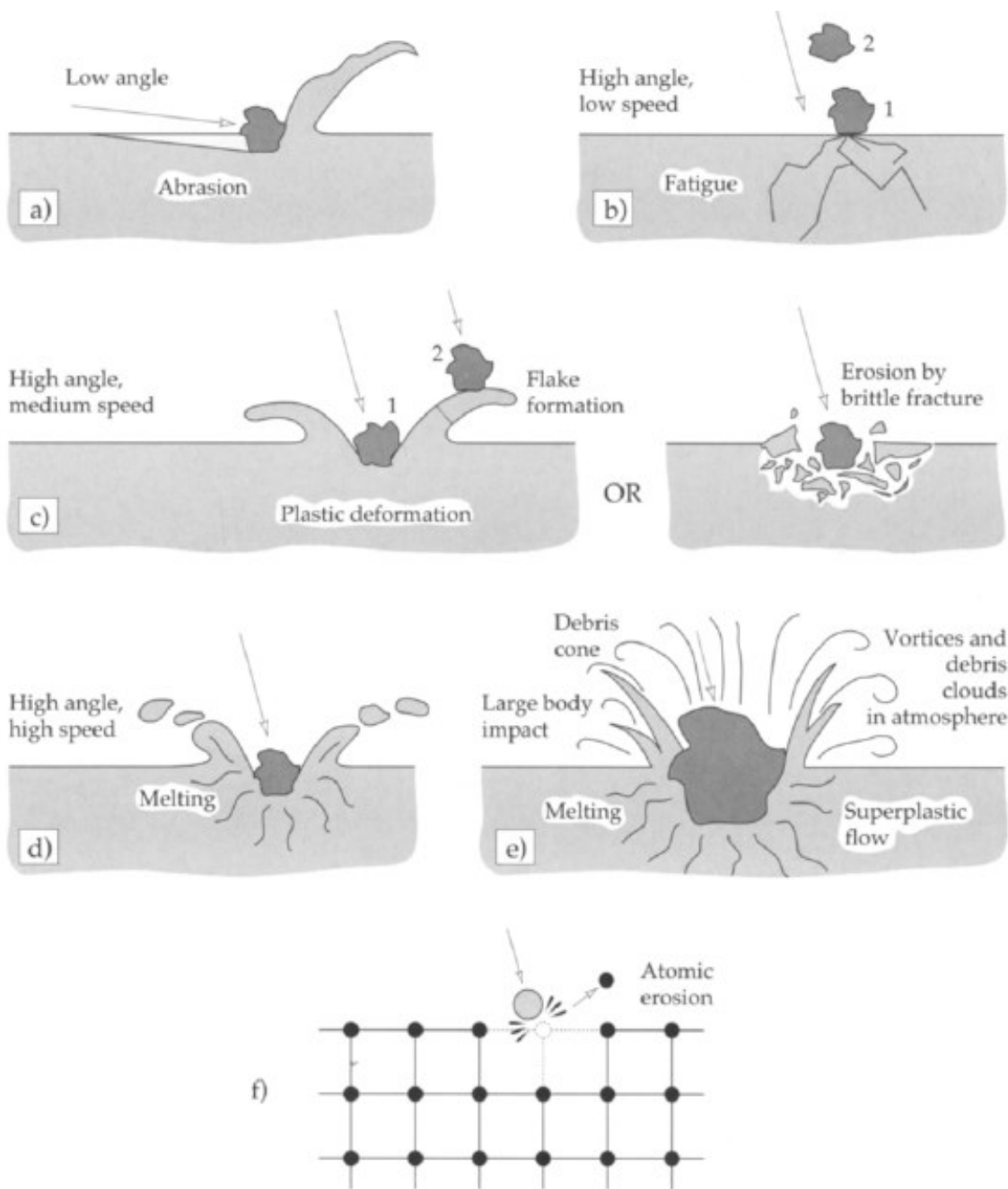
Figure 1.17 – Mechanisms of erosive wear [55]

1.4.2.2.1 Effect of impact angle and velocity on erosive wear

At zero impingement angle, there is negligible wear loss as there is no contact between particle and material's surface. The nature of material (ductile or brittle) also has significant impact on the wear rate(s). At high impact angle (i.e. 90⁰), the brittle material suffer fragmentation from the fracture whereas, the ductile material undergoes indentation/ plastic deformation. At lower impact angle of 30⁰, the ductile material will undergo plastic deformation or ploughing (or cutting) whereas, the brittle material may undergo fracture depending on particle's speed and hardness. Figure 1.18 shows the typical relationships between wear rate and impingement angle for ductile and brittle material(s) [55].
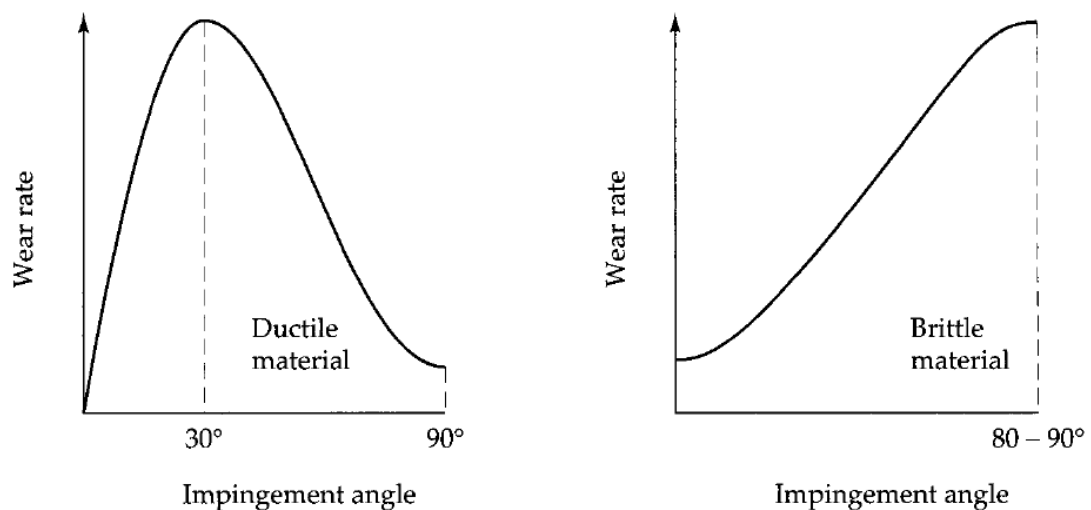
Figure 1.18 – Trend of wear rate(s) w.r.t impingement angle [55]

There is often a threshold velocity above which erosion may occur which is also dependent on material and service conditions [1]. For medium to high speeds, the relationship between wear rate and erosion velocity is given by Equation (1.6) as [55]:

$$-\frac{dm}{dt} = Kv^n \qquad (1.6)$$

Whereas,

m = erosion rate (Kg)

t = Duration of process (s)

k = empirical constant

V = Impact velocity (ms⁻¹)

n = Velocity exponent

On the other hand, threshold velocity can be calculated by Equation (1.7) as [57]:

$$V_e = C\rho m^{-1/2} \qquad (1.7)\,*$$

Whereas,

V_e = Fluid erosional velocity (ft s⁻¹)

ρm = Gas-liquid mixture density

C = Empirical constant

1.4.2.2.2 Effect of erodent attributes (size, shape and hardness and flux rate) on erosive wear

Hard particles yield higher wear rates than softer particle. Also, the sharp particles cause more erosive wear than round particles. The ratio of substrate hardness to particle's hardness seems to be a controlling parameter. The higher hardness has more impact on erosive wear for brittle materials than as of ductile materials.

It's impossible to completely isolate the hardness from other particle attributes. It has been reported that increased size of erodent particle from 8.75 μm to 127 μm caused increased erosive wear. This can be attributed to the fact that increased size of erodent changed its angle of attack thereby shifting the mode from ductile to brittle. The size of particle also has the impact on the vulnerability of materials towards erosion. The large sized particles regard the materials in terms of toughness and small sized particle rely on the hardness of materials in terms of controlling the erosion rates as shown in Figure 1.19 [55].
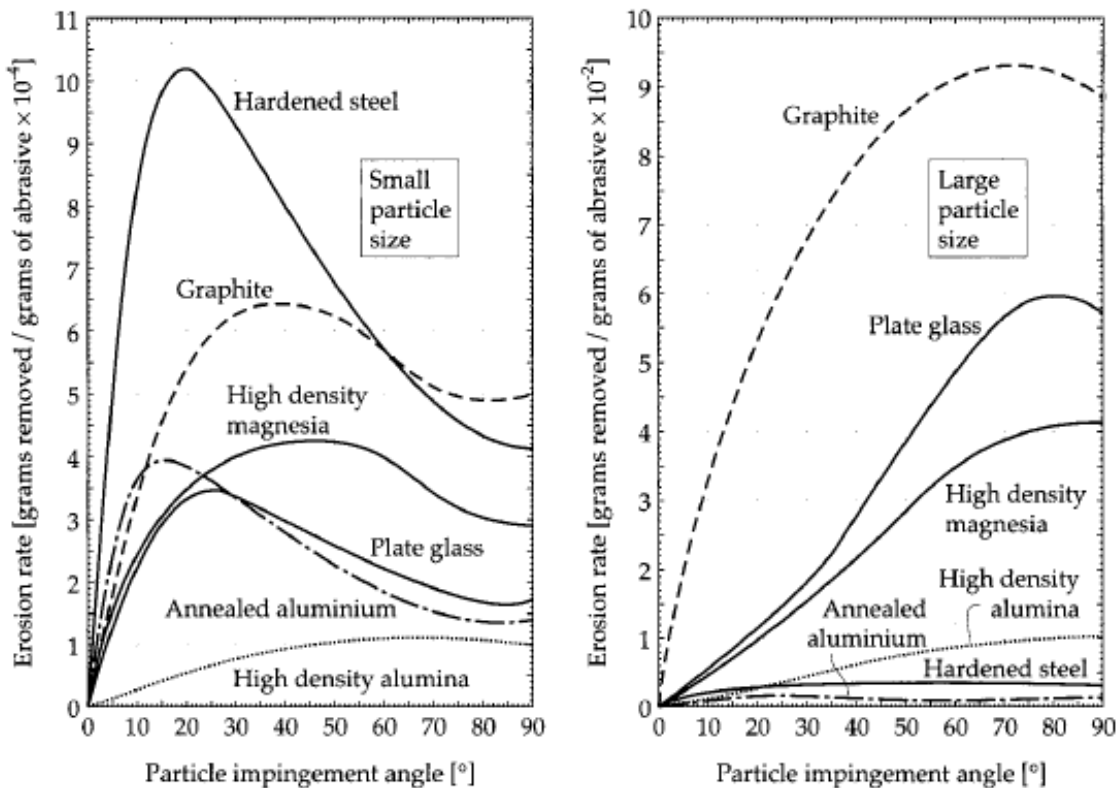
Figure 1.19 – Ranking of materials for erosion rates w.r.t particle size and impingement angle [55]

The change in the wear mode is also a consequence of spacing of defects (cracks, voids, holes etc.) within the solid. If the impinging particles are small, then there is a least possibility

that the striking particles will encounter the site of defect. The material underneath the particle upon impact experiences the stresses and plastic deformation is a consequence of absence of defects, which is the most likely scenario with small particle size. On the other hand, the material removal in the event of plastic deformation requires repeated impact at same location which is very rare with smaller particles. Hence smaller particle has ductile mode leading to slow wear rate. Whereas, large particles have likely chance to encounter the defect sites which results in fracture (brittle mode) and increased wear rate(s). The flux (i.e. mass flow) rate of particle is proportional to wear rate to a certain value. Any further increase of flux rate beyond that value in turn reduces the wear rate. This can be attributed to the interference between the incoming and returning/ bouncing particles. This limit is termed as "limiting flux rate" and is quite variable w.r.t materials and other attributes (shape and velocity etc.) of particle. Another important factor that should be considered during the measurement of erosion rate(s) is the incubation period which is the time between the start of erosion to the start of measurable wear damage. Since the wear rate in the beginning may not be smooth as the erodent particle may get trapped in the eroding material(s) thereby giving an incorrect indication of wear rate(s) [55].

1.4.2.3 Corrosive wear

Corrosive and oxidative wear occur due to chemical reaction between the material and corrosive medium (liquids, air etc.) and known to exist in both lubricated and un-lubricated conditions. Both corrosive and oxidative corrosions have the commonality in terms of increased wear rate with a concurrent reduction in COF (coefficient of friction). If a metal is corroded to produce oxide layer, while it is subjected to sliding loads then any of below scenario(s) may happen:

1. Formation of weak film that is subjected to breaking and reformation leading to increased wear rate

2. A durable and passive oxide layer that is resilient to wear and corrosion

3. Pitting or defects on the protective film that result in the galvanic effects and increased crevice corrosions between the film and underlying substrate

4. Corrosion and wear acting separately with increased material loss that is sum of material loss due to corrosion, wear as well as synergism

The defects in the coatings turn out to be an intrusion site for the electrolyte, which triggers corrosion underneath the coatings leading to accumulation of corrosion products followed by de-adhesion and blisters formation as shown in Figure 1.20. Common example of corrosive wear in the engines from water contamination in methanol fuels [55].
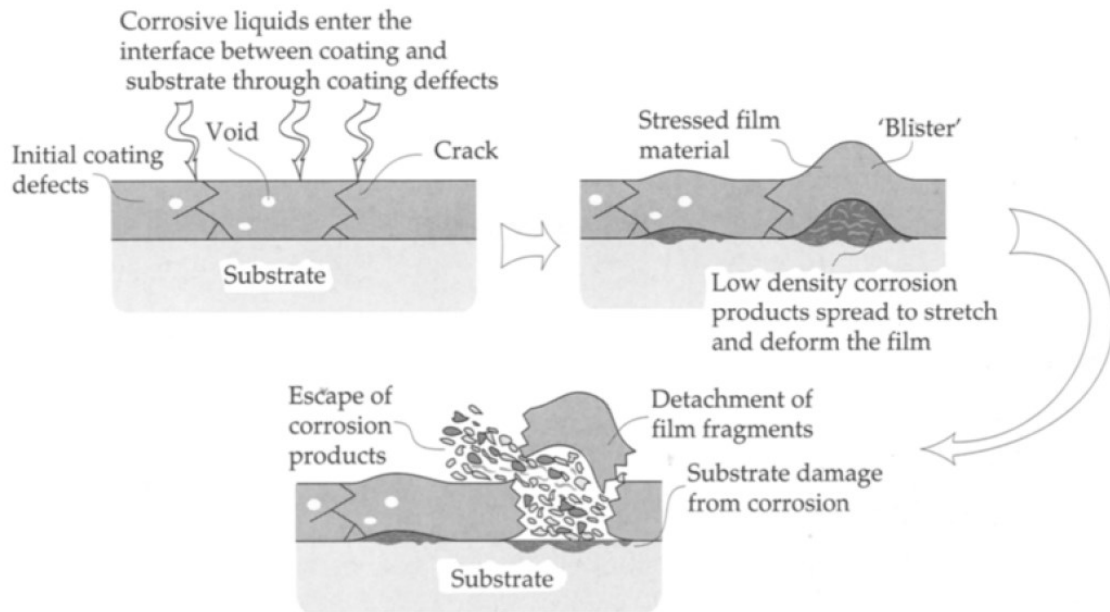
Figure 1.20 – Mechanisms of blisters in thick coatings due to corrosion products [55]

1.4.2.4 Other wear types

Lubricant films in sliding contacts are meant to provide a separation. In the event of lubricant failure to provide gap, the surface contact happens leading to adhesion of surfaces and adhesive wear. This leads to highly unstable COF and found in sliding contacts such as bearing systems in turbomachinery. Cavitation wear is the result of cavitation that is the mechanism of bubble formation and collapse at metal surfaces thereby degrading the surfaces due to pitting. This damage is quite common in control valves and machinery (pumps, turbines etc.). Figure 1.21 shows the worn-out impeller of centrifugal pump. Fatigue wear happens due contact of asperities in the rolling and sliding surfaces (even well lubricated) that along with localized stresses lead to fatigue propagation (crack initiation, crack growth and fracture). Cyclic and compressive loadings lead to high Hertzian contact stresses. The rate/ extent of fatigue wear is highly influenced by the microstructure of the material. Fretting wear happens due to short distant sliding motion between the surfaces for a large number of cycles. Melting wear happens due to melting of surfaces caused by high temperature resulting from high sliding speeds and loads. Electric arc between sliding surfaces leads to electrical discharge wear. Diffusive wear involves the diffusion of atoms among the sliding surfaces at high temperatures. An example is the diffusion between the rake face of cutting tool (near to cutting edge) and metallic chip. Impact wear originates from repetitive collision among the surfaces which causes elastic and plastic deformations. When impact is high, the fatigue is accompanied by wear debris from crack formation [55].

Figure 1.21 – Worn out impeller of centrifugal pump

1.4.2.5 Synergism between corrosive and abrasive wear

Abrasion can accelerate the corrosion as it may remove the passivating film(s) that in turn leads to increased material loss. This typical process is also known as erosion-corrosion which is quite common in the equipment (vessels, centrifuges) and pipelines handling slurries and erosive hydrocarbons (i.e. oil sands) [1]. Figure 1.22 shows the cyclic process involving formation and removal of corrosion products from the impact of abrasive particles. When the corrosion is slow compared to abrasion, the grits may remove the underlying metals showing little interference with corrosion films. Resistance of materials against corrosion-abrasion (or erosion-corrosion) is dependent on their resistance to corrosion. That means a soft and non-corroding polymer will be more durable than a hard & corrodible steel [55]. Another mode of corrosive-abrasive wear happens when the oxide scales have higher hardness than base metals and lead to a significant increase in wear of base metals even when sliding against a soft surface. This is because soft surface provides a counter-face for

abrasive particles of oxide that leads to increased wear of metallic surfaces [58]. This mode is significant for biomedical application whereas Ti$_6$Al$_4$V can be subjected to wear even when they are in contact with soft UHMWPE (ultra high molecular weight polyethylene) [55].
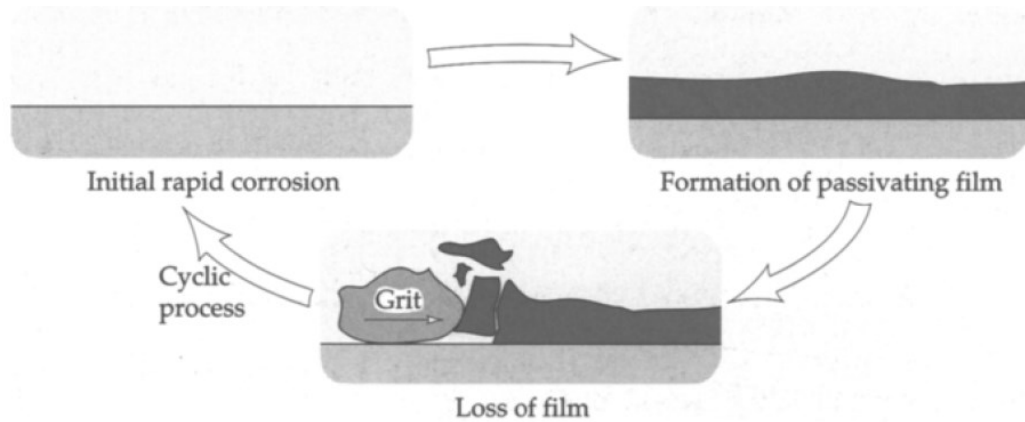
Figure 1.22 – Cyclic removal of corrosion products by abrasion [55]

1.4.3 Corrosion

Corrosion is the electrochemical degradation of metals that results in formation of non-metallic oxide scale(s) and deteriorates the properties of metals. The annual financial loss of corrosion is 275 trillion US $ and corrosion spending constitute up to 5% of income of any industrialized economy [3]. The metal sites which lose electrons (oxidize) are called anodes. Mathematically,

$$M \rightarrow M^{n+} + ne^-$$ (1.8) [3]

The sites which receive electrons (reduce) are called cathode (or cathodic regimes). An example is H$^+$ ions in acidic solutions that receive electrons and reduced to H$_2$ as [3]:

$$H^{2+} + 2e^- \rightarrow H_2$$ (1.9)

The corrosion(s) extent is dependent on various factors such as operating conditions, microstructure, oxygen concentrations, material composition, moisture presence, soil

resistivity, neighborhood factors, and design constraints [59]. Among various failure modes of corrosion are uniform or localized loss of thickness, pitting, pin hole, rupture etc. Figure 1.23 shows the pitting on the inside surface of boiler system piping from boiler heater condensate corrosion [1]. Table B3-B4 in appendix summarize various corrosion types for oil and gas applications.
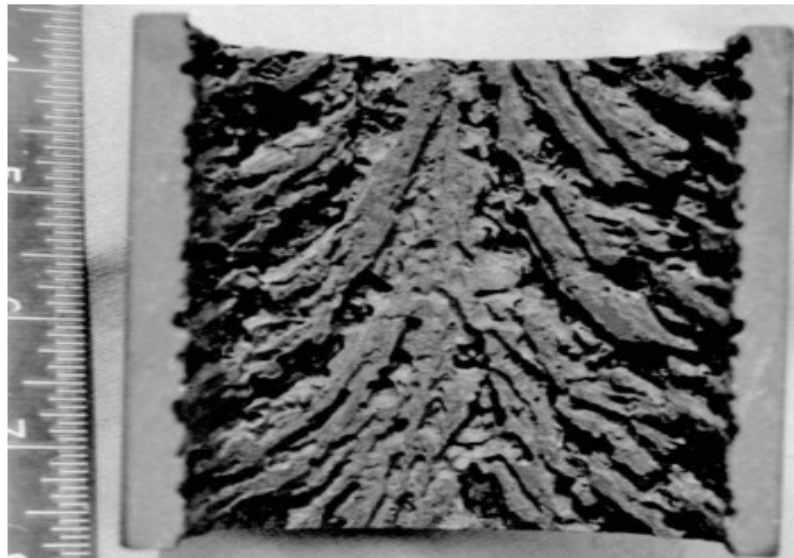
Figure 1.23 – Boiler water condensate corrosion of steam condensate pipe [1] *

1.4.3.1 Corrosion characterization

The rate of material removal is called CPR (corrosion penetration rate) or CR (corrosion rate) which is loss of thickness per unit time e.g. mm/yr. Mathematically,

$$Corrosion\ rate\ = \frac{K \times M}{A \times T \times D} \qquad (1.10)\ [60]$$

Whereas,

K = Constant

M = Mass loss (g)

A = Exposed area (cm^2)

T = Time of exposure (hr)

D = Density (g/cm^3)

Characterization of corrosion rates is a wide subject and involves many variables and methodologies. LPR (linear polarization resistance) is a a technique wherein the potential of a sample (as working electrode) with respect to a reference electrode is varied at a selected rate by application of a current through the electrolyte. The corrosion current I_{corr} is calculated from the slope of Tafel plots as shown in Figure 1.24.
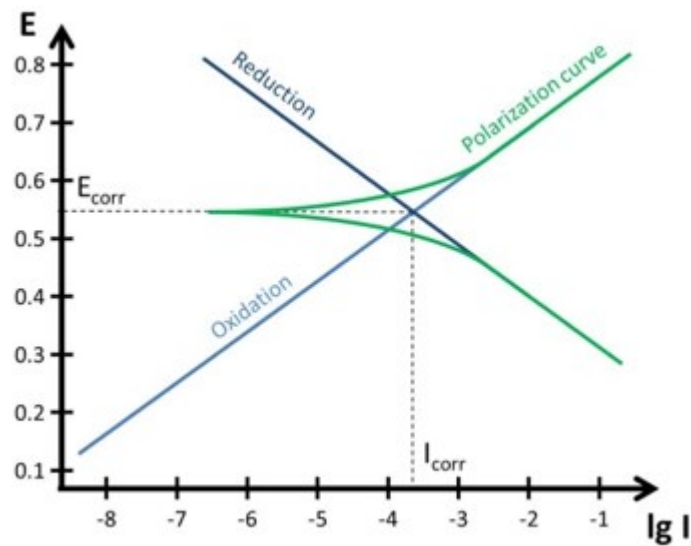
Figure 1.24 – Corrosion current measurement from Tafel plot [61]

Corrosion current density and corrosion rate is calculated using below equations (1.11) and (1.12) as [62]:

$$i_{corr} = \frac{Icorr}{Area} \qquad (1.11)$$

$$CR = \frac{0.00327 \times i_{corr} \times EW}{\rho} \qquad (1.12)$$

Other than LPR, there are other electrochemical techniques such as EIS (electrical impedance spectroscopy) and cyclic polarization which measure the capacitance and potential of materials, respectively. There are other methods for lab characterization of corrosion rates. For example, CUI (corrosion under insulation) lab simulation unlike other corrosion simulations involves a thermally insulated cell and unique parameters [60]. Erosion-corrosion characterization is conducted using SPEC testing [63]. Whereas, characterization of corrosion behaviors under HPHT (high pressure and high temperature) conditions are performed using autoclave. In-situ corrosion inspection for industrial applications involves the use of various NDE (non-destructive examinations) such as radiography, neutron back scattering, Infrared thermography, Ultrasonic thickness measurements. The future of corrosion assessment is likely to avail from AI (artificial intelligence) and machine learning [64].

1.4.3.2 Corrosion mitigation techniques

Various measures are in place to mitigate the corrosion in the industrial and infra structure assets. Other than metallurgical considerations that focus on improved properties using Ni, Cr and Mo containing alloys such as duplex stainless steels, Inconel, monel etc. Also, surface protection using a range of coatings is quite evolving. Until now, numerous coating systems and techniques are in place for various industrial and marine applications. Corrosion inhibitors are used to control the internal corrosion of chemical processing systems without compromising the chemistry of process(es). An example is the use of hydrazine (sodium meta bi sulfite) that serves as an oxygen scavenger and reduces cooling water corrosion and MIC (microbiologically influenced corrosion) in various water applications.

CP (cathodic protection) are an effective mean to mitigate the external corrosion on the surface of metal(s) for structures, storage tanks and marine equipment. It involves a

galvanic couple formation with a sacrificial metal which is more active (e.g. magnesium) than the metal. An example of CP is the galvanizing (Zn coating) on the surface of steel. Here Zn is more active (anode) than steel (cathode) and any defect on Zn surface will still prevent corrosion due to high ratio of anode to cathode. Another source of electrons for CP is from an external current DC power source. The negative terminal of power source is attached to the metal and positive terminal is attached to the sacrificial metal which is buried in soil or conductive back-fill material [3]. In addition to above said measures, the design of systems is quite influential in terms of corrosion resistance. Other than corrosion allowance, general design consideration must include (but not limited to) geometry, asset's interface with its neighborhood, aging and damage factors* etc. [59, 65].

1.5 Toughness

Fracture toughness is a measure of material's resistance to fracture from pre-existing crack and is dependent on many factors such as temperature, material composition, loading rate, material's microstructure, and geometry (thickness, dimensions) etc. It has been reported that the microstructure of materials can be tailored to improve their fracture toughness [66]. Mathematically,

$$K_{Ic} = \sigma\sqrt{\pi}\,\alpha B \qquad\qquad (1.13)\ [67]$$

Whereas,

KIc = fracture toughness

σ = applied stress

a= crack length

B = dimensionless factor (depends on geometry)

Figure 1.25 (a-d) shows various toughening phenomena in materials [68].

(a)   Crack deflection   (b)   Crack bridging

(c)   Uncracked ligament bridging   (d)   Microcracking
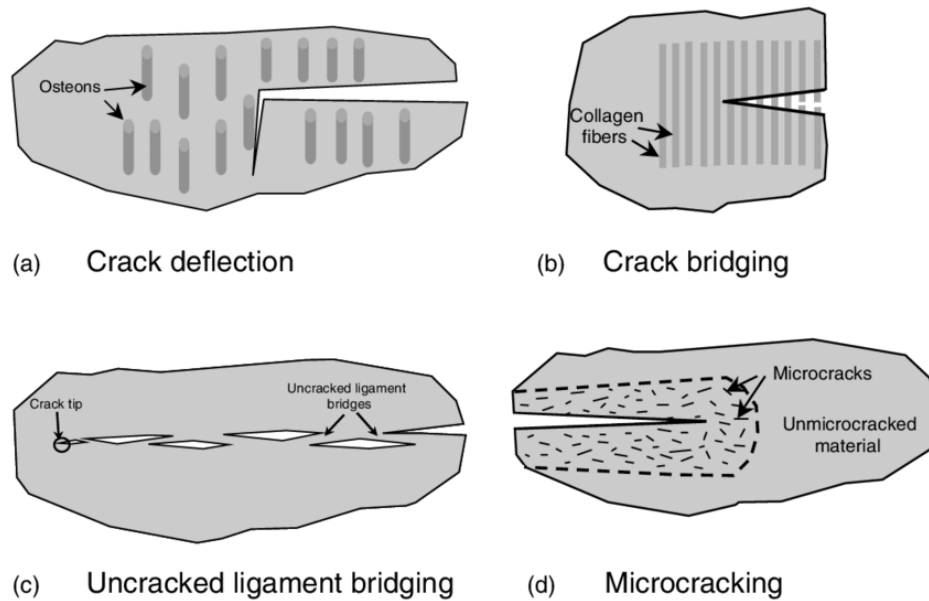
Figure 1.25 – Various toughening phenomena [68]

1.5.1 Crack bridging

Uncracked particles can bridge the walls of propagating cracks as the crack propagates mechanism is termed as crack bridging [66, 69]. As the bridges are loaded, they provide a restraining force against further opening of crack and thereby acting as a crack closure force. Such crack bridging is sometimes referred to as ligament or fiber toughening. It is a widely occurring phenomenon that can act over a wide range of scales [66].

1.5.2 Crack shielding

In crack shielding, the ductile particles cause the dissipation of crack driving energy; thereby impeding the propagation of cracks [70].

1.5.3 Crack deflection

Fracture toughness can be increased by causing a propagating crack to deviate out of crack's plane. Deflection may arise due to interaction with residual stresses, grain boundaries, ductile particle and secondary phases. Thermal treatment introduces residual stresses that behave as obstacles to the propagation of cracks [66]. Higher the deflection of crack's path, the higher would be the toughening due to localized suppression of crack [71]. Crack deflection has been reported to improve the fracture toughness of composites upto three times [72].

1.5.4 Process-zone toughening

It has been reported that defect structure may resist the propagation of cracks thereby improving the toughness of matrix. Energy dissipation near the crack tip (rather at surface separation) results in the toughening. Thus, the process zone which acts as energy-sink can lead to crack suppression or toughening of material(s). Two different types of process zone toughening namely stress-induced micro-cracking and transformation toughening [66].

1.5.4.1 Stress-induced micro-cracking

The microcracks may form near the crack tip due to stress field from loaded crack as well as due to residual stress from the elastic mismatch between the formed phases. The microcrack zone around the crack is termed as process zone. As crack propagates past the microcracks, a wake region builds up as shown in Figure 1.25 (d). Now the toughening happens as: portion of crack energy is used to create process zone of micro-cracks and the formed micro-cracks open up (in wake region) putting the compressive stress on the crack faces. Hence, both frontal zone and wake region constitute the toughening [66].

1.5.4.2 Transformation toughening

Strains induced during the transformation of materials (i.e. phases) may limit the crack opening, thereby increasing the toughness of material. Another scenario is the phase transformation from the stress field of propagating cracks which increases the volume of unit cells. Residual strains resulting from stress field impede the crack. An example is the phase transformation of martensite from tetragonal to monolithic zirconia from the stress field of propagating cracks [66].

Chapter 2 Experimental works

This chapter presents the various experimental tasks undertaken to complete the research study, such as preparation, characterization and testing of coatings. It also includes details of relevant equipment set up and operating conditions.

2.1 Graphene characterization

Graphene suspension (1 wt.%) was procured from US Research Nano-Materials Inc. Procured suspension was characterized using Raman microscope. To ensure the accuracy and consistency of Raman results, Raman testing of graphene samples from same lot/bottle was conducted under similar operating conditions (laser wavelength: 514 nm, laser excitation power: 1.25 mW) from three different lab facilities.

2.2 Coatings preparation

Cylindrical discs of API X70 steel (thickness: 6 mm, diameter: 15 mm) were ground-finished using SiC papers in three increasing grit sizes (240, 320 and 400). Ground-finished discs were subsequently polished using mono-crystalline diamond solution in three steps using diamond solutions of 9 µm, 3 µm and 1 µm, respectively. Surface-polished discs were dried using dry air and stored in a desiccator to avoid any surface oxidation.

Two electroless plating baths (volume: 1.0 L each) were prepared using industrial grade Ni-P plating solutions (make: Nichem Inc.[†]) and de-ionized water. The first bath was used for pre-coating without addition of graphene, while second contained graphene suspension to produce graphene enhanced Ni-P coatings. Plating solution comprised of de-ionized water, nickel sulfate as a salt and sodium hypophosphite as a reducing agent. Figure 2.1 shows the arrangement of electroless plating bath containing Ni-P plating solution. Three ml of graphene suspension (1 wt.%), after ensuring adequate Raman results, was added to one

of Ni-P solution/ bath to create Ni-P-30mg G solution. Same steps were repeated later for adding other volumes (6 ml, 10 ml, 30 ml) of graphene suspension to achieve the intended graphene concentrations of 60 mg/L, 100 mg/L and 300 mg/L in the plating solutions, respectively.   Polished substrates were submerged for 5 minutes in a heated alkaline solution (temperature: 75 - 80°C) with constituents as listed in Table 2-1.
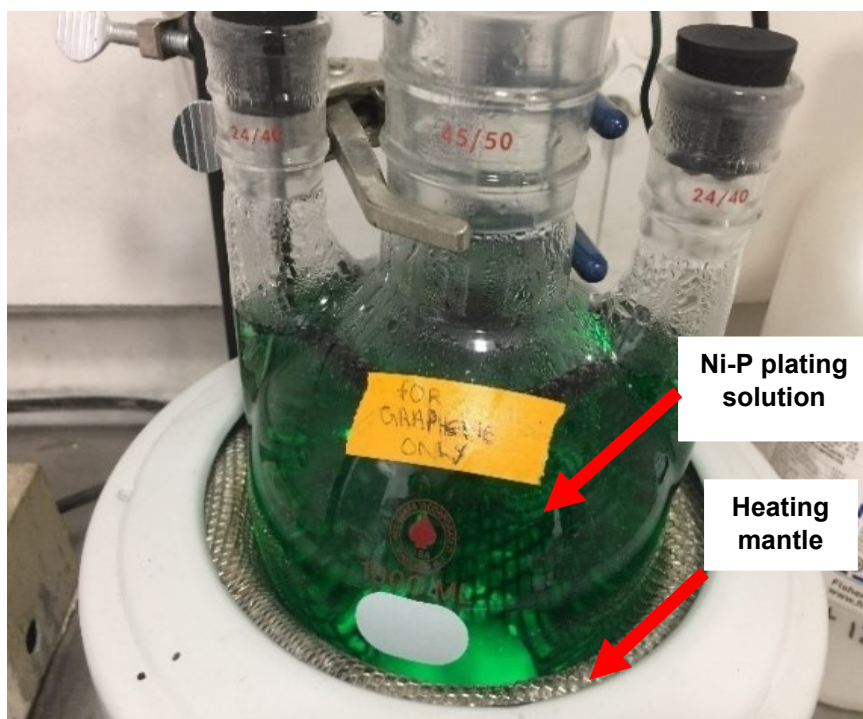
Figure 2.1 – Arrangement of electroless plating bath

Table 2-1 Plating solution composition

CHEMICAL NAME	CONCENTRATION
Sodium phosphate	30 g/L
Sodium carbonate	30 g/L
Sodium hydro oxide	50 g/L

Treated substrates were washed with de-ionized water followed by etching with 15 wt. % sulfuric acid for 10 sec. After etching, substrates were washed with de-ionized water and submerged in the first bath (under agitation at 200 rpm) where Ni-P pre-coating was carried out for 30 minutes. Meanwhile, graphene suspension was added in the other plating bath (under agitation at 100 rpm) in a concentration of 30 mg/L. After 30 minutes of pre-coating, samples were taken out of Ni-P plating bath and submerged in the graphene containing Ni-P bath. Coating was carried out in graphene enhanced plating bath for 3 hours (temp. 90° C), thereby yielding Ni-P-30mg G coating. Same steps were repeated for other plating compositions with 60 mg/L, 100 mg/L and 300 mg/L graphene in the plating solution. Ammonium hydro oxide was dripped in plating solution periodically to maintain pH in the previously reported optimum range of 4.6-4.8 [19]. For the purpose of erosion, corrosion and erosion-corrosion tests, electroless coating was performed on AISI 1018 steel substrate (instead of API X70), using similar plating parameters. Figure 2.2 shows the dimensions of substrate, whereas details on shape and material of various substrates are shown in Table 2-2.

In the current research work, the effect of high stirring speed (500 rpm) was also observed on trial basis that produced severe gouging marks on the surface of coating. This is most likely due to the impact of harder and energized graphene platelets in the plating bath. Figure A1 in the appendix reveals the coating surface damage from the gouging effect of graphene platelets at high stirring speeds.
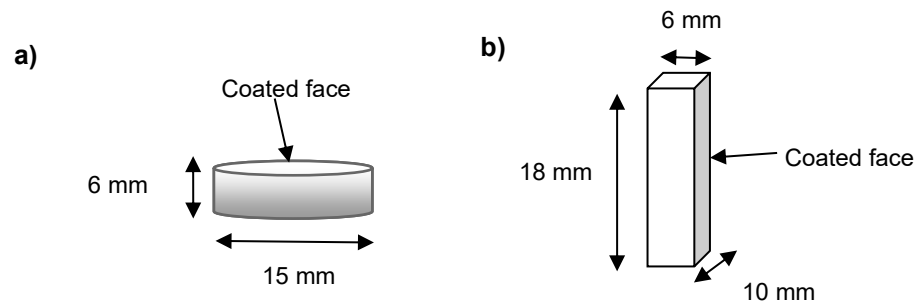
Figure 2.2 – Dimensions for typical a) cylindrical coated sample for characterization (except SPEC test) and b) rectangular coated sample for SPEC test

Table 2-2 Attributes of Substrates

Coating Characterization	Specimen Shape	Substrate Material
Surface topography	Cylindrical	AISI 1018 steel, API X70 steel
Scratch testing	Cylindrical	API X70 steel
Hertzian Indentation testing	Cylindrical	API X70 steel
Static Corrosion	Cylindrical	AISI 1018 steel
Slurry-pot erosion-corrosion	Rectangular	AISI 1018 steel

2.3 Coatings characterization

2.3.1 Optical and micro-structural testing

Topographic analyses of all coating compositions were carried out over a surface area of 16 mm^2 using a very high precision laser confocal microscope (make: Keyence VK-X1000). Topographic scans employing laser confocal microscope were performed as per standard guidelines (ISO 25178-602) for surface texture analysis [73]. Surface images were captured at higher magnifications followed by stitching, 3D topographic imaging and surface roughness measurements. SEM analyses were performed on cross section samples using Hitachi S-4700 coupled with EDS under scanning mode at 15.0 KV to visualize the particles (Ni, P, Graphene) distribution and capture images representative of the coating. Chemical composition of coating, elemental distributions were determined using area EDS and line

scan mapping, respectively. SEM and point EDS checks were also employed on the surface cracks (post tribological characterization) to investigate the existence and nature of toughening mechanisms (if any) in the coatings.

2.3.2 Micro-Vickers hardness

Micro-hardness was measured on cross sections by Vickers hardness tester employing diamond pyramid indenter (under 100 g load) as per guidelines of applicable standard [74]. Indent sizes were measured using microscope (mag. 1000x) to quantify the diagonal lengths for subsequent calculation of hardness values. To account for errors and minimize the possible deviations of hardness readings, three different indents were made on each cross section followed by averaging of indent size (diagonal length). The average indent size was incorporated in below Equation (2.1) to calculate the Vickers hardness (H_v) as [74]:

$$HV = 1.8544P \div d^2 \qquad (2.1)$$

2.3.3 Hertzian-type indentation tests

Hertzian-type indentation test was used to induce cracks in the coatings to subsequently understand the toughness and failure modes of coatings [75]. For this, indentation tests were performed on the polished substrate (API X70 steel), coatings of similar thickness (~50 μm) except Ni-P-300mg G; for which the maximum achieved thickness was around 20 μm. All the specimens were subjected to similar range of loading levels (1000 N, 1500 N, 2000 N and 2500 N) using a spherical indenter in the indentation testing apparatus (PASCO Inc.). The test apparatus was coupled with AE signals probe to account for energy released from the coating during indentation process. The initial crack load for each coating was measured accordingly using intensity of AE signals and corresponding load value on load-displacement curves.

2.3.4 Scratch test

Scratch test were conducted on the polished substrate (API X70 steel) and coatings. All the samples were subjected to multiple passes (10, 20 & 40 passes) scratch tests under an indenter load of 39.2 N for a sliding distance of 5 mm. The specimens were also subjected to an increasing load (4.9 N - 44.1N) scratch for a length of 10 mm. Figure A1 in appendix shows the map and parameters of all scratches that were produced on the coating sample. Scratch tests were conducted using UMT (Universal Micro-Tribometer) tester (Bruker Inc.) under diamond spherical tip indenter coupled with AE (acoustic emission) sensor in order to account for energy released (due to cracking) during scratch testing process [76]. AE signals for increasing load scratch tracks were plotted against time to measure the intensity of AE signals; and account for crack's initiation along with relevant crack load (i.e. initial crack load). Further microscopic checks on the surface of increasing load scratch tracks were performed to check the location and morphology of crack, and double against the initial crack load value that was obtained from AE signals. Also, average COF (coefficient of friction) for each scratch track was measured during scratching process. Optical microscopic checks were performed on constant load scratch tracks to measure scratch track's width for subsequent calculation of volume loss [77] and wear rates. Figure A6 in appendix shows the micrographs for various scars on all coating specimen. Tribological attributes (wear rate, initial crack load, COF) and toughening effects were investigated using UMT tester coupled with AE sensor.

2.3.5 Slurry pot erosion-corrosion (SPEC) test

Prior to slurry pot erosion-corrosion (SPEC) testing, edges of all samples were ground smooth perpendicular to each other to remove any chamfers from the corners. An electrical contact was attached to each sample for electrochemical assessment and control. All faces

of samples (except the test surface) were covered with epoxy. The samples were mounted

in SPEC tester as per schematic arrangement shown in Figure 2.3.
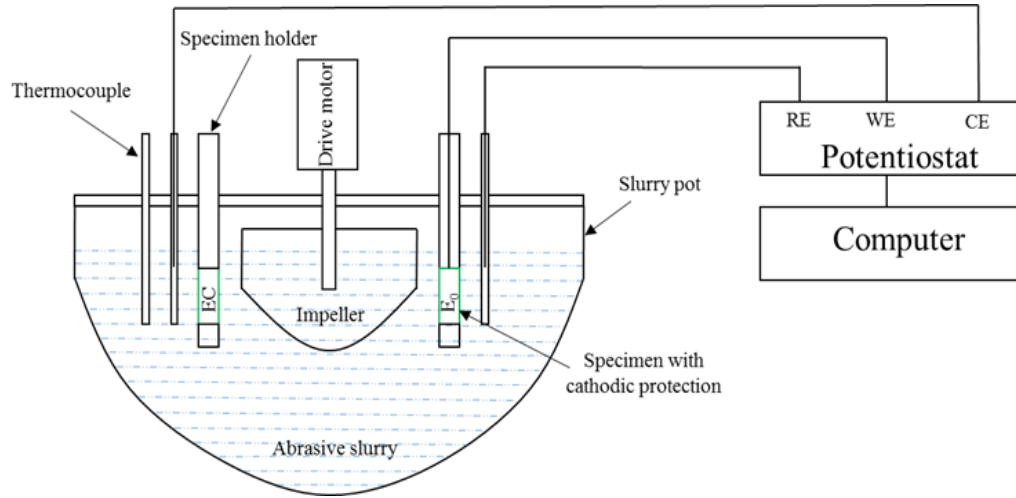
Figure 2.3 - Schematic arrangement for slurry pot erosion-corrosion tester

The slurry pot erosion-corrosion unit consists of 4-litre glass vessel to hold the slurry, a

neoprene-lined impeller that is rotated to impel the slurry against the test surfaces, a

heating/cooling system (chiller) and a three-electrode cell with a Gamry PC4/750

potentiostat to allow for electrochemical assessment as well as cathodic protection control.

Electrochemical tests were conducted in-situ (working electrode) vs. SCE (saturated

calomel electrode) and Pt as counter electrode. Slurry pot erosion-corrosion test

parameters are tabulated in Table 2-3.

Table 2-3 Slurry pot erosion-corrosion (SPEC) test parameters

Slurry composition	AFS 50-70 silica sand (35 wt.%) + NaCl (3.5 wt. %)
Impeller speed	900 rpm
Slurry temperature	45 °C
Test duration	6 hr
Erodent impact velocity at 900 rpm	0.26 - 2.21 ms^{-1}

The erodent particle-target impact velocities (tabulated above) were determined by briefly exposing polished soft metal (pure Cu, annealed at 450°C) specimens in SPEC test to dilute slurry of spherical particles (60-70 glass bead, 212-300 μm). The normal particle impact velocity was then calculated from the depth of the resulting craters [78-79]. Experimentally derived normal impact velocity during SPEC test is 0.26-2.21 ms^{-1} [80]. Figure 2.4 shows the SEM micrograph of AFS 50-70 silica sand particles (212-300 μm).
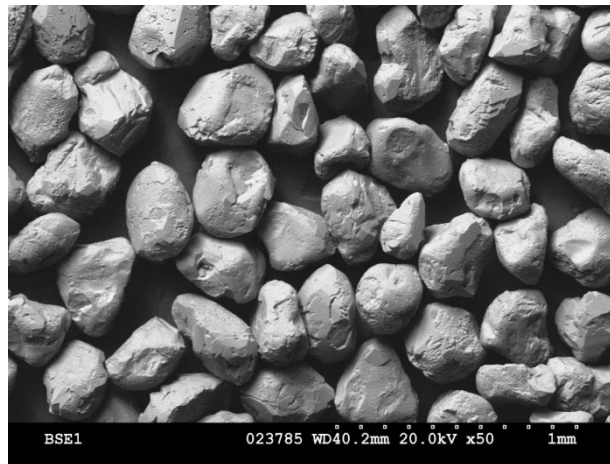
Figure 2.4 - SEM micrographs of AFS 50-70 sand particles

Erosion-corrosion test was conducted by exposing the sample to the slurry as per above tabulated parameters. Pure erosion test was conducted using similar arrangement, but

samples were cathodically protected to resist the corrosion. On the other hand, pure corrosion tests under flowing condition were conducted using 3.5 wt.% NaCl solution (without the abrasive particles), while AFS 50-70 silica was subsequently added to the electrolyte to account for the effect of erosion-enhanced corrosion.

The material loss(es) were measured by weighing samples on a high precision micro-balance (having accuracy of 0.01 mg) before and after SPEC test. Material loss rates were calculated and reported in $cm^3/h/cm^2$ using following equation (2.2):

$$Material\ loss\ rate\ (K) = \frac{Mass\ loss}{Density \times Surface\ area \times Test\ duration} \tag{2.2}$$

The erosion-corrosion synergy values were determined according to the criteria of applicable standard ASTM G119-09, where the total material loss under erosion-corrosion conditions (*Kec)*, is related to the synergistic component (*Ks*) by equation (2.3) as [63]:

$$Kec = Keo + Kco + Ks \tag{2.3}$$

Where, *Kec* = total material loss rate due to erosion-corrosion

Keo = material loss due to pure erosion

Kco = material loss rate only due to pure corrosion

and *Ks* = synergy

Furthermore, total material loss rate (*Kec*) can also be divided into the following components:

$$Kec = (Keo + \Delta Ke) + (Kco + \Delta Kc) = Ke + Kc \tag{2.4}$$

Whereas, K_e = total erosion rate, K_c = total corrosion rate, ΔK_e = corrosion-enhanced erosion and ΔK_c = erosion-enhanced corrosion. Equation (2.4) provides more detailed information

on key contributors to E-C loss. Synergism (*Ks*) and its various components can be calculated/expressed by combining equation (2.3) and (2.4) as:

$$Ks = \Delta Ke + \Delta Kc = Kec - (Keo + Kco) \qquad (2.5)$$

$$\Delta Kc = Kc - Kco \qquad (2.6)$$

$$\Delta Ke = Ks - \Delta Kc \qquad (2.7)$$

2.3.6 Potentiodynamic polarization test

All coatings and ground-finished (600 grit) 1018 steel substrate were characterized for their potentiodynamic behavior using potentiostat as per guidelines of governing standard [81]. Prior to testing, all samples were cleaned with acetone to remove any surface containments followed by rinsing with de-ionized water and dry air blowing. Samples were placed in a corrosion cell filled with 3.5 wt.% NaCl solution. SCE (saturated calomel electrode) was used as reference and platinum as counter electrode. Figure 2.5 shows the arrangement of PD polarization test cell, whereas test parameters are given in Table 2-4.

Table 2-4 Parameters for static corrosion test

Test temperature	Room temperature
Duration for OCP	90 minutes
Scan rate	0.167 mV/sec
Cathodic polarization volts	- 0.25 V (below OCP)
Anodic polarization volts	+ 0.25 V (above OCP)

Coating densities (ρ) were calculated using wt. % and density of each constituent element in the coating matrix. While equivalent weights *(EW)* were calculated using below equation (2.8) as [62]:

$$EW = \frac{1}{\left\{\frac{f_1 \times e_1}{z_1}\right\} + \left\{\frac{f_2 \times e_2}{z_2}\right\} + \left\{\frac{f_3 \times e_3}{z_3}\right\}} \qquad (2.8)$$

Where *f* = Weight fraction of constituent element (wt. % from EDS results)

e = Ion exchanging capacity of constituent element (e.g. 2 for Ni, 5 for P)

Z = Atomic weight of constituent element

Corrosion current i.e. *Icorr* was calculated from the slope of Tafel plots, while corrosion current density *icorr* (i.e. current density of opposing reactions at reversible potential) was calculated using following equation:

$$i_{corr} = \frac{Icorr}{Area}$$ (2.9)

CR (corrosion rate) was calculated according to below equation (2.10) as [25]:

$$CR = \frac{0.00327 \times i_{corr} \times EW}{\rho}$$ (2.10)

Whereas, improvement in corrosion resistance (if any) for graphene coatings (i.e. Ni-P-G) were calculated using below Equation (2.11):

$$Increase\ in\ corrosion\ resistance\ =\ \{(CR\ for\ Ni-P) - (CR\ for\ Ni-P-G)\}\ /\ (CR\ for\ Ni-P) \times 100\ \% \quad (2.11)$$
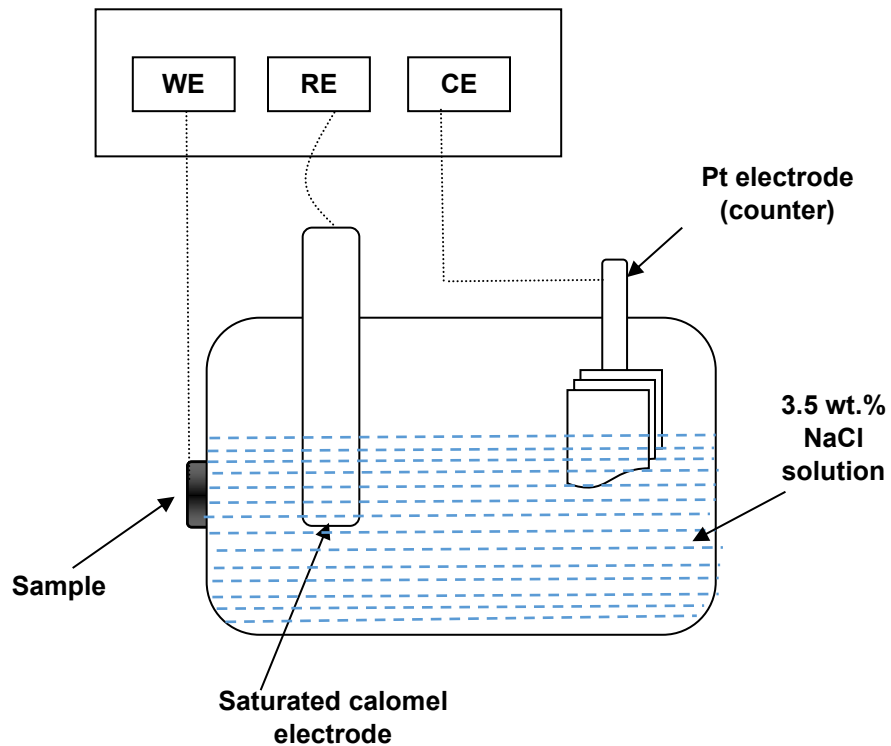

Figure 2.5 - Arrangement of PD polarization test cell

2.3.7 Solid particle erosion test

Erosion due to solid particles is a common degradation in the hydrocarbon, energy and aerospace applications. There are numerous processes in hydrocarbon processing industries where the handling of powders such as catalyst (in reactors, regenerators) requires fluidization by the impact of pressurized air. Impingement of powdered catalyst (or agglomerates/ clusters) at higher velocities (especially during upset conditions) may cause the erosion of the metals. Some common examples are the erosion of air circulation coils and cyclones within the reactor-regenerator system of HOFCC (high olefins fractional catalytic cracking) unit, respectively. The assets in upstream oil and gas industry are also prone to erosion damage. An example of such an instance is the erosion of pipes and tubing in SAGD (steam assisted gravity drainage) systems due to the impact of sand particles.

All coating samples and substrate were characterized for solid particle erosion behavior using combination of two different air velocities and four different angles of attack (30º, 45º, 60º and 90º), respectively using the arrangement shown in Figure 2.6. The WC balls were used as solid particle and placed in the particle housing. The coating sample was mounted as a target on adjustable vice, adjusting it to the required angle and keeping it aligned to barrel. The pressurized air was introduced in the particle housing, via pressure regulator and solenoid valve that forced the WC particle. The pressurized particle after passing through the transparent polycarbonate barrel, strike the target sample. Two different air pressures (30 psi and 60 psi) were used corresponding to the velocities as 35 ± 3 ms^{-1} and 52 ± 3 ms^{-1}, respectively. The samples were analyzed microscopically to account for cracks and applicable wear mechanisms.
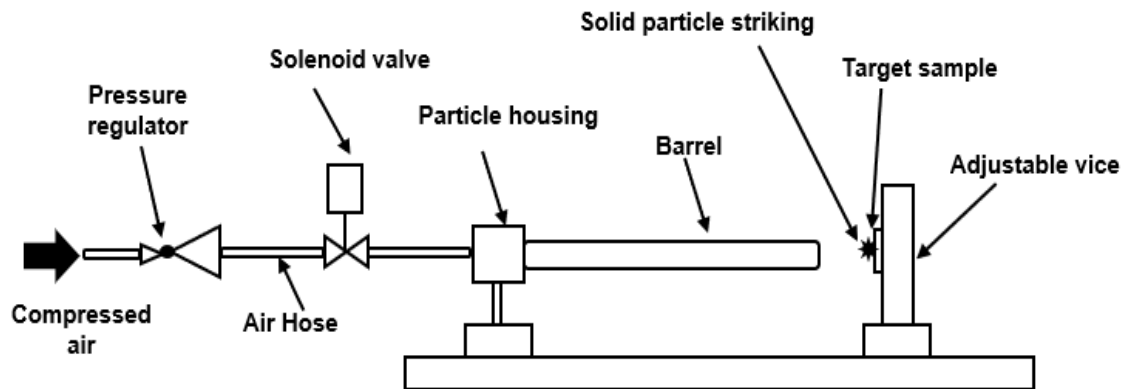
Figure 2.6 - Schematic arrangement for solid particle erosion test setup

Chapter 3 Results and Discussion

This chapter presents the results from various characterization works and offers the reasoning for various microstructural, tribological and corrosion behaviors.

3.1 Graphene identification

Figure 3.1 shows the resulting spectrum of graphene that contains three different peaks (D, G & 2D) obtained from the Raman test. Position (i.e. wavenumber) value of D-peak (at X-axis) was found as 1348 cm^{-1}; while intensity (at Y-axis) of D-peak was found as 10,769 a.u. On the other hand, positions of G-peak and 2D peaks were found as 1595 cm^{-1} and 2681.46 cm^{-1} respectively.
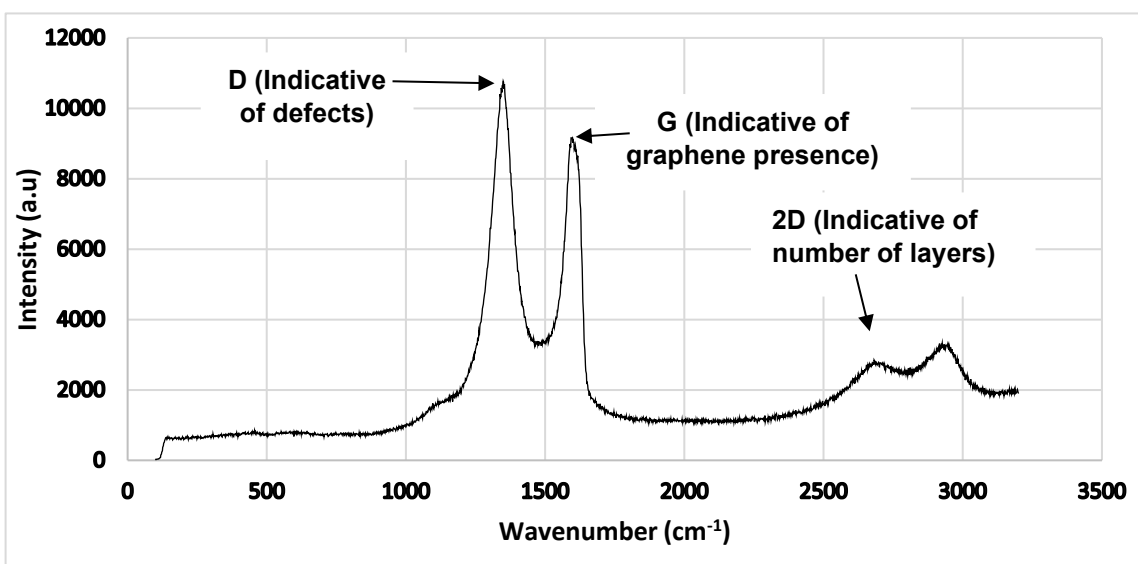
Figure 3.1 - Raman spectrum of 1wt.%graphene suspension using 514nm laser wavelength at 1.25 mW excitation power
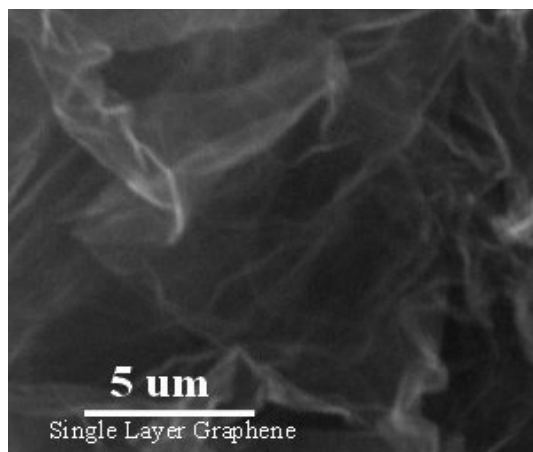
Figure 3.2 - SEM micrograph of single layer graphene [82]

Intensity, shape and location (wave-number) of peaks in a Raman spectra are meant to provide a valuable evidence to fairly predict presence of graphene or graphite, existing defects in nano-structure (edge defect, basal planes etc.), number of layers as well as synthesis method likely used for producing the graphene sample under study [83].

Number of layers can be estimated from the location (wave-number value) on X-axis that corresponds to highest point of 2D peak. Referring to Figure 3.1, position (wavenumber) of D-peak for graphene sample (1348 cm^{-1}) is less than reported value for graphite D-peak (1355 cm^{-1}); thereby eliminating existence of any graphite in the suspension [84]. Moreover, this D-peak position value is closer to that reported by the supplier as 1352.7 cm^{-1} [83]. Intense D-peak (10,769 a.u) is an indicative of the fact that this sample is graphene; along with certain disorder/defects in its nanostructure [85, 86]. Defects are generally attributed to the method of graphene synthesis whereas, the highest quality and defect free graphene is produced by CVD (chemical vapor deposition). Position of G-peak (1595 cm^{-1}) that is closer to reported value for GO (graphene oxide) i.e. 1590 cm^{-1} and to that reported by the supplier (1589.0 cm^{-1}). The close value of G-peak position to that for GO is an indicative of the fact that this graphene is produced by reduction of GO. Position (wavenumber) of 2D

peak is 2681.46 cm^{-1} which is in proximity to that for single-layered graphene (2680 cm^{-1}-2681 cm^{-1}) [85, 86]. Figure 3.2 shows SEM micrograph of single layered graphene platelet [82].

3.2 Microstructural attributes

The deposition rates for all coating compositions were found to be in the proximity 16-20 µm/hr. Figure 3.3 (a) shows typical cross section of coating revealing a uniform coating thickness on the substrate. Figure 3.3 (b) shows the distribution of graphene in Ni-P-30mg G coating using line scan EDS analysis. SEM and area EDS on the top surface of the coating are shown in Figure 3.3 (c) and 3.3 (d), respectively. It's evident that graphene nano-platelets are uniformly distributed throughout the coating matrix without any significant agglomeration or clustering. Micrographs for cross-section of other coating compositions are shown in Figure A3 in Appendix.

Figure 3.4 summarizes the measured wt. % and volume % of graphene within coating matrix (as measured using area EDS scans). It is evident that the ternary coating matrix (Ni-P-graphene) has achieved the highest concentration (18 vol. %) of graphene for a graphene concentration of 30 mg/L in the electroless plating bath. The amount of graphene in coating matrix drops as the graphene concentration in the plating bath is increased to 60 mg/L and 100 mg/L, respectively. It's because higher concentration of graphene increases the possibility of inter-platelets collisions. These collisions reduce the energy of platelets that in turn stay suspended in the solution instead of getting incorporated in Ni-P coating matrix. This behavior of graphene concentration variation is similar to that earlier reported by Tamilrasan [16], where 50 mg/L of graphene in the plating bath achieved higher concentration in the coating matrix than that for 75 mg/ L and 100 mg/L.
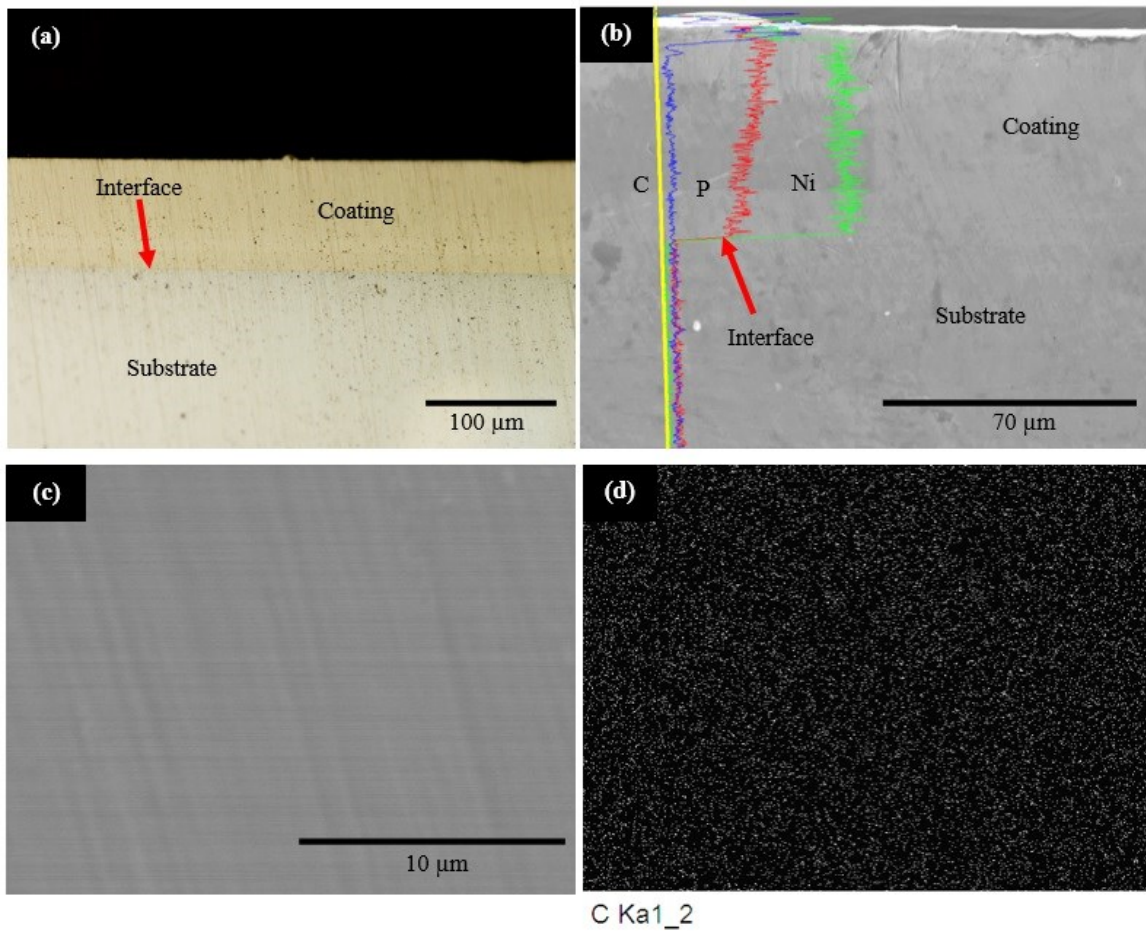
Figure 3.3 - (a) Optical micrograph of cross-section (b) line scan EDS (c) SEM micrograph on top surface of Ni-P-30mg G coating and (d) EDS map of (c)
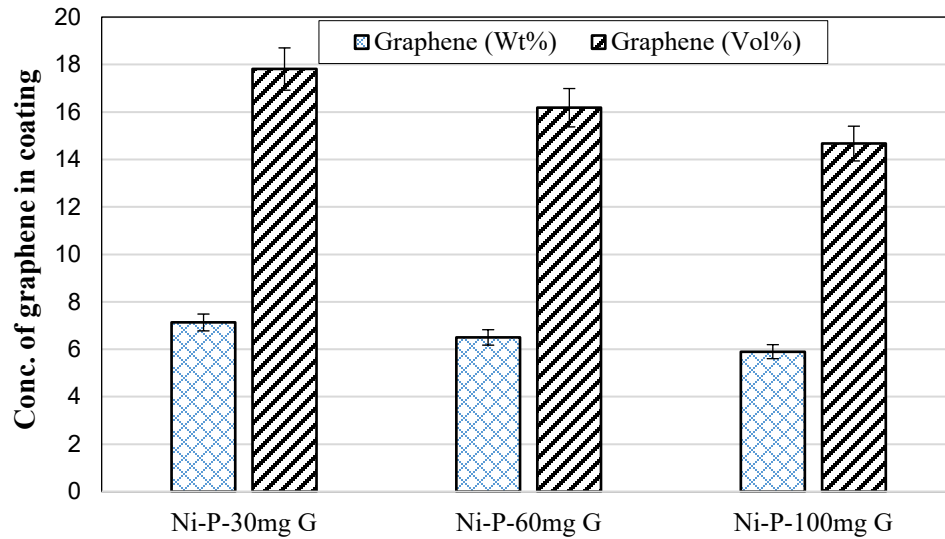
Figure 3.4 - Graphene conc. (wt. % & vol. %) for various coating compositions

3.3 Vickers hardness

Micro-hardness variation for all coatings is summarized in Figure 3.5. It's evident that hardness of Ni-P coating matrix has increased in the presence of graphene. Vickers hardness of Ni-P coating is 5.2 GPa. It is consistent with previously reported hardness by C. Wong [51, 87]. Ni-P-30mg G coating, that contains 18 vol. % of graphene nano platelets in the matrix, exhibits the highest hardness among all coating compositions due to dispersion strengthening mechanism [3]. The coating hardness reduces as graphene concentration in the coating matrix is reduced to 16 vol. % and 15 vol.% in Ni-P-60mg G and Ni-P-100mg G coatings, respectively. This hardness value of Ni-P-30mg G coating (7.50 GPa) is consistent with hardness value reported by Tamilrasan as 7.46 GPa for a graphene concentration of 9.36 wt. % in the coating matrix [16]. Also, the trend of hardness variation with graphene concentrations in the coating matrix is comparable to that reported earlier in literature [16].
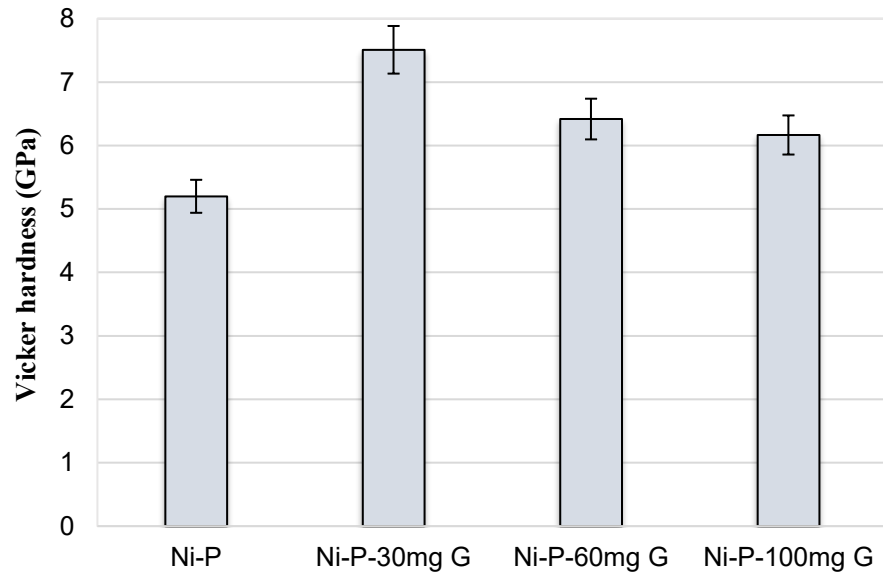
Figure 3.5 - Micro-Vickers hardness trend for all specimens

3.4 Deposition rates

Deposition rates variation with graphene concentration in plating bath is shown in Figure 3.6. The deposition rate of Ni-P is around 17-18 µm/ hour which is almost consistent with values reported earlier in literature [19]. Here, the addition of graphene in a concentration upto 100 mg/L has a slight retarding impact on the deposition rates as the thickness values are found in proximity for all compositions. On the other hand, addition of graphene upto 300 mg/L results in lower thickness and consequently lower deposition rate.
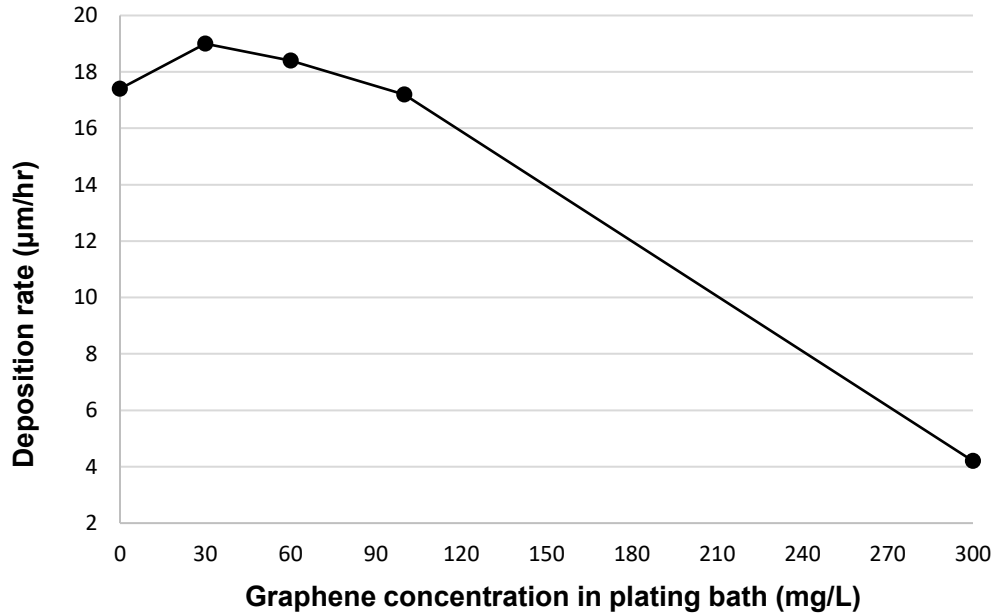
Figure 3.6 - Deposition rate variation with graphene content in Ni-P electroless plating bath after 3 hours of plating time

3.5 Surface topograhy

Typical 3D topographs for Ni-P & Ni-P-100mg G coatings are shown in Figure 3.7 (a) and 3.7 (b), respectively. 2D surface scans (over an area of 16 mm^2 under 100x mag.) are shown in Figure 3.7 (c) and 3.7 (d) for Ni-P and Ni-P-100mg G, respectively. Ni-P coating exhibits uniformly distributed porosities on the surface as observed in Figure 3.7 (a) and 3.7 (c). This is mainly because of hydrogen evolution during oxidation of sodium hypophosphite in electroless coating process as discussed earlier in Equations (1.2) through (1.5) [19]. On the other hand, Ni-P-100mg G has considerably less number of pores compared to Ni-P. It's reported that graphene platelets have tendency to conform to any shape of voids and underlying surface during deposition due to van der Waal's interactions [88]. So, the graphene platelets have likely filled the voids among and over the pores due to van der Waals interaction. Therefore, the presence of graphene (by 15 vol. %) in Ni-P-100mg G has reduced rough features and porosities as shown in Figure 3.7 (b) and 3.7 (d).
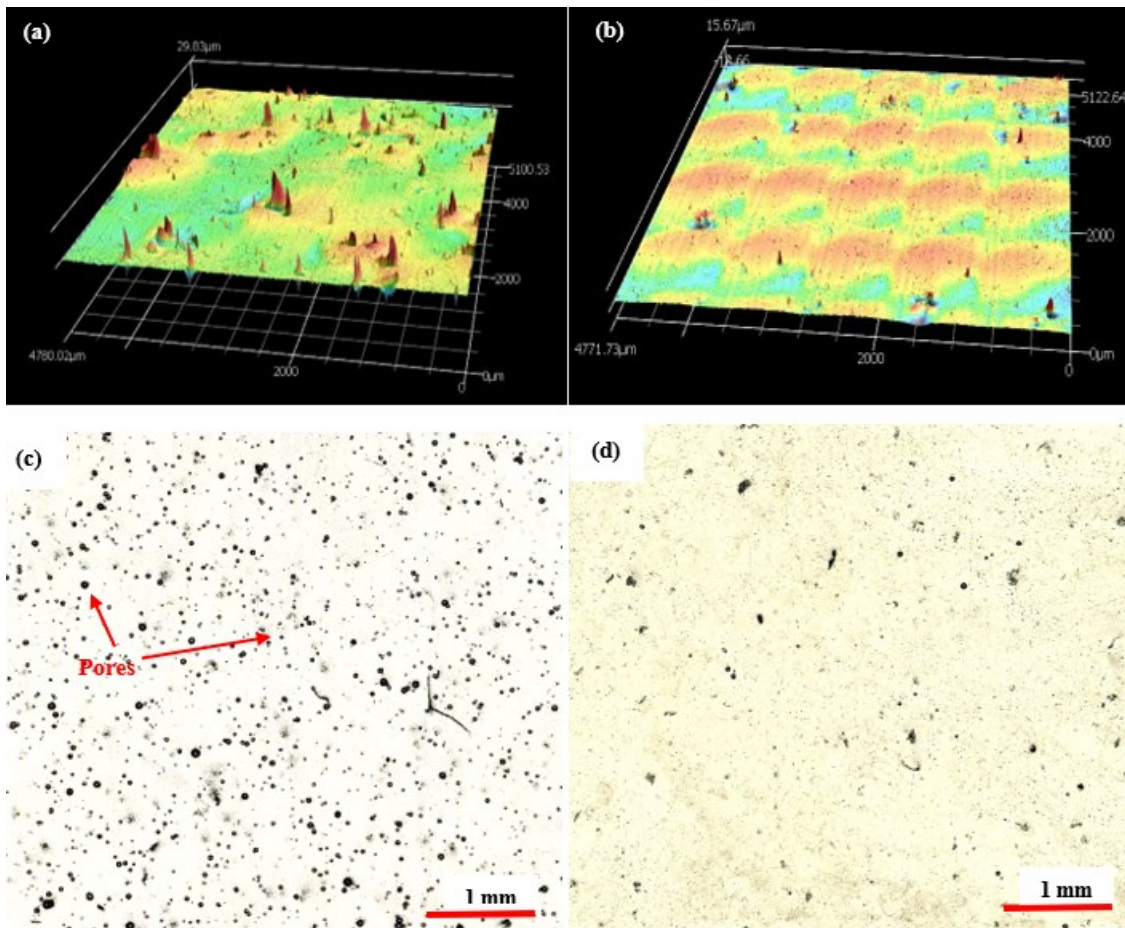
Figure 3.7 - 3D surface topographs (aspect ratio, 1:1:1400) for (a) Ni-P (b) Ni-P-100mg G and 2-D surface micrographs (mag. 100x) for (c) Ni-P and (d) Ni-P-100mg G

Variation of surface roughness with graphene concentration (vol. %) in the final coating matrix (produced by 3 hrs of plating) is shown in Figure 39 (a). It's noticeable from Figure 3.8 that graphene concentration of 15 vol. % achieves best surface smoothness i.e. for Ni-P-100mg G among all coating compositions. Further increase of graphene in coating matrix in turn increases the surface roughness. This increase in roughness is because graphene nano-platelets have very low density compared to remaining matrix; and excess amount of graphene nano-platelets will reside on the surface rather filling the voids from the release

of hydrogen gas. Hence, surface roughness of coatings increases with increase in graphene concentration above 15 vol. %.

Figure 3.8 (b) shows surface roughness trends w.r.t two plating bath parameters i.e. graphene concentration as well as plating time. It's evident that with increase in the plating time the surface roughness increases. This is the result of reduced reaction kinetics that leads to porosities. Also, with increased plating time, the deposition thickness increases that in turn retards the smooth deposition of next particle (i.e. Ni, P, graphene etc.). Figure A4 and A5 in the appendix summarize the 3D topographs for different plating times and compositions. For the higher stirring speeds, the harder graphene platelets lead to gouging effects rather any deposition thereby producing scars on the coatings as shown in Figure A2 in Appendix.

(a)

(b)
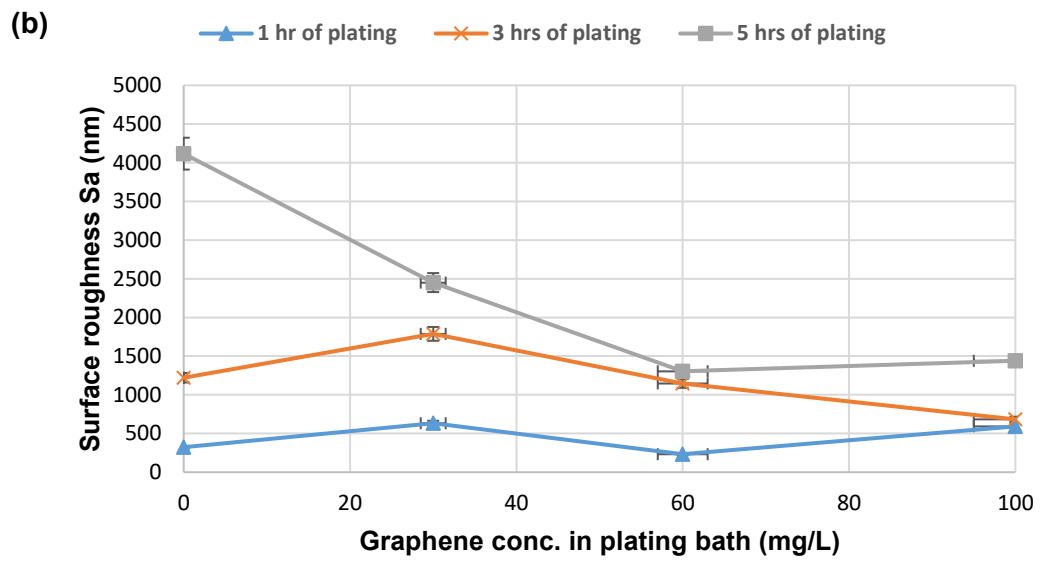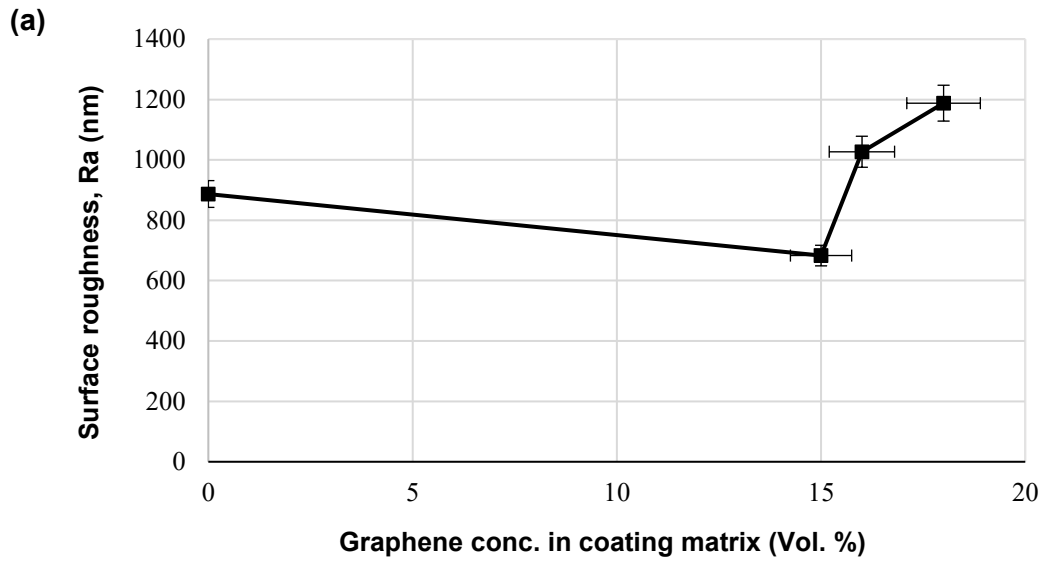
Figure 3.8 - Surface roughness variation(s) w.r.t (a) various graphene concentration in the final coating matrix after 3 hrs of plating time (b) plating bath parameters (graphene concentration and plating time)

3.6 Scratch and wear behavior

Figure 3.9 (a-d) shows the scratch track (length: 10 mm), initial cracks (indicated by circles) and corresponding AE signals (indicated by dotted lines) under increasing indenter load for Ni-P, Ni-P-30mg G and Ni-P-300mg G coatings, respectively. Initial crack loads for all coatings as well as substrate were calculated by incorporating the measured value of X (i.e. distance from starting point to first crack location) in the equation as: 1st crack load = (X / total scratch length) x maximum applied load. Whereas, total scratch length is 10,000 µm and maximum applied load is 4.5 Kg (equals 44.1 N). Figure 3.10 shows the first crack load for all coatings with similar thickness (~50 µm). Multiple readings of track width were taken along the full length of multiple passes scratch tracks (under 39.2 N load) using optical microscope; followed by averaging to minimize the error in the final value of track width. Volume loss was calculated assuming ideal scratch shape and incorporating average track width in below Equation (3.1) as [77]:

$$\text{Scratch volume} = D^2t / 8 \, [2Sin^{-1}(b/D) - Sin\{2Sin^{-1}(b/D)\}] \tag{3.1}$$

Here D is the diameter of indenter tip (0.4 mm), b is the average value of scratch track's width and t is the length of scratch track or indenter's travel distance (5 mm). Calculated volume losses were plotted against indenter's travel distance in order to calculate the wear rate. Wear rates were calculated from slope of graphs (volume loss vs indenter travel distance) for each coating. Figure 3.11 shows the wear rate variation for different compositions of coatings having same plating thickness (~ 50 µm). Micrographs for various scratch tracks are shown in Figure A6 of appendix section.

3.6.1 Initial crack load

It is evident from Figure 3.10 that the load required to create first crack has initially increased with the introduction of graphene nano-platelets (30 mg/L). Through simultaneous analyses of the crack morphology and intensity of AE signals in Figure 3.9 (a-d), it is evident that cracks in Ni-P-30mg G coating are much suppressed than those in Ni-P coating. Cracks for Ni-P-30mg G coating in Figure 3.9 (b) are confined within edges of wear track. While cracks for Ni-P coating in Figure 3.9 (a), have extended beyond the sides of track and appear to be Hertzian-type cracks. Further addition of graphene nano-platelets (60 mg/L and above) in plating bath seems to have reversing effect on the first crack load, where we can see the considerable reduction in the load for causing the first crack. Here the highest initial crack load (as well as cracks suppression) in Ni-P-30mg G than all other coating compositions is the result of highest graphene concentration in the coating matrix (18 vol. %). The ability of coating matrix to resist cracks declines as the graphene concentration in the final coating matrix is reduced.

It is worth noting that Ni-P-300mg G coating doesn't show any evidence of cracking under maximum applied load of 44.1 N. This absence of cracking in Ni-P-300mg G coating is a consequence of its lower thickness that makes it behave like a flexible thin film whereby indenter load is supported by underlying substrate. Also, the EDS analysis of scratch track of Ni-P-300mg G revealed dominant Fe peaks; that is an evidence of the situation where the indenter was exposed to underlying substrate during scratching process. Same is the case with un-plated API X70 steel substrate where no cracking was found even under the maximum applied load of 44.1 N. This performance of un-plated steel substrate is due to its inherent ductility that absorbs indenter's energy. The microscopic results further conformed to the AE signal data regarding the presence as well as intensity of cracks. In case of Ni-P-

300mg G and X70 steel sample, AE data was comprised of low background noise rather than spikes that can correspond to cracking (if any).
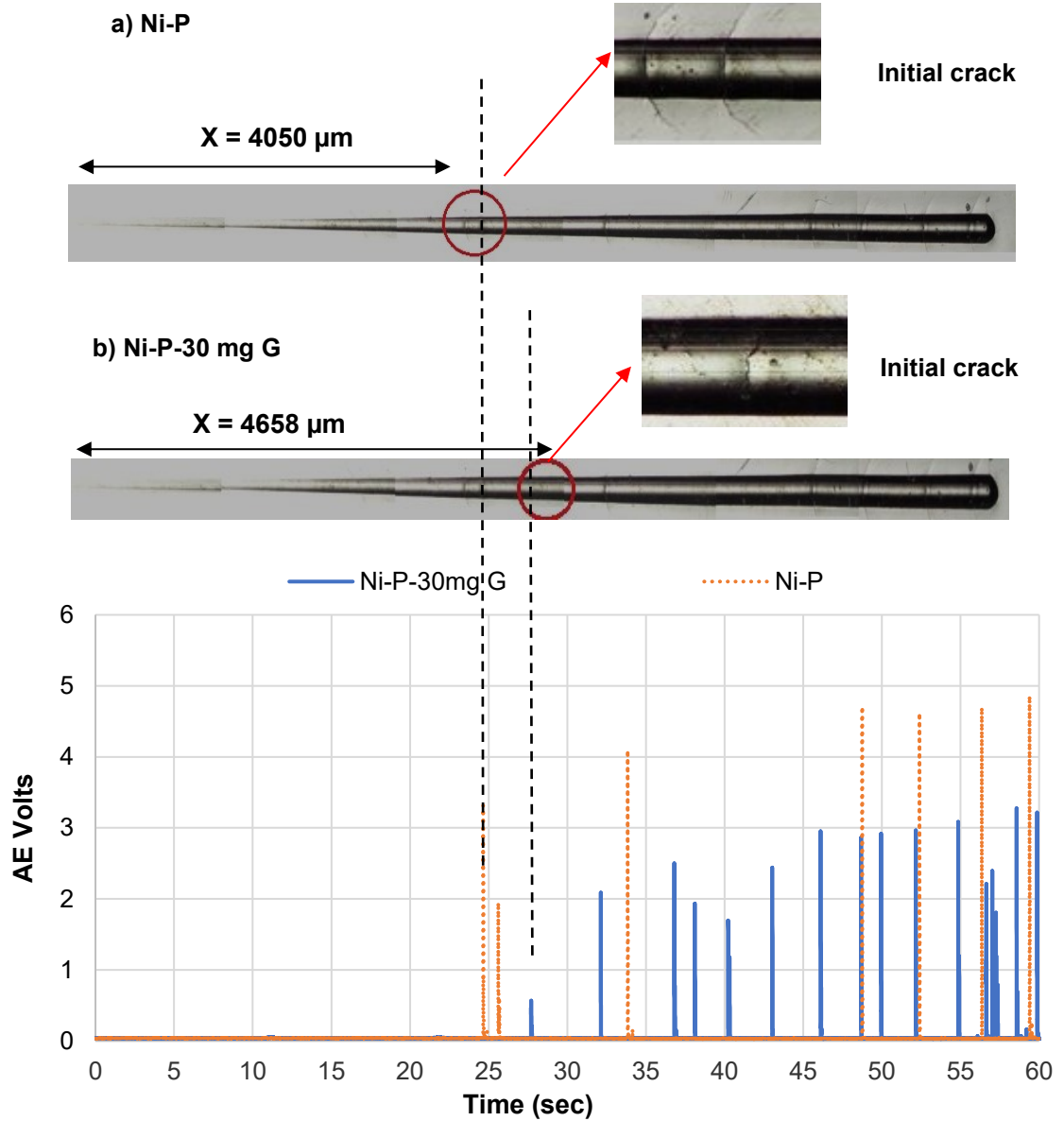
Figure 3.9 - 10 mm long scars under progressive indenter load (4.9 N – 44.1 N) for a) Ni-P b) Ni-P-30mg G and c) corresponding AE signals (volts) for cracks
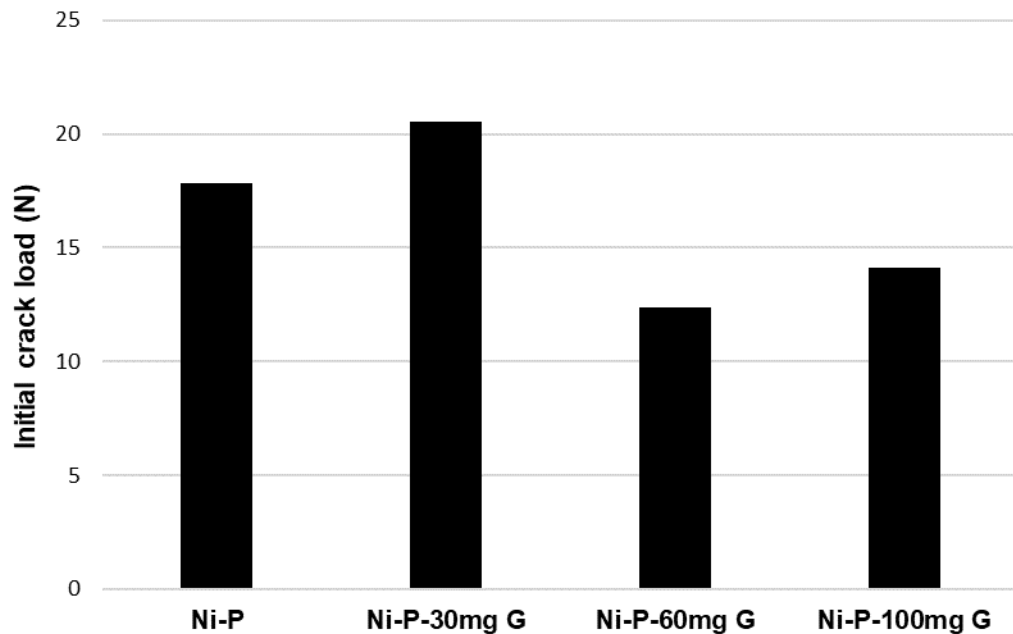
Figure 3.10 - Initial crack load under single point progressive load (4.9 N – 44.1 N) scratch test

3.6.2 Wear rate

Figure 3.11 shows the wear rate trend for different coating compositions. Again, Ni-P-30mg G has the least wear rate than other coatings and attributed to simultaneous increase in the hardness and toughness of coating matrix due to the highest graphene concentration (17.81 Vol. %). The wear rate seems to increase further as graphene concentration is increased in the plating bath. This can be attributed to defects from some agglomeration of graphene resulting from high graphene concentrations of 60 mg/ L and 100 mg/L, respectively in the plating bath.
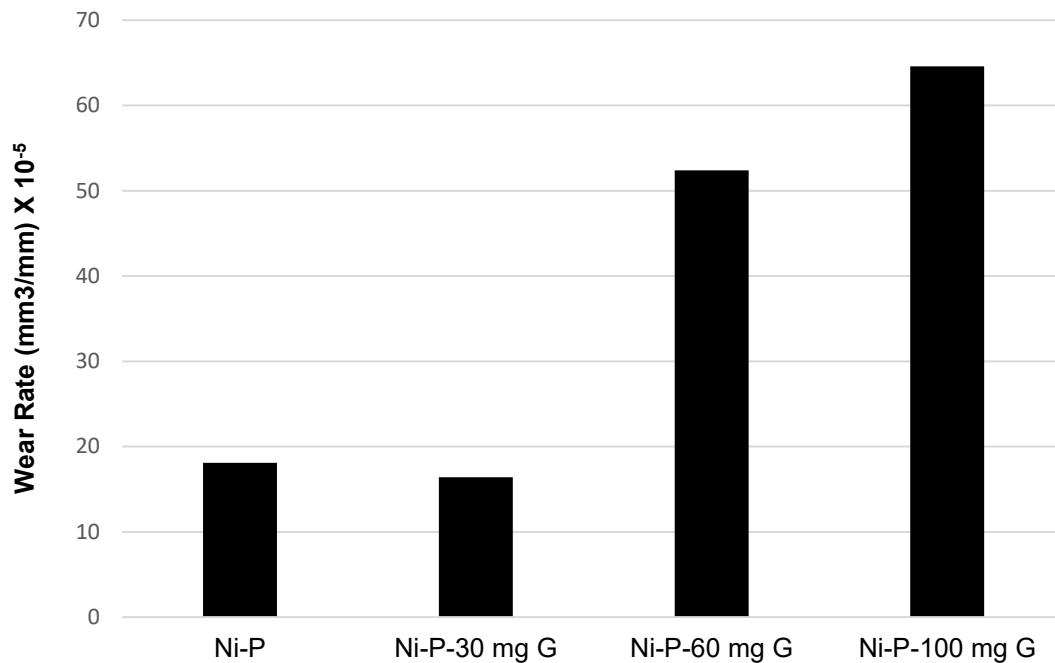
Figure 3.11 - Wear rate variation under constant load (39.2 N), multiple passes scratch test

3.6.3 Co-efficient of friction

COF for coatings prepared by graphene concentrations upto 100 mg/L and with similar thickness (~50 µm) were found to be in proximity i.e. within a range of 0.11-0.17 as shown in Figure 3.12. Here minor variation of COF with various graphene concentrations and the number of indenter passes can be attributed to various factors. These driving factors include (but not limited to) agglomerates formation, variation in plating thickness (though very minimal) due to change in graphene concentration, probability of indenter's encounter with graphene nano-platelets (or even minor agglomerates) at varying depths of coating matrix etc. It is worth noting that COF value for Ni-P-300mg G coating was found to be 0.19 that is relatively closer to COF value of substrate (0.26). This proximity between Ni-P-300mg G and un-coated substrate is attributed to lower thickness of Ni-P-300mg G; where the

indenter encountered underlying substrate during higher number of passes. The interaction of indenter with underlying substrate (underneath Ni-P-300mg G) in turn shifted COF value of Ni-P-300mg G closer to that for substrate.
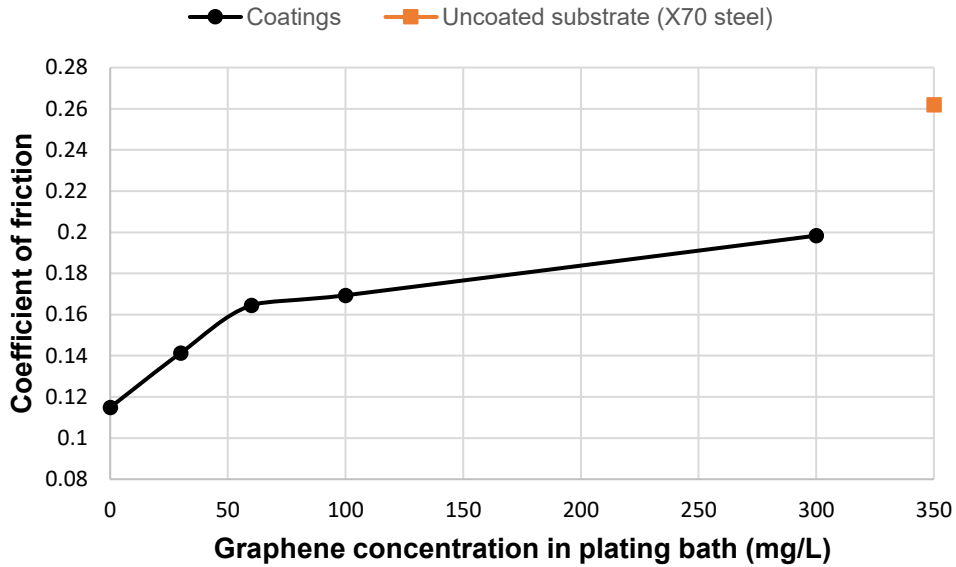
Figure 3.12 – COF variation with graphene concentration in plating bath

3.7 Indentation behavior

Figure 3.13 (a) shows load-displacement curves of all specimen under an indentation load of 2500 N. Whereas, load-displacement curve along with AE signal for Ni-P-30mg G is shown in Figure 3.13 (b). Initial/ first crack load was calculated by drawing vertical line (shown as red dotted line) from signal's peak towards curve, followed by locating the relevant point along the load axis (i.e. y-axis) shown as red circle. It's evident that Ni-P-30 mg G has the least displacement compared to rest of samples under similar indentation conditions. Highest displacement is associated with API X70 steel. Here, least displacement of Ni-P-30mg G is attributed to its higher hardness resulting from the highest graphene concentration in the matrix.

Figure 3.14 (a) and 3.14 (b) show the micrographs (mag. 50x) of indents produced by 1000 N load on Ni-P and Ni-P-30mg G, respectively. Unlike Ni-P (with radial cracks), Ni-P-30mg G shows considerable suppression in the indent's size as well as number and size of cracks. Here, this can be attributed to potential increase in the toughness of Ni-P-30mg G matrix due to the presence of graphene platelets. Finally, Figure 3.15 summarizes the initial crack loads for all coating samples from AE signals, as measured by methodology shown in Figure 3.13 (b). It is obvious that load required to initiate cracking (i.e. first crack load) is directly proportional to the amount of graphene in the coating matrix. So, the graphene has evidently caused toughening in Ni-P matrix as is discussed earlier in this research work. Whereas, the specific toughening mechanism is further discussed in later part of this research work.

On the other hand, Ni-P-300mg G didn't show any signs of major cracks. Simultaneous analyses of indent's surface, load-displacement curves along with AE signals reveal that the behavior of Ni-P-300mg G is due to the ductile effect of underlying substrate rather coating's toughness; that results in coating pile-up and minor radial cracks instead of Hertzian cracks. The trend of toughness variation of coatings (especially Ni-P-30mg G) is almost consistent to what is observed earlier during scratch testing process. Micrographs for the indent's surface and cross-sections are detailed in Figure A7 and A8, whereas load-displacement curves for all specimen can be referred in Figure A9 of Appendix section.
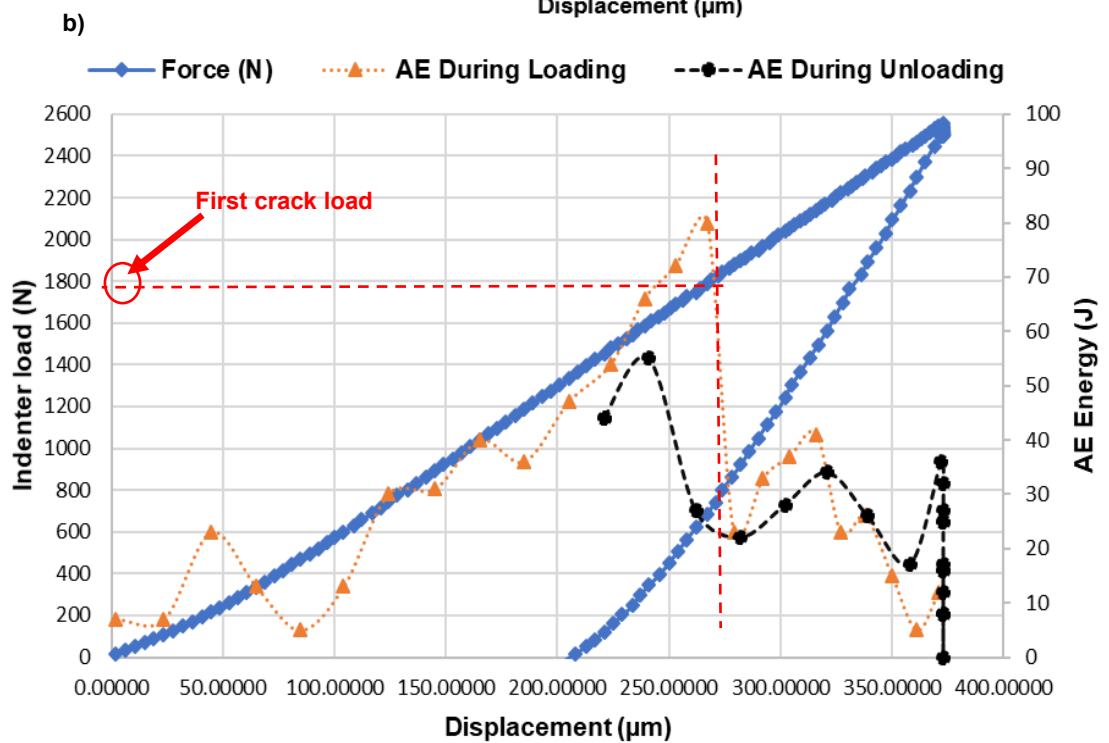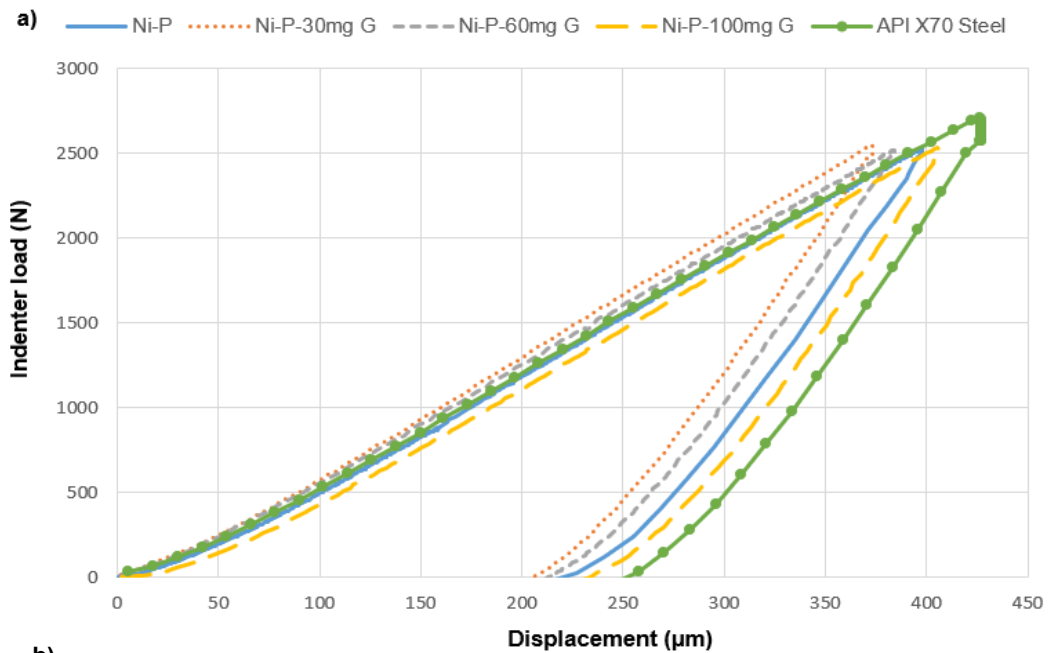
Figure 3.13 - Load-displacement curve under 2500 N for a) all specimens b) Ni-P-30mg G coating along with AE signals
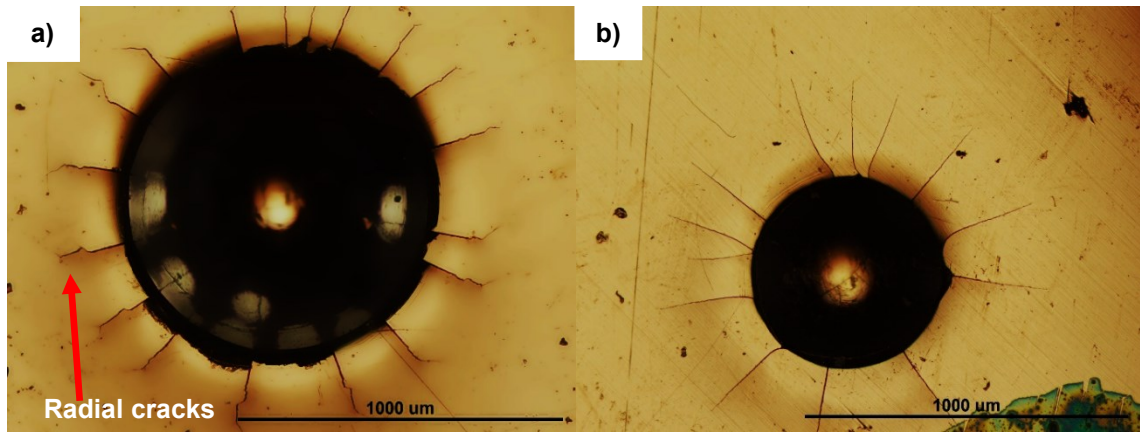
Figure 3.14 - Optical micrograph (mag. 50x) for surface of indent on a) Ni-P b) Ni-P-30mg G under 1000 N load
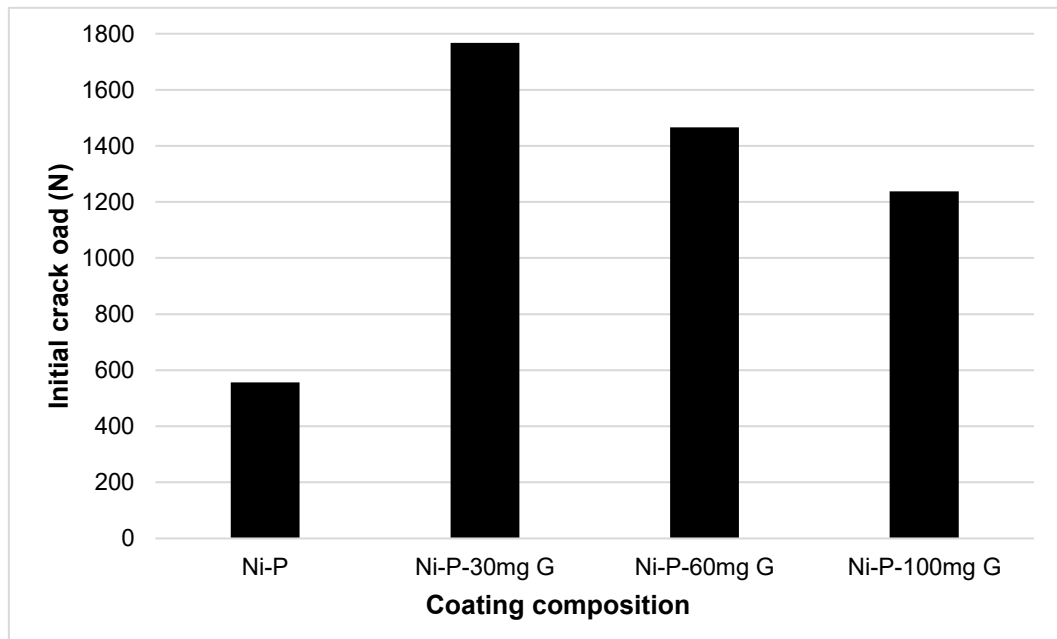

Figure 3.15 - Initial crack load of coatings under 1000 N indentation load

3.8 Corrosion behaviors

Potentiodynamic polarization curves and calculated corrosion rates from Equation (2.10) are shown in Figure 3.16 (a) and 3.16 (b), respectively. Table 3-1 summarizes the measured values of corrosion potential, E_{corr} as well as calculated corrosion current densities, i_{corr} using Equation (2.9). It's evident that graphene enhancement in the matrix has shifted the corrosion potential towards the positive along with reduced current density. Analysis of PD polarization curves in Figure 3.16 (a) reveals that graphene incorporation in Ni-P matrix has improved the corrosion behaviors by shifting the potential towards positive side with concurrent reduction in the corrosion current density.

As calculated from Equation (2.11), there is around 39.78 %, 48.44 % and 38.77 % increase in the corrosion resistance as graphene is added in the concentrations of 30 mg/L, 60 mg/L and 100 mg/L, respectively as shown in Figure 3.16 (b). The improved corrosion behaviors of ternary coatings are the results of graphene's proven barrier properties as well as impermeability that resist the electrolyte from seeping into the coating matrix [9-10]. Surfaces of sp^2 hybridized carbon allotropes (i.e. graphene) form natural diffusion barriers providing a physical separation between the coating and underlying substrate [89]. Whereas, impermeability of graphene membrane (or platelet) is a function of inherent barrier property of graphene as well as quality level (edge defects, basal plane defects etc.) of the membrane [9]. Unlike other additives for ternary coating systems, graphene is an excellent conductor of electricity. The performance of graphene for combating corrosion is sensitive to surrounding underlying matrix/ substrate as reported by Kirkland [90]. Also, corrosion resistance of Ni-P-G can vary due to certain other factors such as likely agglomeration effects, defects in platelets and the orientation of platelets in the matrix etc. The higher electrical conductivity and larger aspect ratio of graphene platelets divert the

path of electrons thereby impeding their flow towards cathodic regimes (i.e. Ni-P matrix and underlying steel substrate) [16, 90].

Table 3-1 Corrosion attributes of samples

Sample	*Ecorr* (Volts) vs SCE	*icorr* (A/cm^2)
AISI 1018	-0.52	1.27 x 10^{-5}
Ni-P	-0.42	6.25 x 10^{-7}
Ni-P-30mg G	-0.388	5.19 x 10^{-7}
Ni-P-60mg G	-0.393	5.07 x 10^{-7}
Ni-P-100mg G	-0.369	5.11 x 10^{-7}

(b)
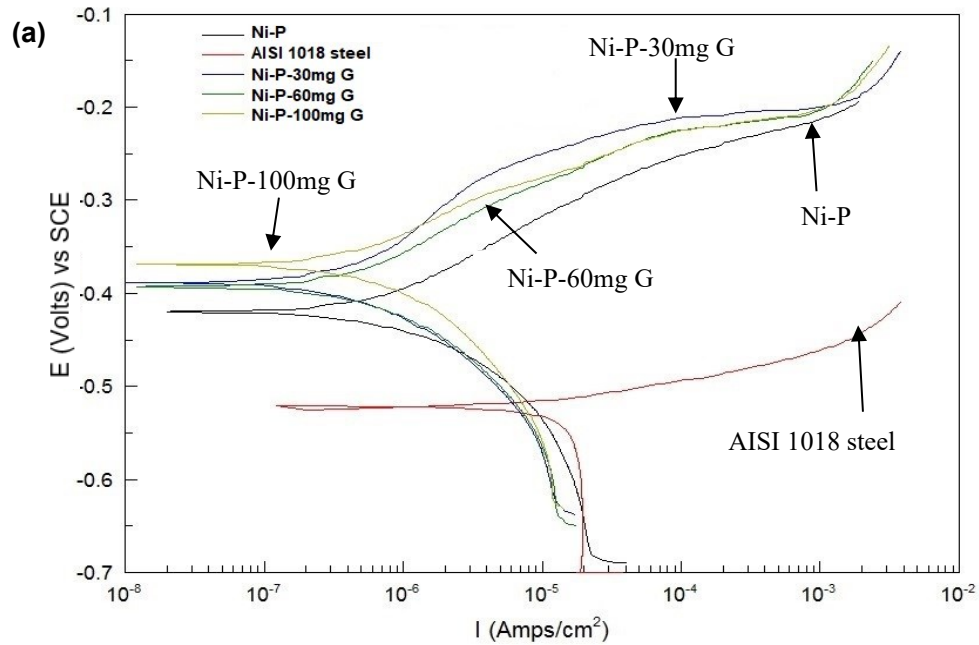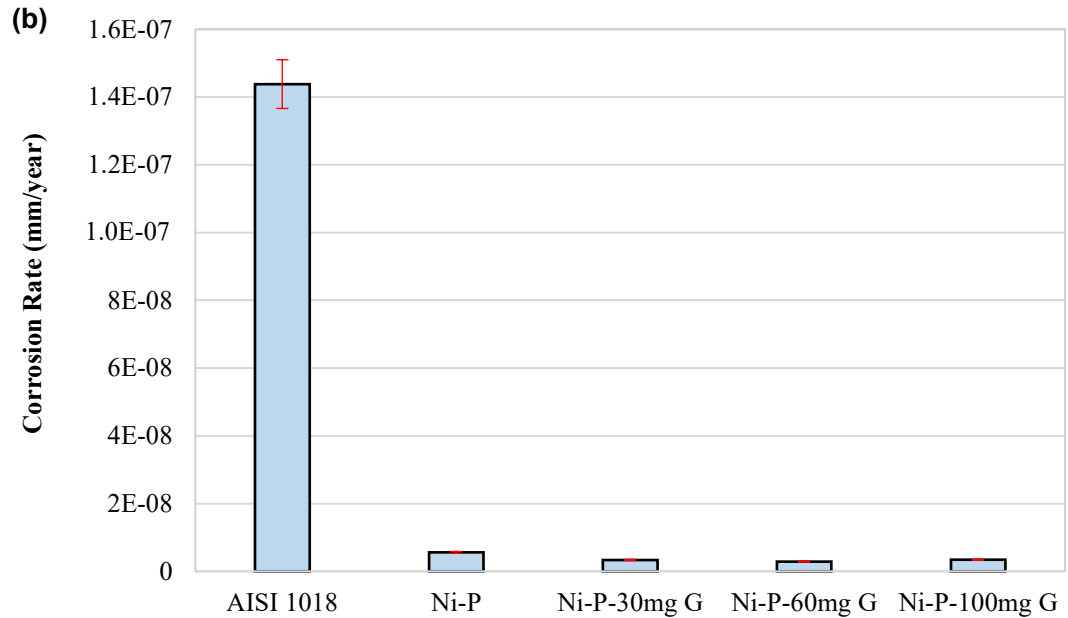
Figure 3.16 - (a) Potentiodynamic polarization curve (-0.25 V below OCP and 0.25 above OCP) and (b) calculated corrosion rates

3.9 Erosion-corrosion and erosion behaviors

Material loss rate due to erosion-corrosion for all coatings and reference material (AISI 1018) are shown in Figure 3.17 (a), where K_{ec} is the total material loss rate due to erosion-corrosion, K_{eo} is the material loss rate due to pure erosion, K_{co} is the material loss rate due to pure corrosion and Ks represents the material loss due to synergy. It is evident from Figure 3.17 (a) that Ni-P-100mg G has the lowest material loss rate due to pure erosion (K_{eo}) and erosion-corrosion (K_{ec}) among all coating compositions and substrate (AISI 1018). Ni-P-100mg G exhibits 1.5 times and 5 times erosion-corrosion and pure erosion resistance respectively, compared to Ni-P coating. This is mainly because incorporation of graphene provides higher coating hardness, reduced the inter-connected surface porosities and improved surface smoothness. Pure erosion resistance increases with increase in hardness. On the other hand, removal of surface porosity increases the corrosion resistance

80

and reduces the synergistic contribution. It is important to note that, pure erosion rate (K_{eo}) is the key driving mechanism towards overall erosion-corrosion loss rate (K_{ec}) after synergism (K_s), whereas pure corrosion (K_{co}) contribution is relatively small (especially for graphene enhanced coatings). This behavior, where pure erosion (K_{eo}) and synergism (K_s) are the main contributor towards total material loss, is consistent with earlier studies [16, 91-92].

Surface roughness has been reported to play an important role in changing the erosion rates, as the surface irregularities can change the angle of attack of incoming erodent particle. Smoother surface is likely to erode at reduced rate due to change in angle of impact as reported by Kirols [93]. Although, both Ni-P-30mg G and Ni-P-100mg G have increased hardness (than Ni-P) but the relatively smoother surface in Ni-P-100mg G is improving its overall erosion performance even compared to Ni-P-30mg G. Here, Ni-P-100mg G has the highest surface smoothness compared to rest of samples, it's less likely to deflect erodent particles. Higher surface smoothness reduces the erosion loss rate (K_{eo}) that in turn reduces the erosion-corrosion loss rate (K_{ec}) for Ni-P-100mg G coating. Higher pure erosion loss rate (K_{eo}) and erosion-corrosion loss rate (K_{ec}) of Ni-P coating is mainly due to its higher surface roughness and non-uniformity of the coating microstructure (i.e. pores, defects etc.). Figure 48 (b) illustrates the contribution of erosion enhanced corrosion *(ΔKc)* and corrosion enhanced erosion *(ΔK$_e$)* to the total synergy *(Ks)*. Corrosion enhanced erosion (ΔK$_e$) is dominant for all coating samples, whereas erosion enhanced corrosion (ΔK$_c$) dominates the synergistic effect for AISI 1018. This is mainly because for all coatings, deposition of corrosion product inside the pores and micro-cracks accelerates the coating material removal process by abrasive particle impact. On the other hand, for AISI 1018 steel, the abrasive particle impact increases surface roughness and creates more surface area for corrosion [94]. In addition, a thin work-hardened layer is formed on the surface which is

more anodic in nature and undergoes accelerated corrosion due to localized galvanic effects [1,95].

Figure 3.17 (c) displays the contribution of synergy to total material loss rate. It's worth noting that synergy has significant contribution (> 50%) towards overall material loss rate, for all coatings as well as substrate steel. During erosion-corrosion, material loss rate increases due to simultaneous action of erosion (caused by the abrasive particles) and corrosion. Contribution of synergism (K_s) towards total material loss rate (K_{ec}) is more prominent in coatings incorporated with graphene. For Ni-P-100mg G, synergy contributes around 84% to total material loss rate. This behavior is similar to what is reported earlier in literature [16], where synergism contribution towards overall material loss rate for a coating produced by 100 mg/L graphene is more than those produced by graphene concentrations of 25 mg/L, 50 mg/L and 75 mg/L.
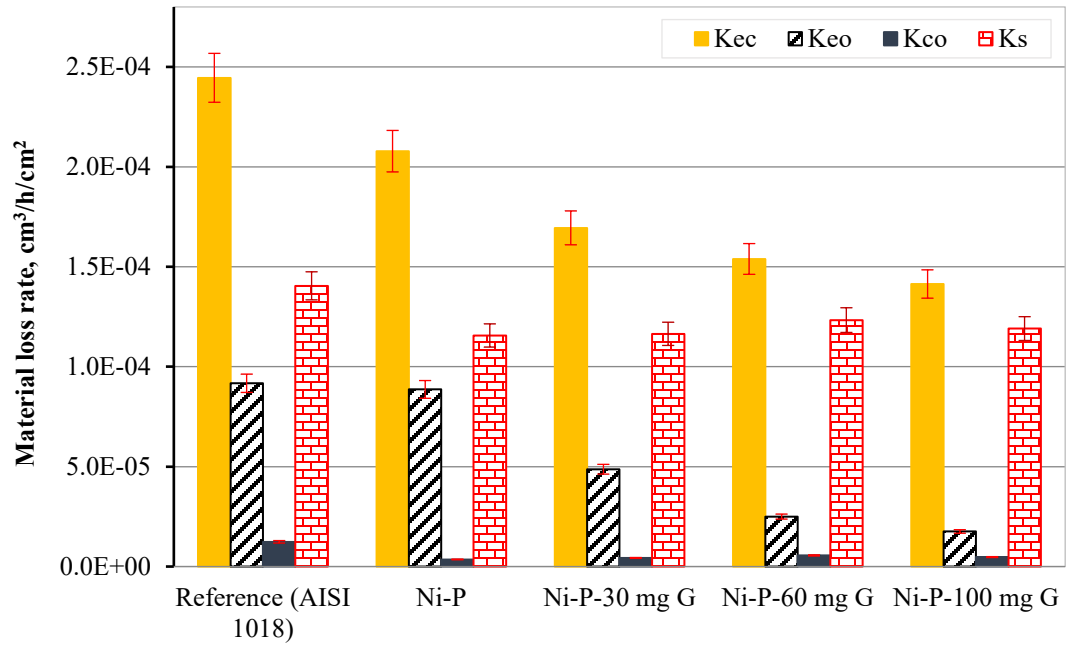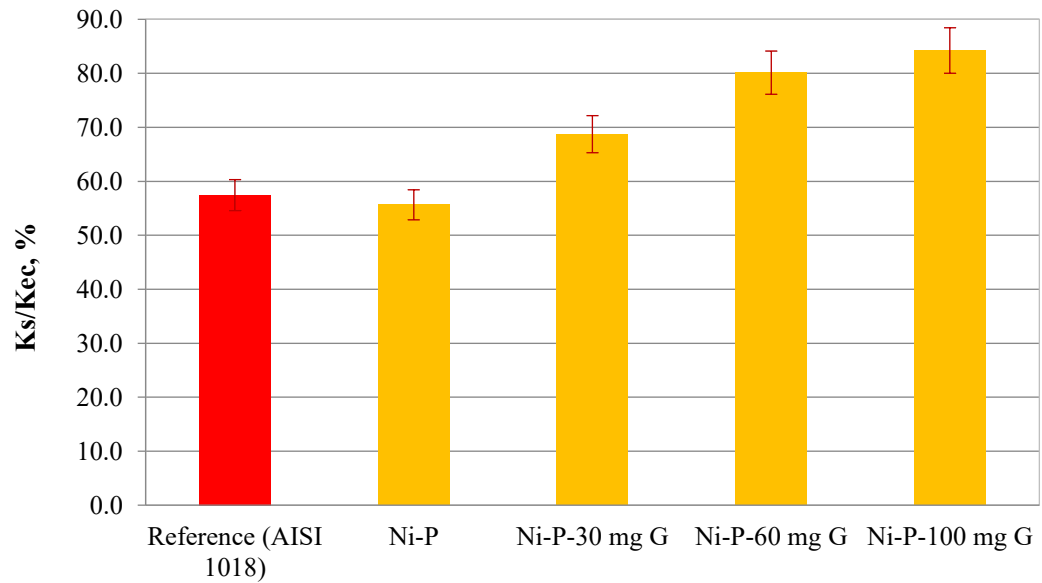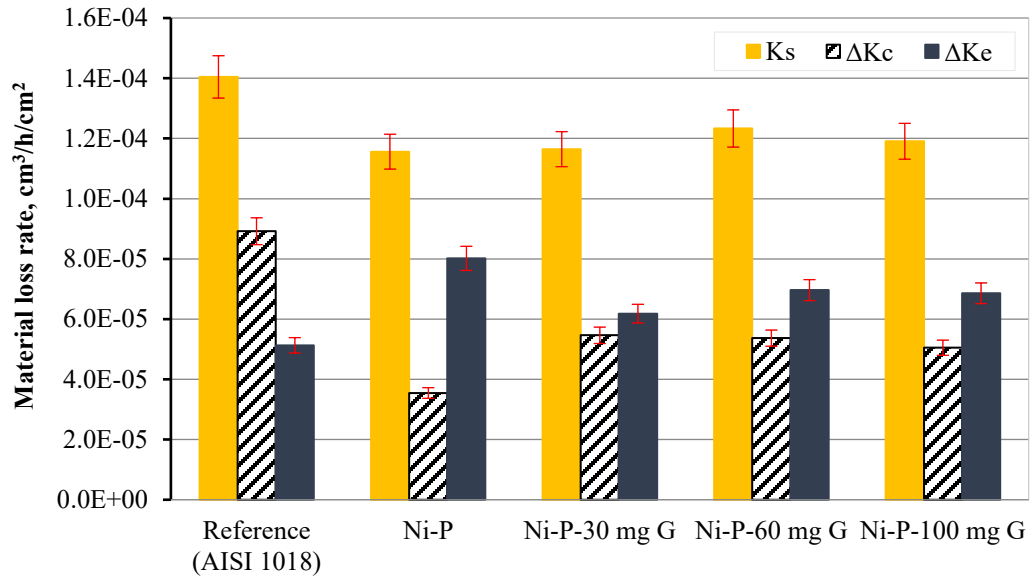
Figure 3.17 - Erosion-corrosion synergy analysis for the coatings, (a) material loss rate due to erosion-corrosion, pure erosion, pure corrosion and synergy, (b) contribution of erosion enhanced corrosion *(ΔKc)* and corrosion enhanced erosion *(ΔKe)* to total synergy *(Ks)* and (c) contribution of synergy to total material loss rate

Figure 3.18 (a) and 3.18 (b) show the optical micrograph of 1018 steel surface after pure erosion and erosion-corrosion, respectively. During pure erosion, AISI 1018 steel surface undergoes plastic deformation, indentation and metal-cutting by the abrasive particles. During erosion-corrosion, 1018 undergoes severe degradation due to formation of inter-connected pits through selective leaching and galvanic corrosion [1].

Examination of SEM micrographs of eroded-corroded surfaces of Ni-P coating in Figure 49 (c-d) reveals various failure modes such as micro-fracture, micro-cutting and plastic deformation etc. [96-97]. Micro-cutting (known to initiate by chip formation) is mainly due to lower hardness and rough features [96]. Whereas, micro-fracture of Ni-P coating is due to its lower fracture toughness as revealed in the earlier sections of this research work. Furthermore, Ni-P coating also exhibits some pitting as shown in Figure 3.18 (e). Unlike Ni-P, Ni-P-100mg G coating doesn't show any signs of corrosion or micro-fracture as shown in Figure 3.19 (a-d). The absence of corrosion in Ni-P-100mg G is mainly due to its higher corrosion resistance from graphene platelets as discussed earlier in section 3.8 of this study. On the other hand, higher toughness of Ni-P-100mg G coating (due to toughening mechanisms of crack shielding and crack deflection) has impeded the failure due to micro-fracture [55]. In addition to operating conditions, asperities of erodent particles (either intrinsic or from particle's fracture) and surface attributes govern the mechanism of erosive wear [96]. Here, micro-cutting was found more dominant in Ni-P coating than Ni-P-100mg G; and can be attributed to its simultaneous lower hardness and higher roughness [97].

Material removal pattern from the coating surface shows the dependency on surface roughness as any irregularities (due to roughness) change the angle of attack inclining the material's removal trend towards particle dis-bonding [95-96]. In addition, abrasive particle impact(s) create more available area (for corrosion) on coating's surface resulting from particle dis-bonding, micro-cutting and micro-ploughing etc. When compared with other

ternary coatings, Ni-P-100mg G undergoes more plastic deformation than micro-fracture compared to Ni-P-30mg G and Ni-P-60mg G coatings due to its relatively lower hardness [55]. Despite of higher hardness and higher fracture toughness, Ni-P-30mg G is subjected to more wear damage and higher overall material loss rate (K_{ec}) due to particle dis-bonding from abrasive particles impact compared with other ternary coatings. This higher loss rate in Ni-P-30mg G is merely due to its higher surface roughness. Although, both as-deposited Ni-P-30mg G and Ni-P-100mg G have increased hardness (than Ni-P) but the relatively smoother surface in as-deposited Ni-P-100mg G is improving its overall erosion performance even compared to Ni-P-30mg G.
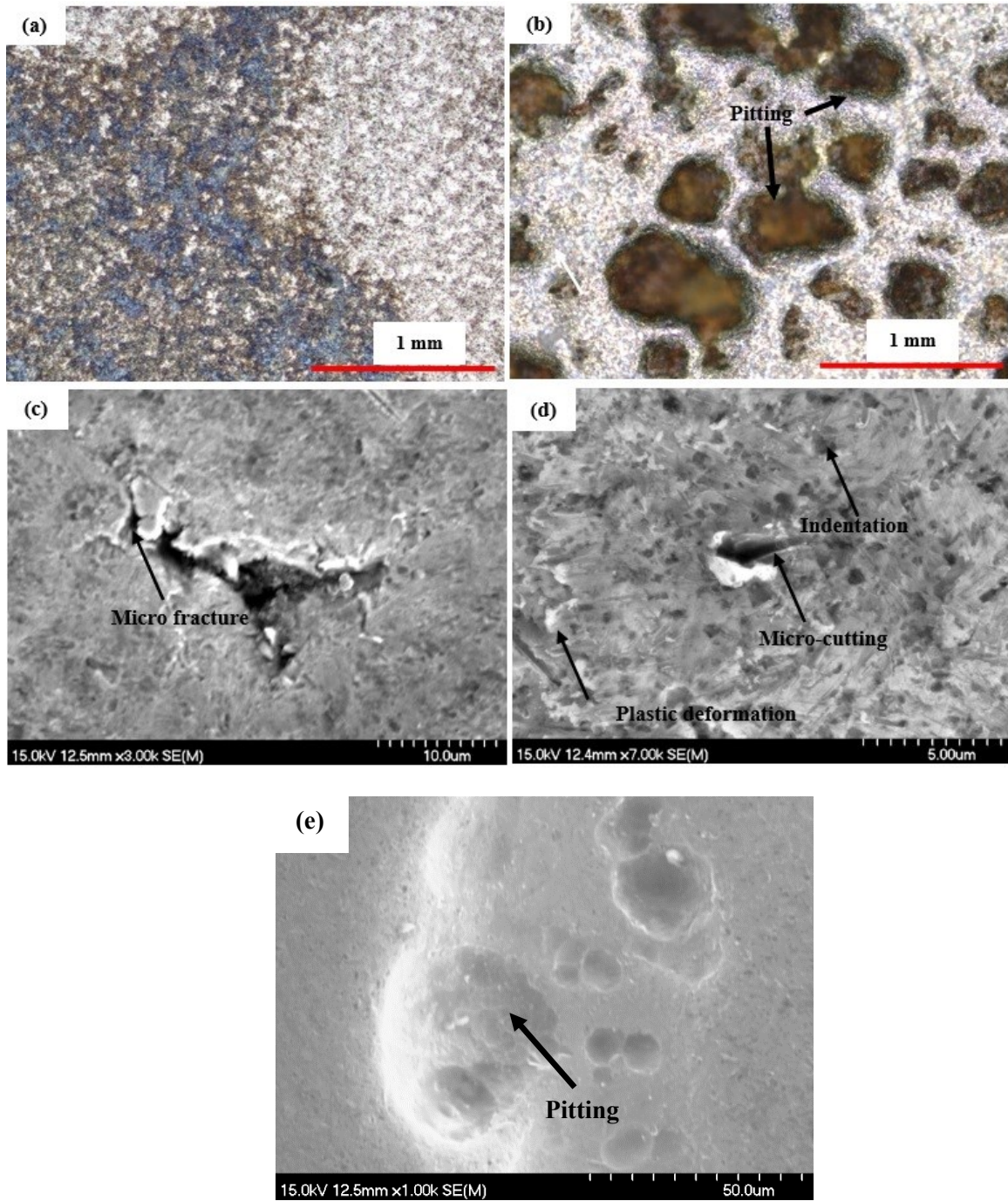
Figure 3.18 - Optical micrograph (mag. 200x) for 1018 after (a) pure erosion (b) erosion-corrosion and (c-e) SEM micrograph for Ni-P coating after erosion-corrosion
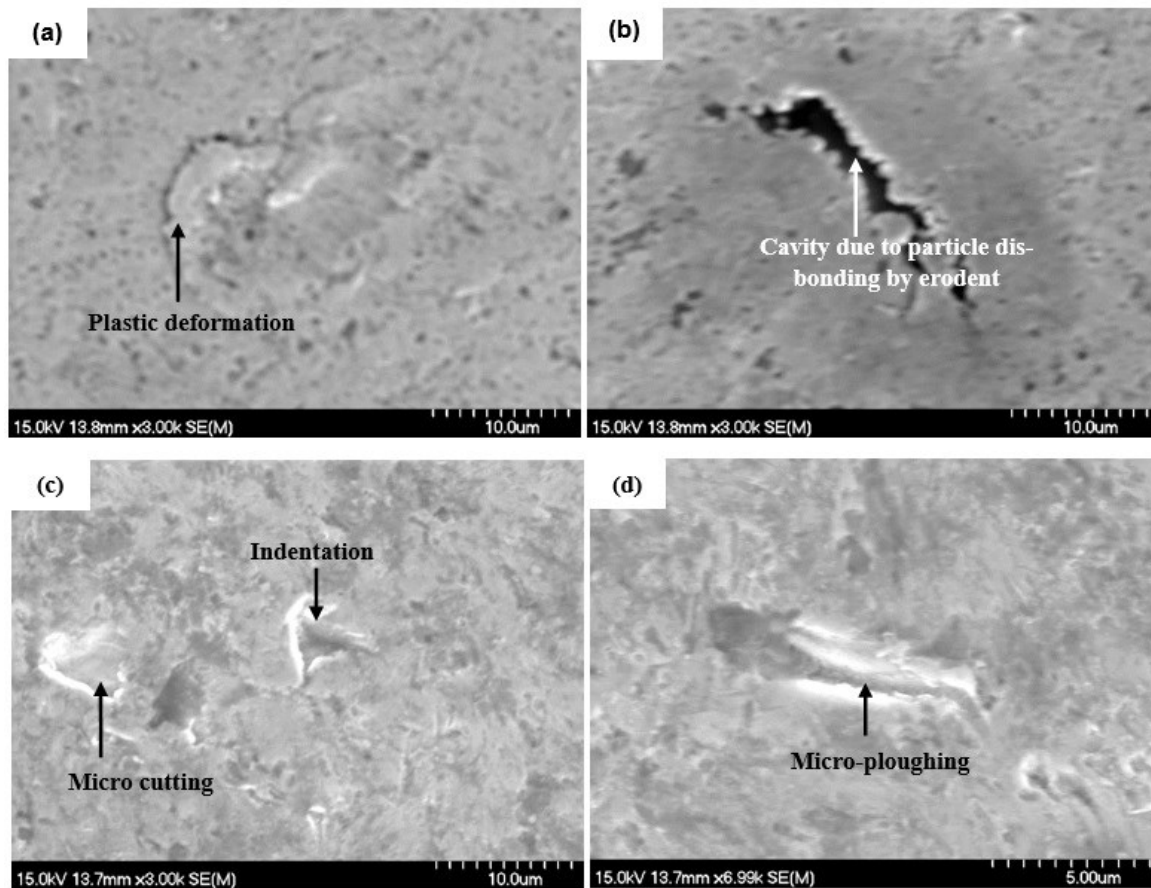
Figure 3.19 - (a-d) SEM micrograph for Ni-P-100mg G coating after erosion-corrosion
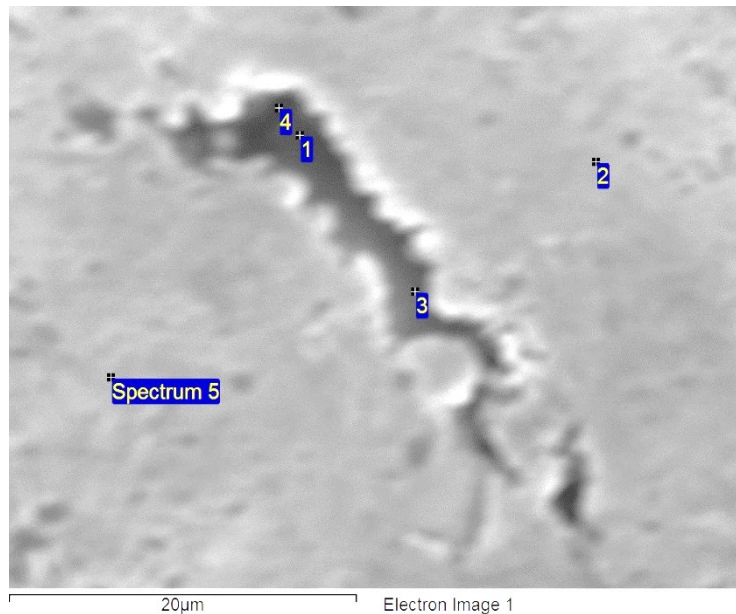
Figure 3.20 - SEM micrograph of Ni-P-100mg G after erosion-corrosion

Table 3-2 shows EDS results of cavity on Ni-P-100mg G surface in Figure 3.20. Here, the absence of any considerable Fe peaks eradicates the possibility of surface cracks due to erodent particle's impact. Figure 3.21 shows schematic of typical wear mechanisms w.r.t angle of attack of erodent particle.

Table 3-2 Post SPEC EDS spectrum at surface of Ni-P-100mg G

Spectrum Point	C (wt. %)	O (wt. %)	Si (wt. %)	P (wt. %)	Ni (wt. %)	Fe (wt. %)
1	6.52	2.64	1.20	0.22	89.04	0.37
2	4.81	1.29	0.33	2.17	91.29	0.10
3	26.13	13.87	2.55	2.06	55.13	0.26
4	9.08	2.18	0.6	0.4	88.14	0
5	5.03	1.92	0.50	9.00	83.55	0
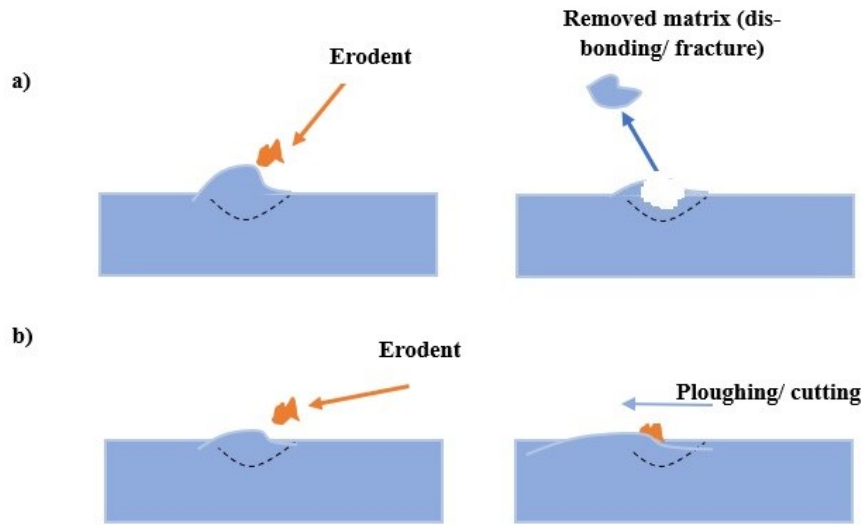
Figure 3.21- Schematic of possible wear damages w.r.t angle of attack

Figure 3.22 (a-e) shows the optical micrograph of craters by WC particles on the coatings and uncoated substrate (AISI 1018 steel). At high particle speeds (corresponding 60 psi pressure), Ni-P-30mg G showed least plastic deformation (i.e. small indent size) and attributed to the higher hardness of Ni-P-30mg G compared to rest of coating compositions and substrate. Also, it's noticeable that at lower speed (corresponding 30 psi pressure) & 45º angle of attack, the effect of hardness of Ni-P-30mg G is not that pronounced. Whereas, Ni-P shows least indent size due to its second highest hardness after Ni-P-30mg G and the possibility that particle didn't interact compressively with defect site [55]. On the other hand, substrate steel 1018 showed pile up and plastic deformation without any signs of cracks. Figure 54 shows the trend of indent size for various compositions and particle speeds.
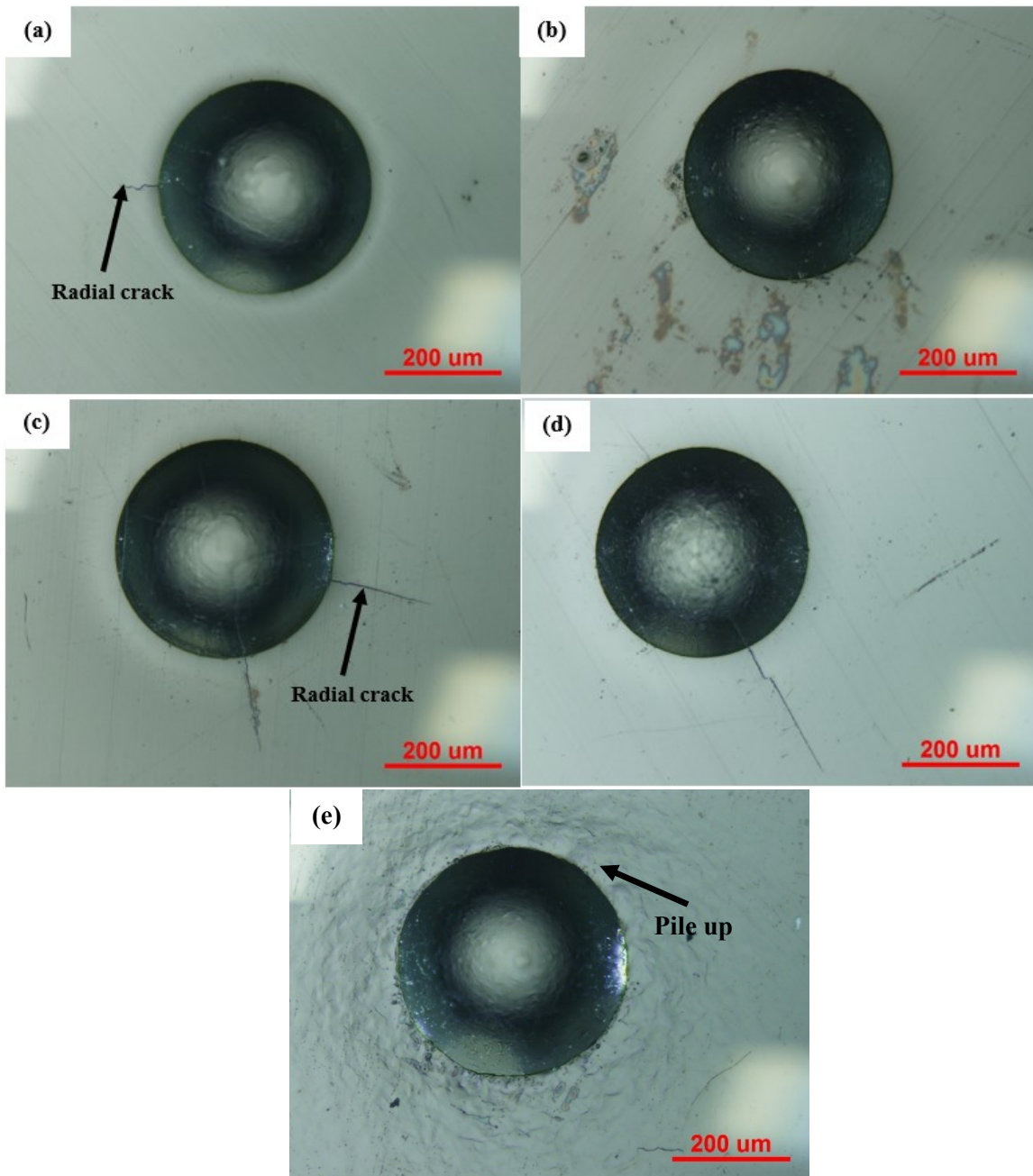
Figure 3.22 - Optical micrograph (mag. 100x) after erosion with WC particle at velocity of 52 ms^{-1} and angle of attack 90 for (a) Ni-P (b) Ni-P-30mg G (c) Ni-P-60mg G (d) Ni-P-100mg G (e) AISI 1018 steel
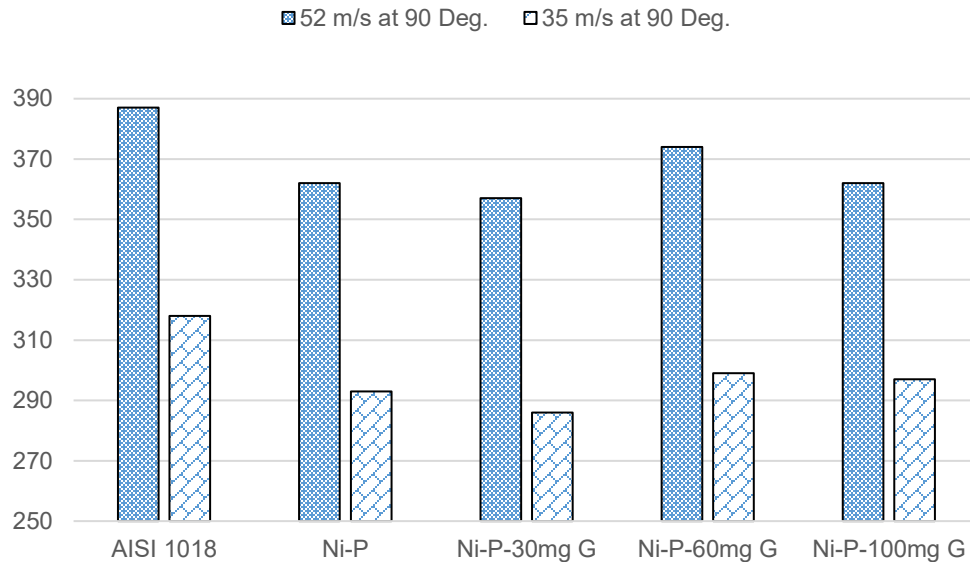
Figure 3.23 - Indent diameter on various samples produced by WC particle under 90-degree angle of attack

3.10 Toughening mechanisms

Analyses of surfaces subjected to scratching and Hertzian-type indents revealed some commonalities in the cracking behavior of coatings, where Ni-P-30mg G exhibits improved toughness than Ni-P coating as shown earlier in Figure 3.9 (a-b). On the other hand, toughening is also evident in Ni-P-30mg G under the Hertzian-type indentation loads where ~ 50 μm thick Ni-P-30mg G coating showed least cracks and highest load to initiate major cracks than other coatings of similar thickness.

SEM and EDS examinations were conducted on Ni-P-30mg G coating in order to identify toughening mechanisms. Such analyses of Hertzian-type cracks in Ni-P-30mg G scratch track revealed crack suppression along with absence of any Fe peaks. The absence of Fe peaks further confirms that indenter's load is supported by the coating. Unlike Ni-P-300mg G coating, substrate hasn't been encountered with indenter during the scratch process. Therefore, suppression of cracks supports the presence of higher toughness in Ni-P-30mg

G due to presence of graphene nano-platelets. Two types of toughening mechanisms named as crack shielding and crack deflection have been identified and are given below. SEM micrographs revealing cracked portion of the scratch track along with EDS data points for Ni-P-30mg G coating are shown in Figure 3.24 (a-b). In Figure 3.24 (a), the cracks originate from the left side and seem to terminate at the point indicated by circles.
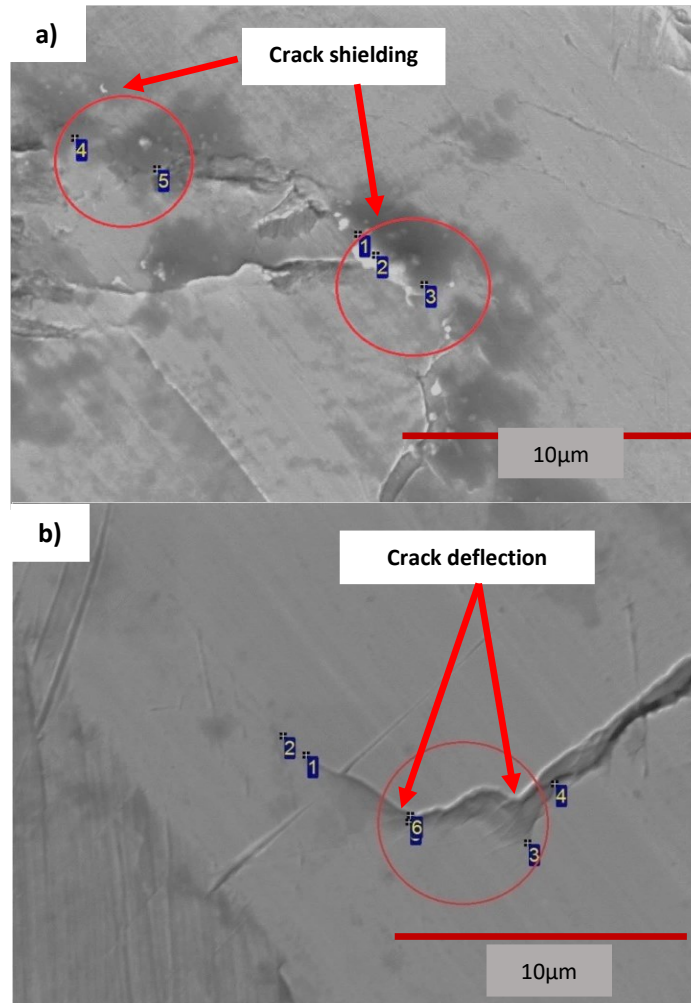
Figure 3.24 - SEM micrograph of a) shielded cracks b) deflected cracks alongwith EDS data points in Ni-P-30mg G coating

Point EDS data for the spots labeled in Figure 3.24 (a) is given in Table 3-3. It is evident that there is a high vol. % concentration of graphene at the crack termination point. Graphene seems to resist and absorb the energy of crack propagation thereby impeding the growth of cracks. In such a scenario, the shielding graphene nano-platelets are likely to cause dissipation of crack driving energy; thereby impeding the cracks propagation [70].

Table 3-3 EDS data for points spectrum at crack shielding locations in Ni-P-30mg G

Spectrum Point	C (vol. %)	P (vol. %)	Ni (vol. %)
1	40.87	15.53	43.61
2	36.62	15.38	47.99
3	41.72	15.16	43.19
4	39.19	15.29	45.52
5	39.39	15.27	45.33

Crack deflection that has been reported to improve the fracture toughness of composites upto three times [72]. Crack deflection involves change in the direction of crack as it encounters a particle, causing the loss of driving energy. This eventually leads to localized suppression of cracks [71]. Figure 3.24 (b) shows the deflection in pathway of crack that is likely caused by graphene nano-platelets as well as EDS data points on micrograph to investigate chemical composition at the locations of crack deflection. Table 3-4 shows EDS data of labeled points # 5 & 6 in Figure 3.24 (b) revealing a higher vol. % of graphene. The presence of graphene and the deflection of cracks at labeled points support the occurrence of crack deflection phenomena due to graphene nano-platelets.

Table 3-4 EDS data for points spectrum at crack deflection locations in Ni-P-30mg G

Spectrum	C (vol. %)	P (vol. %)	Ni (vol. %)
1	17.95	19.26	62.74
2	36.39	14.39	49.22
3	38.24	13.75	47.99
4	60.03	8.55	31.41
5	45.46	16.33	37.85
6	37.30	14.84	47.86

Chapter 4 Conclusions

Ni-P and graphene enhanced Ni-P coatings were prepared using electroless plating that were characterized for topography (surface features), Vickers hardness, deposition rates along with microstructural analysis. The coatings were further characterized for tribological and electrochemical attributes using single point scratch testing, Hertzian indentation, solid particle erosion, potentiodynamic polarization and slurry pot erosion-corrosion testing, respectively. Following conclusions can be reached from current study:

1. Graphene enrichment in Ni-P matrix significantly increased the corrosion resistance by increasing the polarization potential and reducing the corrosion current density

2. As plated Ni-P-100mg G coating containing 15 vol. % graphene achieved highest surface smoothness, highest erosion resistance as well as least erosion-corrosion loss

3. Dominant wear mechanisms during erosion and erosion-corrosion in all coatings were micro-ploughing, micro-cutting and plastic deformations

4. Synergistic effect (K_s) was the dominant contributor (> 50%) towards overall erosion-corrosion loss (K_{ec}), while pure corrosion (K_{co}) contribution was the least

5. The presence of graphene in a concentration of 30 mg/L in plating bath achieved highest concentration (18 Vol. %) of graphene in the coating matrix thereby increasing the hardness and wear resistance

6. Also, similar concentration i.e. 30 mg/L improved toughness of Ni-P coating matrix by crack shielding and crack deflection phenomena

7. A higher concentration of 300 mg/L of graphene in the plating bath had diminishing return as it concurrently reduced the deposition rate, matrix hardness and surface smoothness

8. Tribological attributes (wear rate, COF, cracking etc.) of Ni-P-300mg G coating were in proximity to that of uncoated substrate steel due to its lower thickness

9. Surface roughness (Sa) was found to increase with increase in plating time and stirring speed

10. Higher stirring speed in graphene added plating bath led to gouging/ erosion marks on the coating surface due to collisions from graphene platelets that have higher hardness than Ni and P

11. With same surface smoothness (polished), Ni-P-30mg G showed improved resistance to solid particle erosion and subsequent cracking

Further works that can be conducted may include (but not limited to) below:

1. Development of free-standing graphene enriched Ni-P coatings

2. Nano-indentation and bending tests on Ni-P-G coatings

3. Annealing and phase analysis of Ni-P-graphene using XRD (x-ray diffraction) studies to understand the process zones (i.e. stress areas)

4. Tribological and electrochemical behavior of annealed Ni-P-graphene coatings

5. Characterization of graphene in coating matrix using Raman and TEM (transmission electron microscopy) to account for defects and degradations during deposition process

6. Polish both samples at same level prior to erosion-corrosion to eliminate the impact of surface roughness from the coating's hardness/ toughness

Appendix A – Publications

Published papers generated from current research work include:

1. Rana, Ahmad Raza Khan, et al. "Preparation & Tribological Characterization of Graphene Incorporated Electroless Ni-P Composite Coating." Surface & Coatings Technology 369 (2019), pp. 334-346

2. Rana, Ahmad Raza Khan, et al. "Effect of GNPs (graphene nano-platelets) addition on Erosion-Corrosion Resistance of Electroless Ni-P Coatings." Journal of Bio & Tribo-Corrosion 6:11 (2020), pp. 1-14

3. Preparation & Tribological Characterization of Graphene Enriched Ni-P Coatings on X70 Pipeline Steel, CORROSION 2020 Houston (TX) NACE International (Mar 2020)

Additional published/ accepted work related to materials, corrosion and asset integrity include below:

4. Neighborhood Watch – A Right Step Towards Asset Integrity, CORROSION 2020 Houston (TX) NACE International (Mar 2020)

5. Rana, Ahmad Raza Khan, et al. "Case Study on Ti Lining Failure" International Journal of Material Science and Engineering

6. Rana, Ahmad Raza Khan, et al. "Mitigating Material Damages Through Risk-Based Inspections." Material Performance Magazine Vol. 57 No.9 (2018), pp. 46-49

7. Rana, Ahmad Raza Khan, et al. "Neighborhood – An Influential Factor for Materials Damages." Material Performance Magazine Vol. 58 No.6 (2018), pp. 52-55

8. Rana, Ahmad Raza Khan, et al. "Case Study on Failure of Hexane Storage Tank." Corrosion Management Journal 150 (2019), pp. 20-22

9. Rana, Ahmad Raza Khan, et al. "Thermal Fatigues – A Quest for asset Integrity." Inspectioneering Journal

Posters and presentation work include below:

10. Influence of graphene enrichment on erosion-corrosion and cracking behaviors of electroless Ni-P composite coatings, CORROSION 2020 Houston (TX) NACE International (Mar 2020)

11. Qualitative RBI – An Effective Corrosion Combating Tool, NACE northern Area Western Conference Calgary (AB) NACE International (Feb 2019)

12. Qualitative RBI for Heat Exchangers Damages Mitigation, NACE Northern Area Eastern Conference Halifax (NS), NACE International (Jan 2019)

13. Qualitative RBI – A Dandy Start for Materials Damages Mitigation, NACE Northern Area Eastern Conference Halifax (NS), NACE International (Oct 2018)

Appendix B – Additional tables

Table B1 Reported mechanical/ metallurgical cracking for oil and gas applications [1]*

CRACKING TYPE	DESCRIPTION
Dissimilar metal weld cracking	Cracking of ferritic-austenitic welds under exposure to high temperature(s)
Brittle fracture	Brittle cracking of all materials (especially thick components under stresses, high pressure, low operating temperatures)
Reheat cracking	Cracking of thick section of low alloy steels e.g. P91 (9Cr-Mo-V), SS 3xx and Ni base alloys e.g. Alloy 800H under high temperature (750 ºC)
Temper embrittlement	Loss of toughness in high strength low alloy steels due to long term exposure to 343 ºC – 577 ºC
Sigma-phase embrittlement	Cracking of SS 4xx, SS 3xx, duplex SS HK and HP alloys due to high (10–40 %) ferrite content after a long-term exposure to 538 ºC – 927 ºC
475ºC embrittlement	Cracking of SS 4xx and duplex SS due to ferrite content after a long-term exposure to 316 ºC – 540 ºC
Creep and stress rupture	All metals and alloys suffer deformation due to high temperature and loads leading to cracking e.g. heater tube hangers etc.
Short term overheating rupture	Fracture of materials via bulging (all compositions) due to high temperature exposure in fired heaters

Table B2 Reported environmental driven cracking in oil and gas applications [1] *

CRACKING TYPE	BRIEF DESCRIPTION
Chloride stress corrosion cracking	Cracking of SS 3xx in high chlorides environments (Marine, cooling towers etc.)
Caustic stress corrosion cracking	Cracking of Carbon steel, low alloy steel and SS 3xx exposed to caustic service especially at non-PWHT welds
Ammonia stress corrosion cracking	Cracking in Cu alloys and Carbon steels under combined action of stresses as well as ammonia (or NH_3 compounds)
Ethanol stress corrosion cracking	Surface-initiated cracks on carbon steels under the combined action of stress and fuel-grade ethanol
Sulfate stress corrosion cracking	Cracking of Cu in the sulfate solutions under the combined action of aging and residual stresses
HCl SCC of Ni [98]	Cracking of Ni (and its alloys) under the combined action of stresses and exposure to high temperature aqueous-chloride environments
Polythionic acid stress corrosion cracking	Sensitized microstructure of stainless steel (SS316, 317, 321, 347) causes surface cracks in the events of stresses and exposure of sulfide scale to Oxygen and H_2O
Amine stress corrosion cracking	Cracking of Carbon steel and low alloy steels in amine service with severity depending on amine concentration, temperature and residual stresses
Hydrogen Induced cracking	Stepwise cracking in the laminates of carbon steel and low alloy steel from H_2S permeation in the laminates
Hydrogen Stress cracking - HF	Cracking of high hardness (> 237 BHN) zones in carbon and low alloy steel due to exposure to HF acid environments
Carbonate stress corrosion cracking	Cracking of carbon and low alloys steels as a result of exposure to free water phase in carbonate (with some H_2S) under the action of residual stresses
Liquid metal embrittlement	Surface initiated cracking on metals as a result of exposure to molten metals (e.g. molten Zn causes cracking of SS, Hg can crack Alloy 400 as well as Cu and Al alloys; and high strength steels are damaged by Cd and Pb)
Hydrogen embrittlement	Loss in toughness of carbon steel, SS 4xx and Ni-based alloys due to penetration of atomic hydrogen from aqueous, corrosive or gaseous environment

Table B3 Reported medium/ low temp. corrosion(s) for oil and gas applications [1]*

TYPE OF CORROSION	BRIEF DESCRIPTION
Corrosion under insulation	Corrosion and cracking of metals (all) that are covered by thermal insulations
Galvanic corrosion	Corrosion due to dissimilar metal contacts
Cooling water corrosion	Corrosion of metals (e.g. heat exchangers) handling cooling water
Flue gas dew-point corrosion	Corrosion of carbon steel, stainless steel (fire stacks, boiler tubes) due to dew point condensation of Cl^- and SO_x
Atmospheric corrosion	General corrosion and pitting of metals (all) exposed to weathering
Soil corrosion	Corrosion of structures, metals in contact with soil
Graphitic corrosion	Removal of Fe from cast iron matrix in environments w.r.t temperature, degree of aeration, pH and exposure time
De-alloying (leaching)	Selective leaching of metals from Cu alloys (brass, bronze), Alloy 400 w.r.t environmental factors such as pH, aeration, temperature and exposure time
Microbiologically influenced corrosion	Corrosion of Ships, storage tanks, stagnant low points in vessels
Caustic corrosion	Localized corrosion of Carbon steel, low alloy steel, SS 3xx from alkaline salts
CO_2 corrosion	Corrosion Carbon steel in CO_2 handling systems due to formation of carbonic acid

**Table B4 Reported high temp. corrosion(s) for oil and gas applications [1]***

TYPE OF CORROSION	BRIEF DESCRIPTIONS
Oxidation	Oxide scale formation and thinning of carbon steel, low alloy steels, SS xx, SS 4xx, Ni based alloys under high temperatures
Sulfidation	Sulfide scale formation and thinning of carbon steel, low alloy steels, SS xx, SS 4xx, Ni and Cu based alloys in sulfur service at high temperatures i.e. > 260 ºC
Carburization	Increased hardness and reduced ductility of carbon steel, low alloy steel, SS 3xx, SS 4xx, Ni based (600, 800) and HK/HP alloys
De-carburization	Loss in hardness, strength of Carbon steels, low alloy steels due to removal of Carbon from matrix due to low carbon gaseous environment
Metal Dusting	Pitting on the surface of alloys (all) at high temperatures (482 ºC-816 ºC) in reducing gas (CH_4, CO, H_2 etc.) environments
Fuel ash corrosion	Corrosion (deposits) on alloys (all) in fired heater, gas turbines and boiler applications
Nitriding	Formation of nitride scale at high temperatures (>316 ºC) on Carbon steels, low alloy steels, SS 3xx and SS 4xx in N_2 environments that retards the corrosion resistance

Appendix C – Additional figures
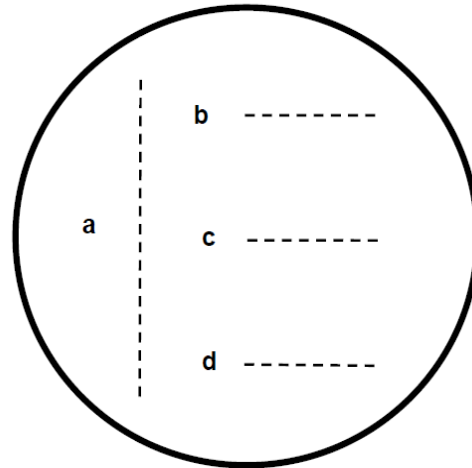
FIGURE C1 – SCARS MAP FOR SCRATCH TEST ON COATINGS AND SUBSTRATE
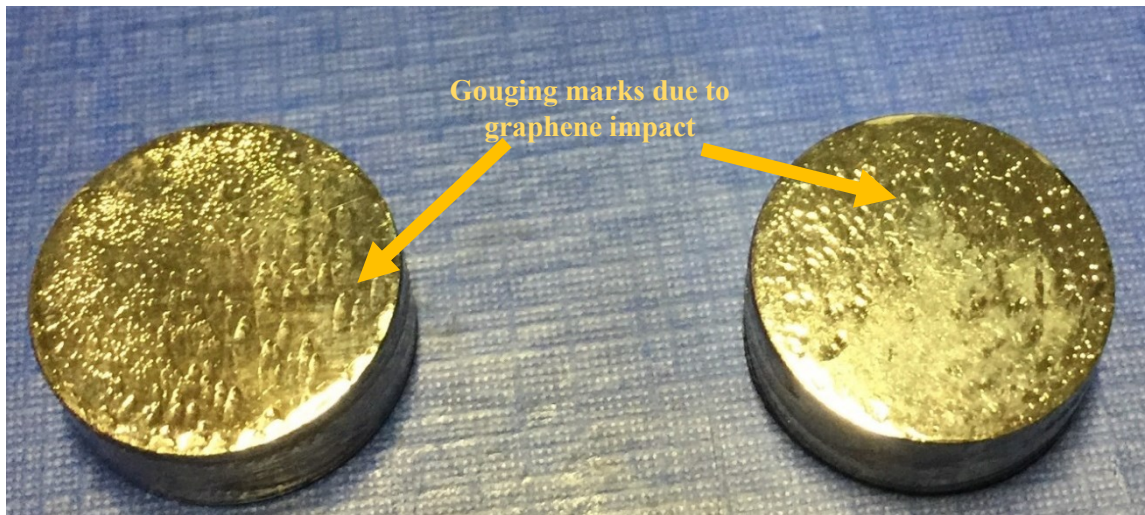
FIGURE C2 – GOUGING MARKS ON NI-P-10mg G COATING AFTER 1 HR OF PLATING UNDER 500 RPM
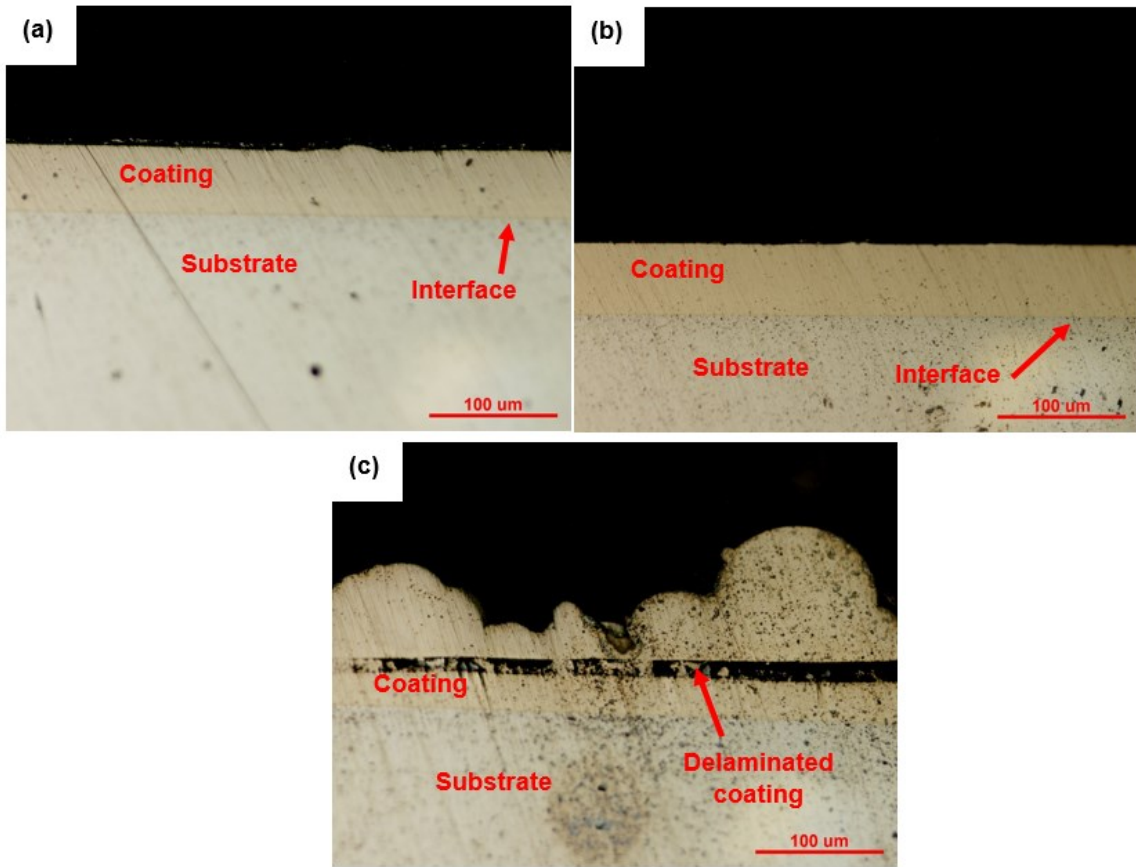
FIGURE C3 – MICROGRAPHS (MAG. 200x) FOR CROSS-SECTION OF (a) Ni-P-60mg G (b) Ni-P-100mg G (c) Ni-P-300mg G
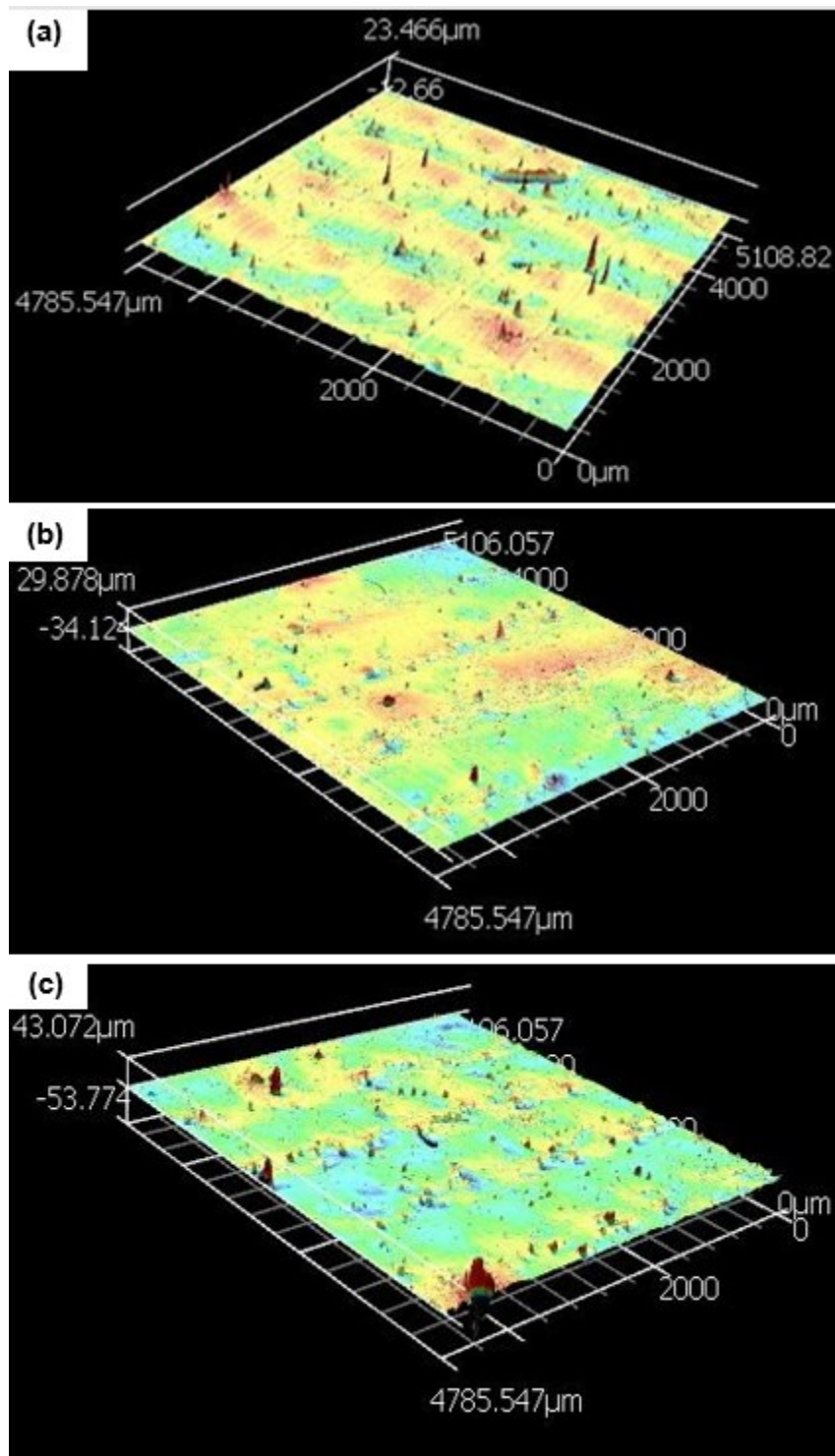
FIGURE C4 – SURFACE TOPOGRAPHS OVER 4 mm x 4 mm (ASPECT RATIO 1:1:700) FOR Ni-P-30mg G COATING AFTER PLATING TIME OF (a) 1 HR (b) 2 HRS (c) 3 HRS
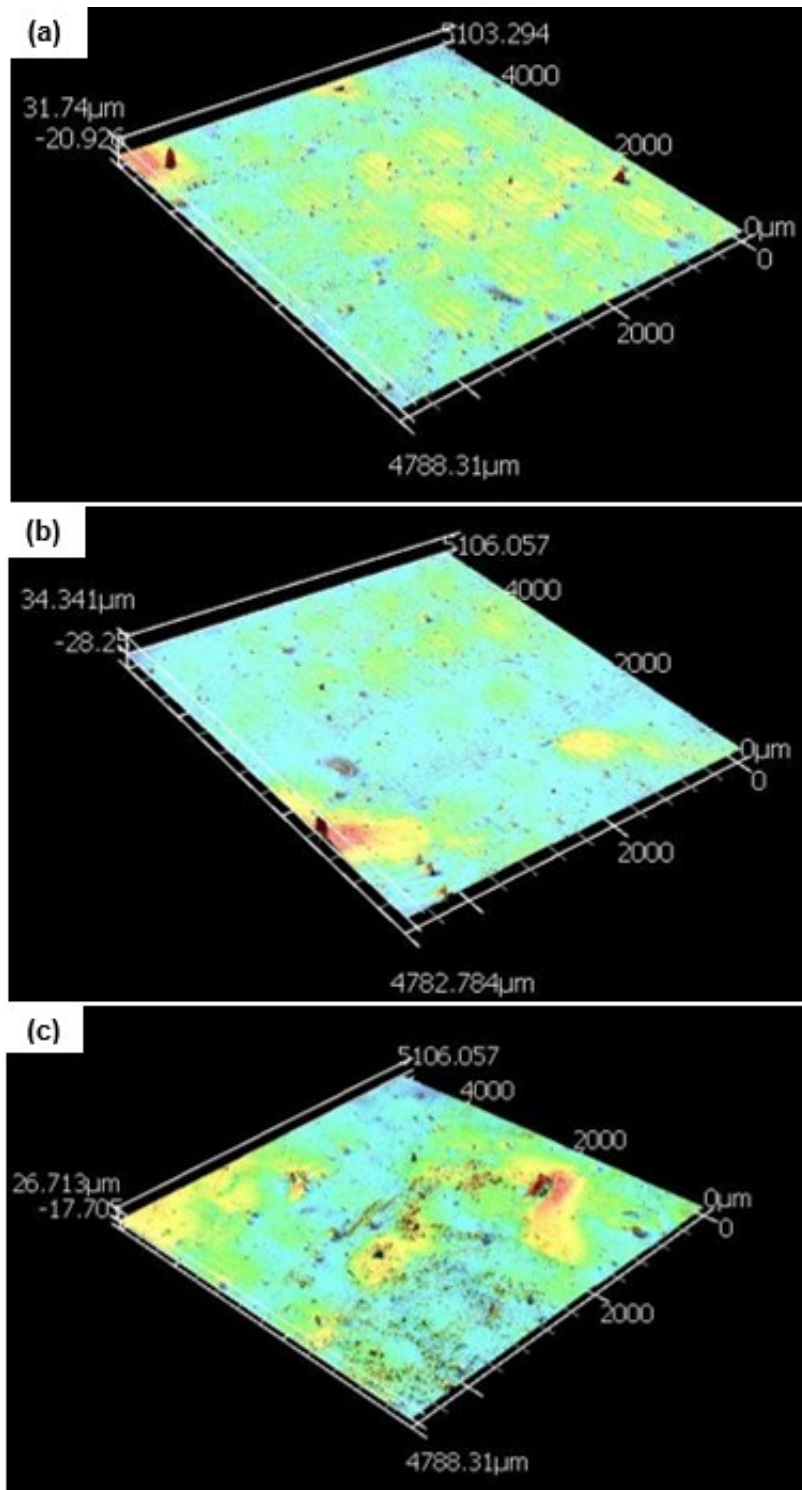
FIGURE C5 – SURFACE TOPOGRAPHS OVER 4 mm x 4 mm (ASPECT RATIO 1:1:700) FOR Ni-P-60mg G COATING AFTER PLATING TIME OF (a) 1 HR (b) 2 HRS (c) 3 HRS
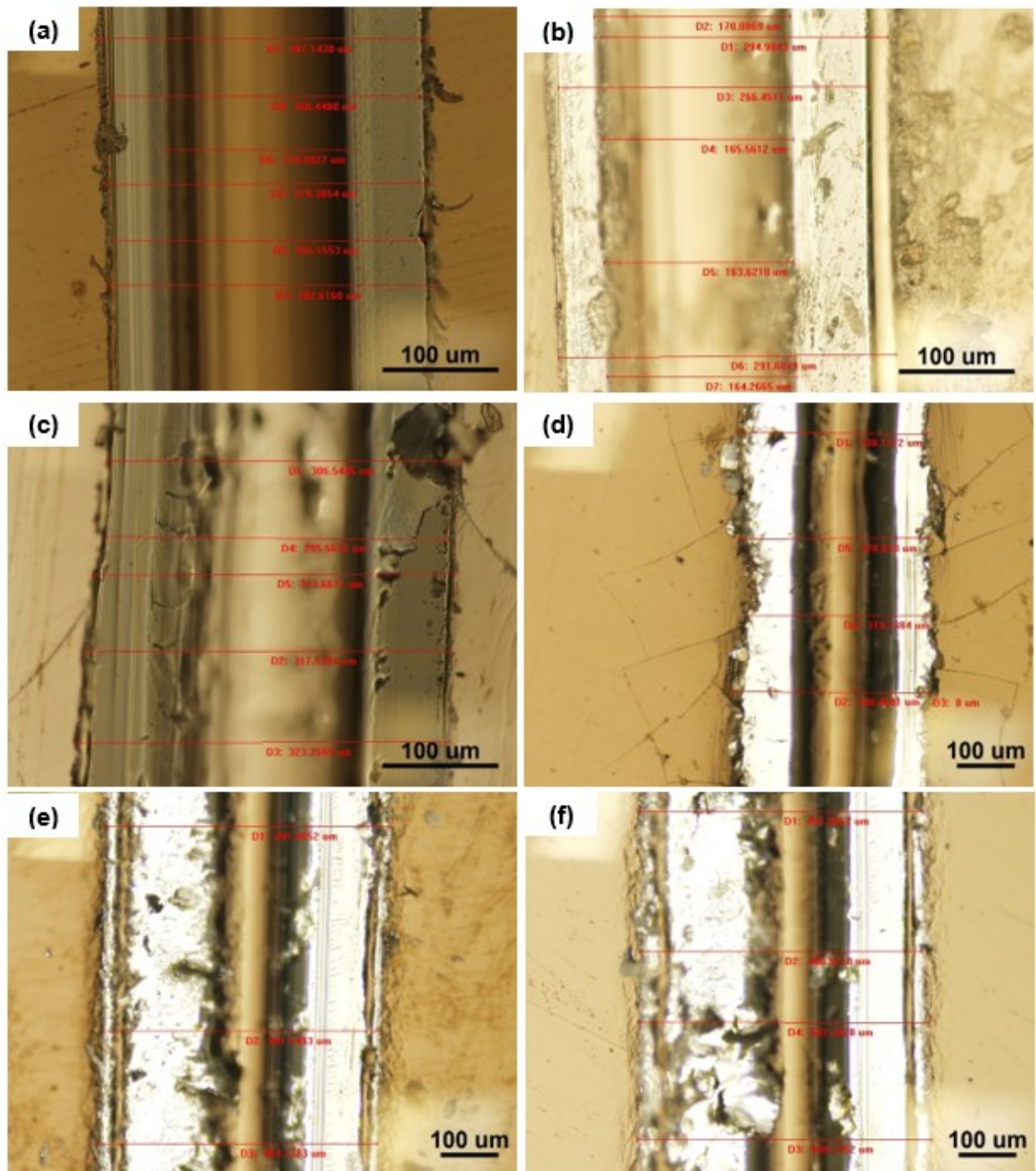
FIGURE C6 – MICROGRAPHS ON FOR SCARS (40 INDENTER PASSES) ON SURFACE OF COATINGS AND SUBSTRATE a) Ni-P b) Ni-P-30mg G c) Ni-P-60mg G d) Ni-P-100mg G e) Ni-P300mg G f) API X70 STEEL
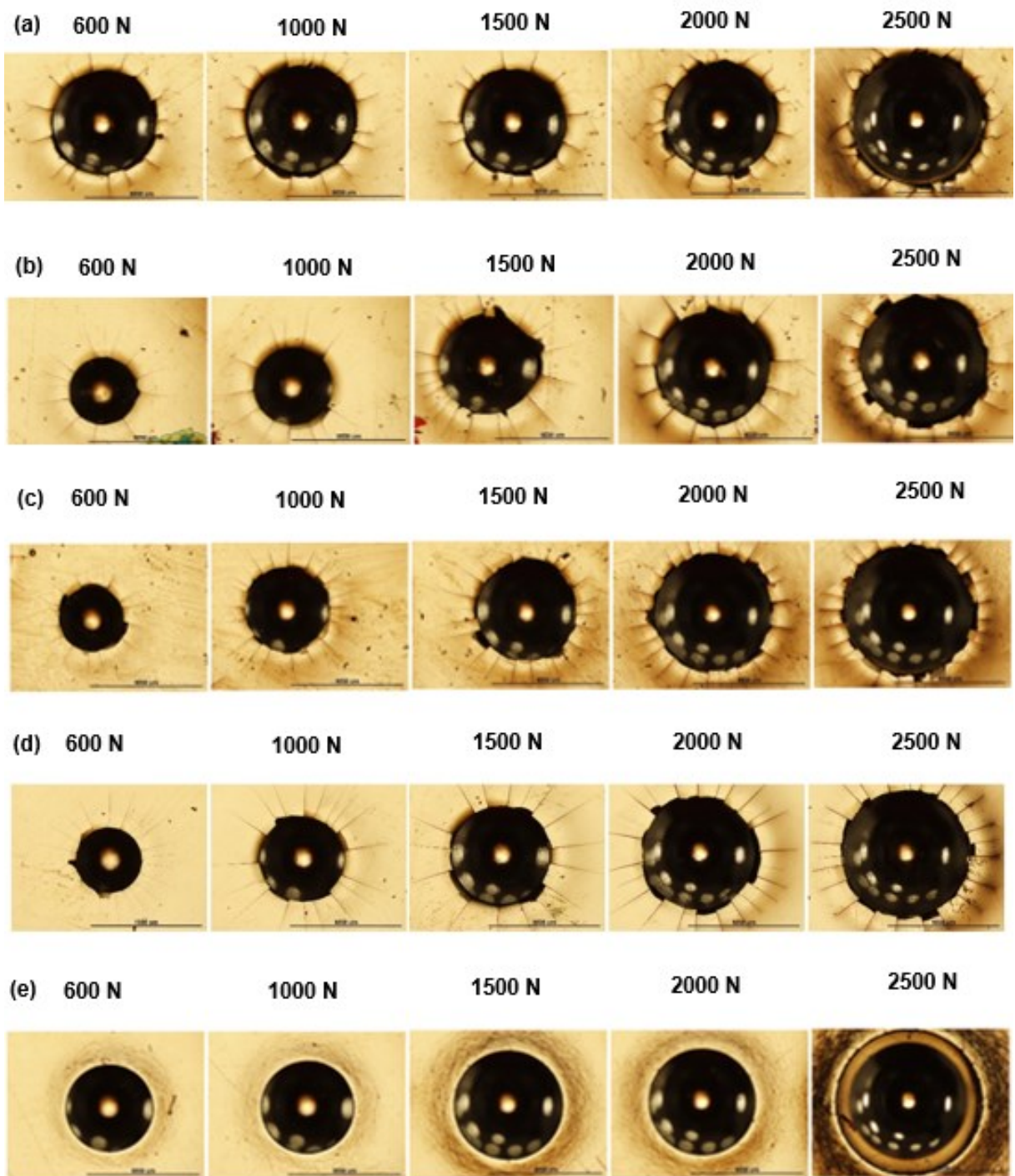
FIGURE C7 – MICROGRAPHS (MAG. 50x) FOR HERTZIAN INDENTS ON (a) Ni-P (b) Ni-P-30mg G (c) Ni-P-60mg G (d) Ni-P-100mg G (e) Ni-P-300mg G

(a) Hertzian Cracks

100 um

(b) 100 um

(c) Hertzian Crack
Multiple Bend cracks
(through thickness)
100 um
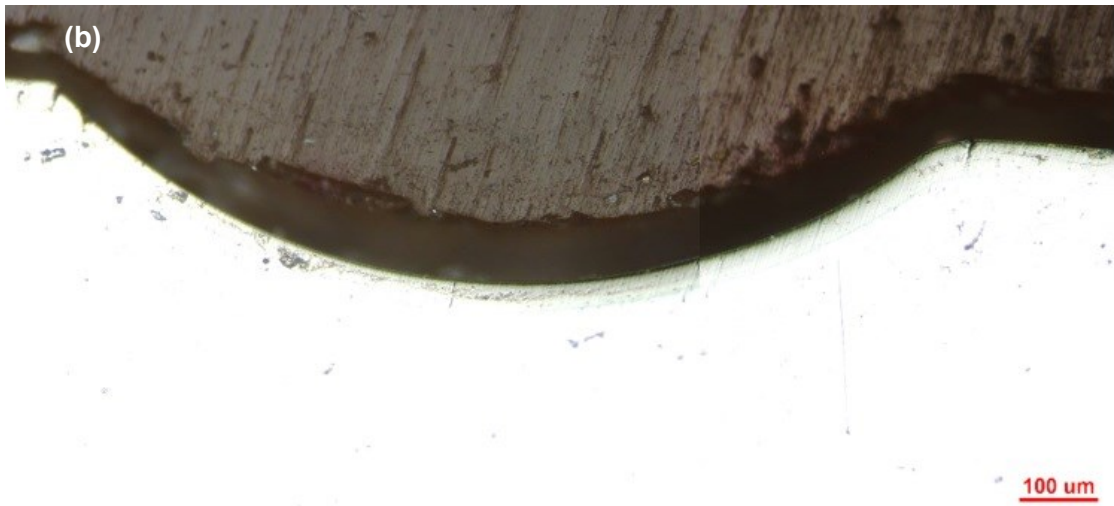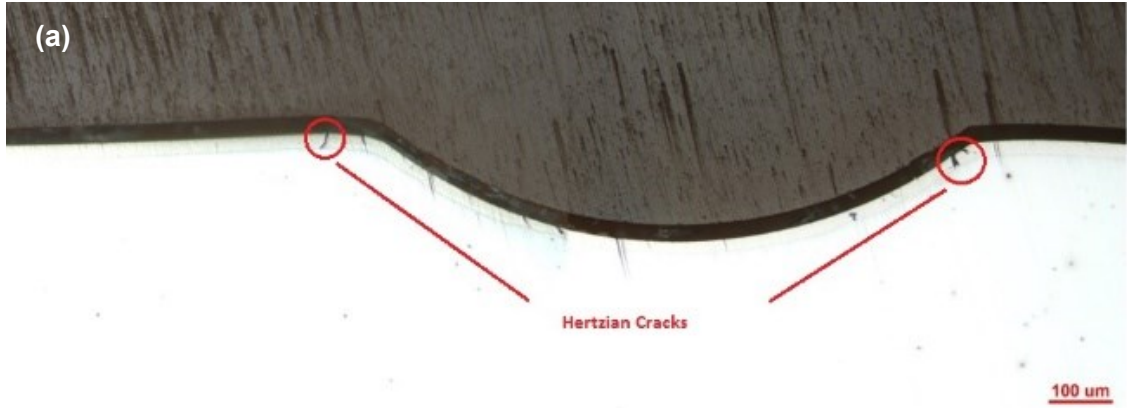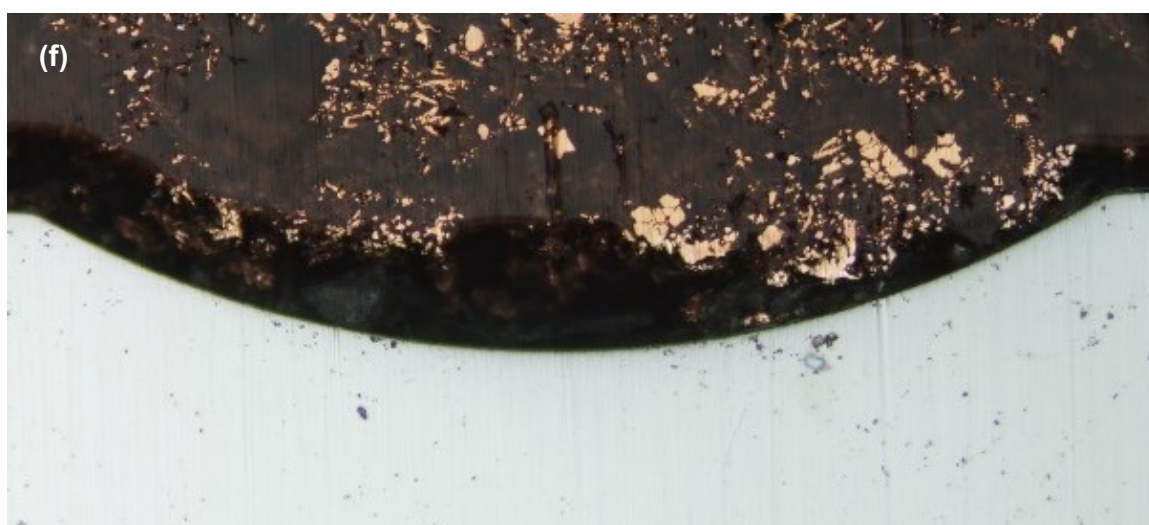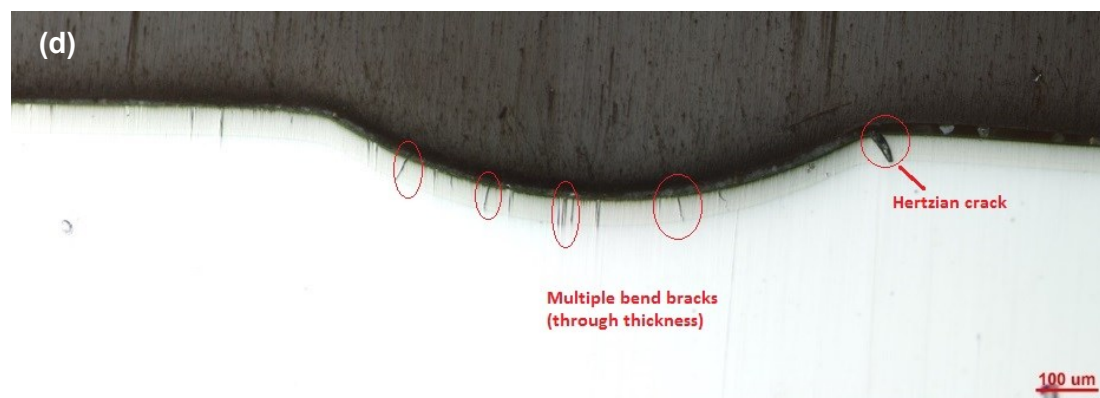
FIGURE C8– MICROGRAPHS (MAG. 100x) FOR CROSS-SECTION OF HERTZIAN INDENTS ON (a) Ni-P (b) Ni-P-30mg G (c) Ni-P-60mg G (d) Ni-P-100 mg G (e) Ni-P-300mg G (f) API X70 STEEL

(a)

Legend: Ni-P, Ni-P-30mg G, Ni-P-60mg G, Ni-P-100mg G, Ni-P-300mg G, API X70 Steel

(b)

Legend: Ni-P, Ni-P-30mg G, Ni-P-60mg G, Ni-P-100mg G, Ni-P-300mg G, API X70 Steel

114
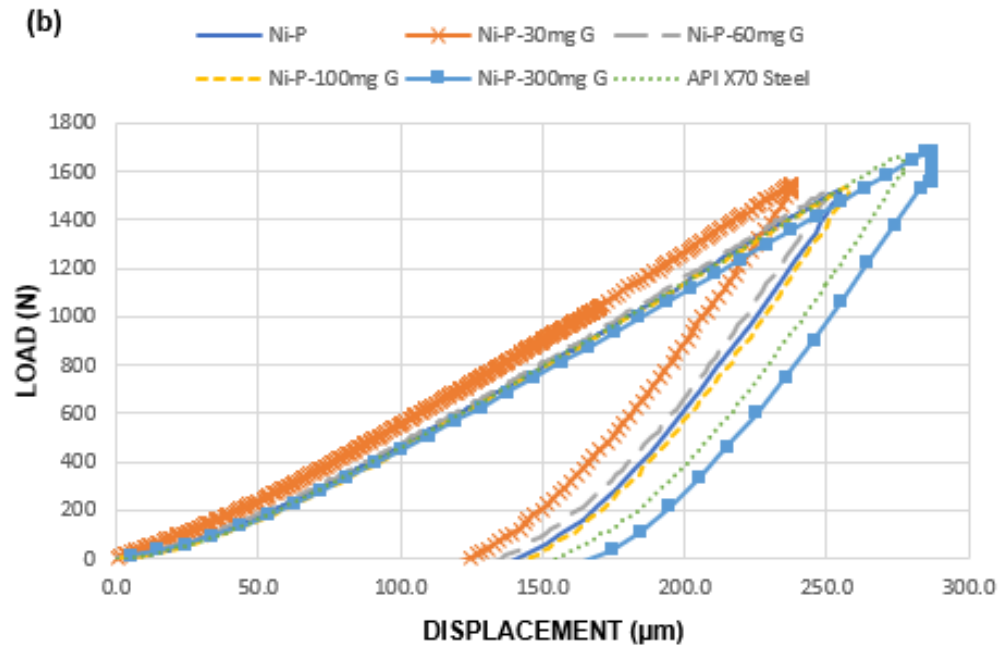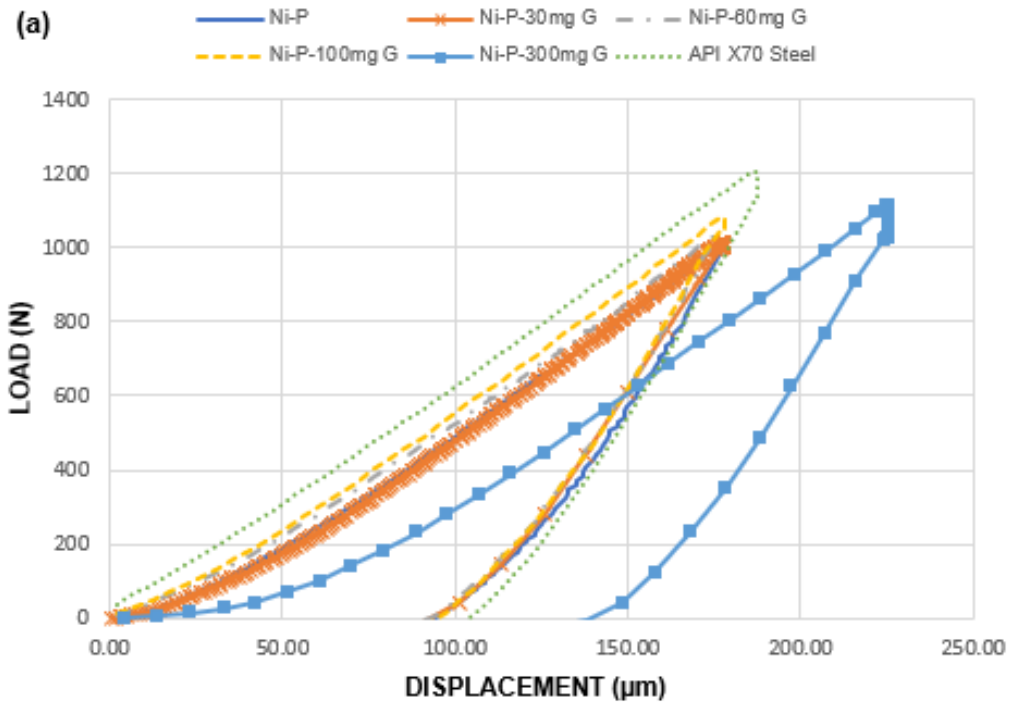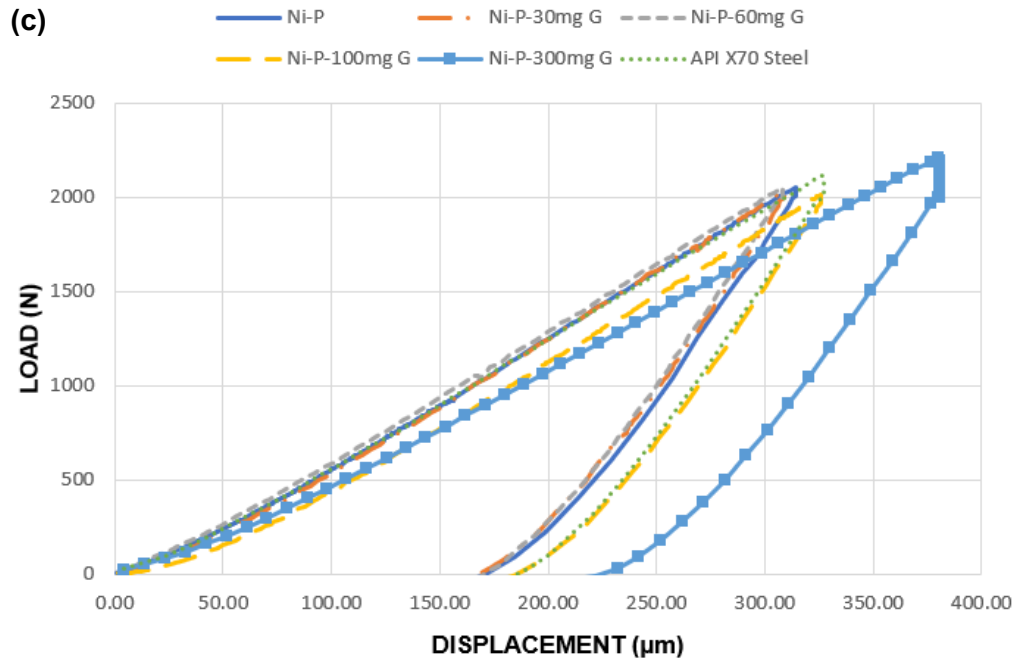
FIGURE C9 – LOAD-DISPLACEMENT CURVES FOR COATINSG AND SUBSTRATE UNDER LOAD OF (a) 1000 N (b) 1500 N (c) 2000 N

Appendix D – Copyright permissions

Scott Garten

Director of Intellectual Property Sales

Global Industry Services

200 Massachusetts Avenue, NW
Washington, DC 20001
USA
Telephone   202-682-8080
Fax   202-962-4717
Email   gartens@api.org
www.api.org

energy **API**

April 1th, 2020

Ahmad RK Rana
MASc Candidate
Department of Mechanical Engineering
Dalhousie University
Halifax NS B3H 4R2 Canada

Dear Ahmad RK Rana:

The American Petroleum Institute (Licensor) hereby grants a limited, non-exclusive license to Ahmad RK Rana (Licensee) to reproduce the API-copyrighted material outlined in Appendix A. The Licensee agrees that such license shall not grant it ownership rights of any derivative works created using the copyrighted works of API and such use shall be dependent on this license. The material may not be reproduced nor redistributed outside of this occurrence. Should you or anyone wish to reproduce this material in the future, in any other publication, for any other reason, permission must be requested again at that time.

A statement of acknowledgment, including the source API publication dates and the element titles, along with the statement, "Reproduced courtesy of the American Petroleum Institute", should appear for each element listed in the proposed attached handout.

API reserves the right to terminate this license at any time. By signing this license, you agree to withdraw this material from any published works within 90 days of receiving notice from API.

If the above terms are acceptable, please sign below and return to me.

Sincerely,

Scott Garten
Director, Global Industry Services

Agreed to by:
        Ahmad RK Rana
        MASc Candidate
        Department of Mechanical Engineering
        Dalhousie University

            4/1/2020 | 2:26 PM EDT
        _____
        Date

(Case 287)

Appendix A

- **API RP 571, 2nd Edition, April 2011,** *Damage Mechanisms Affecting Fixed Equipment in the Refining Industry*

  - Figure 1.10
  - Figure 1.23
  - Figure 4-84
  - Table B-1
  - Table B-2
  - Table B-3
  - Table B-4

- **API RP 581, 3rd Edition, April 2016,** *Risk-Based Inspection Technology*

  - Item 3.1.17

References

[1] American Petroleum Institute, RP 571 Damage Mechanisms Affecting Fixed Equipment in the Refining Industry, 2nd edition (2011)

[2] A. Rana, Z. Farhat., Mitigating Material Damages through Risk Based Inspections, Materials Performance Magazine, Vol 57 No.9 (2018) 46-49.

[3] William D. Callister, David G. Rethwisch, Materials science and Engineering an Introduction, 8th Edition (2010) 634, pp. 675

[4] NACE RP0192-HD1998-SG, Monitoring Corrosion in Oil and Gas Production with Iron Counts, NACE Inter., TX, 1998.

[5] ASM International, Corrosion: Fundamentals, Testing and Application, ASM Handbook, 13A (2003) 487

[6] Eman M. Fayyad, Aboubakr M. Abdullah, Mohammad K. Hassan, Adel M. Mohamed, George Jarjoura and Zoheir Farhat, Recent advances in electroless-plated Ni-P and its composites for erosion and corrosion applications: a review, Emergent Materials, (2018) 1:3-24.

[7] Edward P. Randviir, Dale A.C. Brownson and Craig E. Banks, A decade of graphene research: Production, applications and outlook, Materials Today, Volume 17, Number 9 (Nov. 2014) 426-432

[8] Graphene properties, American Elements [Internet] [Cited 2018 Dec. 30] https://www.americanelements.com/graphene-1034343-98-0

[9] Y. Su, V.G. Kravets, S.L. Wong, J. Waters, A.K. Geim & R.R. Nair, Impermeable Barrier films and protective coatings based on reduced graphene oxide, Nature Communications, 5:4843(Sep. 2014)

[10] Yanbin Cui, S.I. Kundalwal, S. Kumar, Gas barrier performance of graphene/ polymer nanocomposites, Carbon, 98 (2016) 313-333

[11] Khalid Youssef, Development of graphene based anti-corrosion coatings, The Petroleum Institute, (Nov. 2015.)

[12] Zhao zhong Qiu, Rui Wang, Jinzhu Wu, Yushen Zhang, Yunfei Qu and Xiaohong Wu, Graphene oxide as corrosion inhibitive coating on magnesium alloys, RSC Advances, 5 (2015)44149-44159

[13] Jibo Jiang, Haotian Chen, Liying Zhu, Wei Qian, Sheng Han, Hualin Lin, Huihui Wu., 2016, Effect of heat treatment on structures and mechanical properties of electroless Ni-P-GO composite coatings, RCS Advances, 6 (2016) 109001-109008

[14] Wei Shao, Jimin Wu, Hui Liu, Guanghui Dong, Shuxia Wang, Huihua Min and Min Huang., Graphene oxide reinforced Ni-P coatings for bacterial adhesion Inhibition, RCS Advances, 6 (2016), 46270-46277

[15] Cheng-Kuo Lee, Chi-Lun Teng, An-Hung Tan Electroless Ni-P/ Diamond/ Graphene Composite Coatings and characterization of their wear and Corrosion Resistance in Sodium Chloride Solution, Key Engineering materials, Vol. 656-657(Jan. 2015) 51–56

[16] T.R. Tamilarasan, U. Sanjith, M. Siva Sankar, G. Rajagopal., Effect of reduced graphene oxide (rGO) on corrosion and erosion-corrosion behavior of electroless Ni-P coatings, Wear 390-391 (2017) 385-391

[17] Qian Yu, Tiafeng Zhou, Yonggang Jiang, Xing Yan, Zhonglie An, Xibin Wang, Deyuan Zhang, Takahito Ono., Preparation of graphene-enhanced nickel-phosphorous composite films by ultrasonic assisted electroless plating, Applied Surface Science, 435 (2018) 617-625

[18] Maria Trzaska, Grzegorz Cieslak., 2015, Ni-P/ Graphene composite layers produced by chemical reduction method, Composite Theory and Practice, 15:3 (2015) 137-140

[19] Cui Lin, Nazila Dadvand, Zoheir Farhat and Georges Kipouros, Electroless Nickel Phosphorous Plating on Carbon steel, Materials Science and Technology, (2013) 2224-2237.

[20] Yuan Li and Nitin Chopra. "Progress in Large-Scale Production of Graphene. Part 1: Chemical Methods." Critical Reviews in Solid State and Materials Sciences, Vol 67 2015 No.1, pp. 34-43

[21] B Galindo, S Gil Alcolea, J Gómez, A Navas, A Ortega Murguialday, M Pérez Fernandez and R C Puelles, "Effect of the number of layers of graphene on the electrical properties of TPU polymers" 2nd International Conference on Structural Nano Composites Materials Science and Engineering 64 (2014)

[22] Paul Gabrielsen, "Thinnest graphene sheets react strongly with hydrogen atoms; thicker sheets are relatively unaffected" February 2013, Phys.org, p 1-2 https://phys.org/news/2013-02-thinnest-graphene-sheets-react-strongly.html

[23] P. R. Somani, S. P. Somani, and M. Umeno, Planer nanographenes from camphor by CVD, Chemical Physics Letters, 430, 56 (2006)

[24] A. N. Obraztsov, E. A. Obraztsova, A. V. Tyurnina, and A. A. Zolotukhin, Chemical vapor deposition of thin graphite films of nanometer thickness, Carbon, 45, 2017 (2007).

[25] Q. Yu, J. Lian, S. Siriponglert, H. Li, Y. P. Chen, and S. S. Pei, Graphene segregated on Ni surfaces and transferred to insulators, Appl. Phys. Lett., 93, 113103 (2008).

[26] Wonbong Choi, Indranil Lahiri, Raghunandan Seelaboyina, Yong Soo Kang. "Synthesis of Graphene and Its Applications: A Review." Critical Reviews in Solid State and Materials Sciences, 35:1, Feb. 2010, pp. 52–71

[27] G. D. Yuan, W. J. Zhang, Y. Yang, Y. B. Tang, Y. Q. Li, J. X. Wang, X. M. Meng, Z. B. He, et al., Graphene sheets via microwave chemical vapor deposition, Chem. Phys. Lett., 467, 361 (2009).

[28] Y. Hernandez, V. Nicolosi, M. Lotya, F. M. Blighe, Z. Sun, S. De, I. T. Mcgovern, et al., High-yield production of graphene by liquid-phase exfoliation of graphite, Nature Nanotechnol., 3, 563 (2008).

[29] M. Lotya, Y. Hernandez, P. J. King, R. J. Smith, V. Nicolosi, L. S. Karlsson, F. M. Blighe, et al., Liquid phase production of graphene by exfoliation of graphite in surfactant/water solutions, J. Am. Chem. Soc., 131, 3611 (2009).

[30] S. Horiuchi, T. Gotou, M. Fujiwara, T. Asaka, T. Yokosawa, and Y. Matsui, Single graphene sheet detected in a carbon nanofilm, Appl. Phys. Lett., 84, 2403 (2004)

[31] Sangiliyandi Gurunathan, Jae Woong Han, Eun Su Kim, Jung Hyun Park, Jin-Hoi Kim "Reduction of graphene oxide by resveratrol: a novel and simple biological method for the synthesis of an effective anticancer nanotherapeutic molecule". International Journal of Nanomedicine, 2015:10, pp. 2951–2969

[32] Bipinchandra K. Salunke and Beom Soo Kim, "Facile synthesis of graphene using a biological Method" RSC Adv., 2016, 6, pp. 17158-17162

[33] Z.Wu, W.Ren, L.Gao, B.Liu, C.Jiang,and H.Cheng, Synthesis of high-quality graphene with a pre-determined number of layers, Carbon, 47, 493 (2009)

[34] Z.Y. Juang, C.-Y. Wu, C.-W. Lo, W.-Y. Chen, C.-F. Huang, J.C. Hwang, F.-R. Chen, et al., Syntehsis of graphene on silicon carbide substrates at low temperature, Carbon, 47, 2026 (2009).

[35] C.D. Kim, B.K. Min, and W.S. Jung, Preparation of graphene sheets by the reduction of carbon monoxide, Carbon, 47, 1610 (2009).

[36] Stephen F. Bartolucci, Joseph Parasa, Mohammad A. Rafieeb, Javad Rafiee, Sabrina Lee, Deepak Kapoor, Nikhil Koratkar. "Graphene-aluminum nano-composites." Materials Science and Engineering A, 528 (2011), Jul-2011, pp. 7933-7937

[37] Wenchao Tian, Wenhua Li, Wenbo Yu and Xiaohan Liu, "A Review on Lattice Defects in Graphene: Types, Generation, Effects and Regulation" Micromachine 2017 8, 163 pp. 1-15

[38] Letardi, Sara; Celino, Massimo; Cleri, Fabrizio; Rosato, Vittorio (2002). "Atomic hydrogen adsorption on a Stone–Wales defect in graphite". Surface Science. 496 (1–2), pp. 33–38

[39] https://en.wikipedia.org/wiki/Stone%E2%80%93Wales_defect

[40]https://www.mt.com/ca/en/home/applications/L1_AutoChem_Applications/Raman-Spectroscopy.html

[41] Mark Wall, Ph.D. "The Raman Spectroscopy of Graphene and the Determination of Layer Thickness." Thermo Fisher Scientific, Madison, WI, USA

[42] https://en.wikipedia.org/wiki/Graphene#cite_note-90

[43] Limin Ma, Zhengang Lu, Jiubin Tan, Jian Liu, Xuemei Ding, Nicola Black, Tianyi Li, John Gallop, Ling Hao, "Transparent Conducting Graphene Hybrid Films To Improve Electromagnetic Interference (EMI) Shielding Performance of Graphene" ACS Appl. Mater. Interfaces 2017 9, 39, pp. 34221-34229

[44] Trisetyarso, Agung "Dirac four-potential tunings-based quantum transistor utilizing the Lorentz force". Quantum Information & Computation Volume 12 Issue 11-12 Nov 2012, pp. 989-1010

[45] Recep Zan, Quentin M. Ramasse, Ursel Bangert and Konstantin S. Novoselov "Graphene re-knits its holes" https://arxiv.org/ftp/arxiv/papers/1207/1207.1487.pdf

[46] https://phys.org/news/2018-08-high-graphene-based-catalysts.html

[47] Sunil P Lonkar and Ahmed A. Abdala, "Applications of Graphene in Catalysis" Journal of J Thermodynamics & Catalysis, Volume 5 Issue 2, p. 1-6

[48] Yi Feng Fu, Josef Hansson, Ya Liu, Shujing Chen, Abdelhafid Zehri, Majid Kabiri Samani, Nan Wang, Yuxiang Ni, Yan Zhang, Zhi-Bin Zhang, Qianlong Wang, Mengxiong Li, Hongbin Lu, Marianna Sledzinska, Clivia M Sotomayor Torres, Sebastian Volz, Alexander A Balandin, Xiangfan Xu and Johan Liu "Graphene related materials for thermal management" 2D Mater. 7 (2020) 012001, pp. 1-42

[49] Fernanda MP Tonelli, Vânia AM Goulart, Katia N, Gomes, Marina S Ladeira, Anderson K Santos, Eudes, Lorençon, Luiz O Ladeira & Rodrigo R Resende "Graphene-based nanomaterials: biological and medical applications and toxicity, Nanomedicine (2015)

[50] Subhashree Priyadarsini, Swaraj Mohanty, Sumit Mukherjee, Srirupa Basu, Monalisa Mishra, "Graphene and graphene oxide as nanomaterials for medicine and biology application" Journal of Nanostructure in chemistry 2018(8), pp 123-137

[51] Chuhong Wang, "Indentation and Fracture Behaviour of Electroless Ni-P-based Composite Coatings" Dissertation (2017)

[52] A. Almotairi, A. Warkentin, Z. Farhat. "Mechanical damage of hard chromium coatings on 416 stainless steel." Engineering Failure Analysis, Vol. 66 (2016) pp. 130-140

[53] G.M.P. Robert F. Cook. "Direct Observation and Analysis of Indentation Cracking in Glasses and Ceramics." Journal of American ceramic society, 73(4) 1990, pp. 787-817

[54] http://www.amteccorrosion.co.uk/buildings.html

[55] Gwidon W. Stachowiak, Andrew W. Batchelor "Engineering Tribology handbook 3rd edition (2005)

[56] P.J.S. Buenconsejo, K. Ito, H.Y. Kim, S. Miyazaki. "High-strength super elastic Ti–Ni microtubes fabricated by sputter deposition" Acta Materialia, Vol. 56 (2008) pp. 2063-2072

[57] Recommended practice for design and installation of offshore production platform piping systems RP 14E, 5th Edition, American Petroleum Institute, 1991.pp. 23

[58] I. Serre, N. Celati, R.M. Pradeilles -Duval "Tribological and corrosion wear of graphite ring against Ti6Al4V disk in artificial sea water" Wear 252 (2002), pp. 711-718

[59] A. Rana, Z. Farhat., Neighborhood – An Influential Factor for Material Damages, Materials Performance Magazine, Vol 58 No.6 (2019) pp. 52-55

[60] ASTM Inter. (2013) Lab Simulation of Corrosion Under Insulation G189-07. ASTM, W. Conshohocken PA

[61] https://www.palmsenscorrosion.com/knowledgebase/tafel-plot-and-evans-diagram/

[62] ASTM Inter. (2010) Standard Practice for Calculation of Corrosion Rates and Related Information from Electrochemical Measurements G102-89. ASTM, W. Conshohocken PA

[63] ASTM Inter. (2012) Standard Guide for Determining Synergism Between Wear and Corrosion G119-09. ASTM, W. Conshohocken PA

[64] Digital Transformation Initiative Oil and gas Industry, World Economic Forum Geneva (2015)

[65] American Petroleum Institute, RP 581 Risk-Based Inspection Methodology, 3rd edition (2016)

[66] G.M. Nagaraja Rao and C.R.L. Murthy. "Dual role of microcracks: toughening and degradation", Can. Geotech. J. 38 (2001), pp. 427–440

[67] J. Pelleg, Mechanical properties of materials, books, (2013).

[68] Robert o Ritchie, John H Kinney, Jamie K Kruzic, R.K. Nalla "Invited Article A fracture mechanics and mechanistic approach to the failure of cortical bone" Fatigue Fract Engng Mater Struct 28 (2005), pp. 345–371

[69] J.J. Kruzic, R.K. Nalla, J.H. Kinney, R.O. Ritchie, Crack blunting, crack bridging and resistance-curve fracture mechanics in denting: effect of hydration, Biomaterials, 24 (2003) pp. 5209-5221

[70] A. Sakaida, C.D. Bencher, K. T. Venkateswara Rao, R. O. Ritchie, Toughening mechanisms in ductile niobium-reinforced niobium aluminide (Nb/Nb3Al) in situ composites, Metallurgical and Materials Transactions A, 26A (1995) pp. 2027-2033

[71] R.O. Ritchie, Mechanisms of fatigue crack propagation in metals, ceramics and composites: Role of crack tip shielding, Materials Science and Engineering: A, 103 (1988) pp.15-28

[72] H.Ruf, A.G. Evans, Toughening by monoclinic zirconia, Journal of the American Ceramic Society, 66 (1983) pp. 328-332

[73] ISO Geometrical product specifications – Surface Texture 25178. ISO (2010), Geneva

[74] ASTM Inter. (2015) Standard Test Method for Vickers Indentation Hardness of Advanced Ceramics C1327-15. ASTM, W. Conshohocken PA

[75] ASTM Inter. (2015) Standard Practice for Instrumented Indentation Testing E2546-15. ASTM, W. Conshohocken PA

[76] ASTM Inter. (2015) Standard Test Method for Adhesion Strength and Mechanical Failure Modes of Ceramic Coatings by Quantitative Single Point Scratch Testing C1624-05. ASTM, W. Conshohocken PA

[77] ASM International, Friction, Lubrication and Wear Technology, ASM Metals Handbook, 18 (1992) pp. 696

[78] H. M. Hawthorne, Y. Xie, and S. K. Yick (2000) Different responses of thermal sprayed WC-Co-Cr coatings to erosion by Alumina Slurry in coriolis and jet experiments. Proceedings of the International Tribology Conference pp. 1031–1036.

[79] H. M. Clark (1995) A comparison of particle impact in gas-solid and liquid-solid erosion. Wear 186–187 PART 2, pp. 465–472.

[80] Md. Aminul Islam, Jiaren (Jimmy) Jiang, Yonsong Xie, Petr Fiala (2017) Investigation of erosion-corrosion behaviour of (WTi)C based weld overlays. Wear 390-391, pp. 155-165.

[81] ASTM Inter. (2009) Standard Test Method for Conducting Potentiodynamic Polarization Resistance Measurements G59-97. ASTM, W. Conshohocken PA

[82] US nano research (2019) Research Grade Single Layer Graphene Nanoparticles 1 wt. % Water Dispersion https://www.us-nano.com/inc/sdetail/11386. Accessed 10 May 2019

[83] Raman spectrum of graphene US Nano Materials Research (internet) [Cited 2018 Dec. 30] https://n.b5z.net/i/u/10091461/i/US7905-5-Raman_Graphene.jpg

[84] F. Tuinstra, J.L. Koeing. Raman Spectrum of Graphite, Journal of Chemical Physics Vol. 53 Number. 3(Aug. 1970) 1126-1130

[85] Nikhil A. Koratkar., Graphene in Composite Materials Synthesis, Characterization and Applications,17-24

[86] A. C. Ferrari, J. C. Meyer, V. Scardaci, Casiraghi, M. Lazzeri, F. Mauri, S. Piscanec, D. Jiang, K. S. Novoselov, S. Roth, A. K. Geim., Raman Spectrum of Graphene& Graphene Layers

[87] Chuhong Wang, Zoheir Farhat, George Jarjoura, Mohamed K. Hassan, Aboubakr M. Abdullah (2017) Indentation and erosion behaviour of electroless Ni-P coating on pipeline steel. Wear 376-377, pp. 1630-1639.

[88] Wei Gao and Rui Huang (2011) Effect of surface roughness on adhesion of graphene membranes. J. Phys. D: Appl. Phys. 44, pp. 1-4.

[89] Pramoda K. Nayak, Chan-Jung Hsu, Sheng-Chang Wang, James C. Sung, Jow-Lay Huang (2013) Graphene coated Ni films: A protective coating. Thin Solid Films 529, pp. 312-316

[90] N.T. Kirkland, T. Schiller, N. Medhaker, N. Birbilis (2012) Exploring graphene as a corrosion protection barrier. Corrosion Science 56, pp.1-4

[91] Md. Aminul Islam, Jiaren (Jimmy) Jiang, Yonsong Xie, Petr Fiala (2017) Investigation of erosion-corrosion behaviour of (WTi)C based weld overlays. Wear 390-391, pp.155-165.

[92] C.T. Kwok, F.T. Cheng, H.C. Man (2001) Laser-fabricated Fe-Ni-Co-Cr-B austenitic alloy on steels. Part II. Corrosion behavior and corrosion-erosion synergism. Surface & Coatings Technology 145, pp. 206-214.

[93] H.S. Kirols, D. Kevorkov, A. Uihlein, M. Medraj (2015) The effect of initial surface roughness on water droplet erosion behaviour. Wear 342-343, pp. 198-209.

[94] Md. Aminul Islam, Zoheir Farhat, Elsadig M. Ahmed, A.M Alfantazi (2013) Erosion enhanced corrosion and c orrosion enhanced erosion of API X-70 pipeline steel Wear 302, pp. 1592-1601

[95] J. Xie, A. Alpas, D. Northwood (2003) The effect of erosion on the electrochemical properties of AISI 1020 steel. Journal of Material Engineering and Performance 12, pp. 77–86

[96] Md. Aminul Islam, Zoheir Farhat (2014) Effect of impact angle and velocity on erosion of API X42 pipeline steel under high abrasive feed rate. Wear 311, pp. 180-190

[97] Gwidon W. Stachowiak, Andrew W. Batchelor (2005) Engineering Tribology 3rd edn. Elsevier, Burlington, pp. 501-507

[98] R. B. REBAK, "Stress corrosion cracking (SCC) of nickel-based alloys" Wood head publishing ltd. (2011), pp. 273-306